2009

Modeling and Feedback Control of a MEMS Electrostatic Actuator

Jason Edwards
Cleveland State University

MODELING AND FEEDBACK CONTROL OF A MEMS ELECTROSTATIC ACTUATOR

JASON M. EDWARDS

Bachelor of Electrical Engineering

Cleveland State University

May, 2004

submitted in partial fulfillment of requirements for the degree

MASTER OF SCIENCE IN ELECTRICAL ENGINEERING

at the

CLEVELAND STATE UNIVERSITY

December, 2008

This thesis has been approved
for the Department of Electrical and Computer Engineering
and the College of Graduate Studies by

_____

Thesis Committee Chairperson, Lili Dong

_____

Department/Date

_____

Dr. Zhiqiang Gao

_____

Department/Date

_____

Dr. Dan Simon

_____

Department/Date

ACKNOWLEDGEMENTS

First of all, I would like to thank my employer for being patient and supporting the furthering of my education. Without their support (temporal and financial) this thesis wouldn't be possible. Secondly, I would like to thank my advisor, Dr. Dong, for not only helping me choose my thesis topic, but also for the tedious hours proof reading it. I would also like to thank my thesis committee, Dr. Dong, Dr. Gao and Dr. Simon for helping instill my knowledge of controls, and in the end, letting me know that I have only begun my journey to understanding. Finally, I would like to thank my family for putting up with me while I finish this stage of my academic career.

MODELING AND FEEDBACK CONTROL OF A MEMS ELECTROSTATIC ACTUATOR

JASON M. EDWARDS

ABSTRACT

This thesis describes the mathematical modeling and closed-loop voltage control of a MEMS electrostatic actuator. The control goal is to extend the travel range of the actuator beyond the open-loop pull-in limit of one third of the initial gap. Three controller designs are presented to reach the control goal. The first controller design utilizes a regular fourth order Active Disturbance Rejection Controller (ADRC) and is able to achieve 97% of the maximum travel range. The second design also uses a fourth order ADRC, while additional modeling information is included in an Extended State Observer (ESO), which is part of the ADRC, to improve control performance. This controller achieved 99% of the travel range. The third design is a multi-loop controller with a second order ADRC in an inner loop and a Proportional-Integral (PI) controller in an outer loop. This design achieved 100% of the travel range. Transfer function representations of the three controller designs are developed. The controllers are successfully applied and simulated in a parallel-plate electrostatic actuator model. The simulation results and frequency domain analyses verified the effectiveness of the controllers in extending the travel range of the actuator and in noise attenuation.

TABLE OF CONTENTS

Page

LIST OF TABLES

Table **Page**

LIST OF FIGURES

Figure **Page**

NOMENCLATURE

1-DOF:	One Degree of Freedom
2-DOF:	Two Degrees of Freedom
3-DOF:	Three Degrees of Freedom
ADRC:	Active disturbance rejection control
C:	Controller
ESA:	Electro-Static Actuator
ESO:	Extended State Observer
F:	Prefilter
g_0:	Actuator gap with zero applied voltage
G:	Actuator gap
ISE:	Integral Squared Error
L:	Loop transmission
LADRC:	Linear ADRC
MEMS:	Micro-Electro-Mechanical Systems
P:	Plant
PD:	Proportional-Derivative
PI:	Proportional-Integral

PID:	Proportional-Integral-Derivative
q:	Normalized charge
Q:	Charge
Q_{eq}:	Equilibrium charge
QFT:	Quantitative Feedback Theory
S:	Sensitivity function
T:	Complementary sensitivity function
v_s:	Normalized source voltage
V_{eq}:	Equilibrium source voltage
V_s:	Source voltage
x:	Normalized displacement
X:	Displacement
X_{eq}:	Equilibrium displacement

CHAPTER I

INTRODUCTION

This introductory chapter will define a Micro-Electro-Mechanical System (MEMS) electrostatic actuator. The applications of the actuator in micro-systems will be introduced. The control problems associated with this device will be discussed. With this information in hand, it will be shown how researchers have attempted to solve these problems in the past. A few different existing control strategies will be briefly presented. At the end of the chapter, the outline for the rest of the thesis will be given.

1.1 Electrostatic Actuators

MEMS electrostatic actuators, also termed as micro-actuators, are the key devices allowing MEMS to perform physical movements [1]. They have the advantages of small size, low cost, and low power consumptions. An impressive range of applications demonstrates the electrostatic actuators' utility. Some examples of the applications are: micro-mirrors, optical gratings, variable capacitors, and micro-accelerometers [2]. Figure 1 shows a simplified illustration of a parallel-plate electrostatic actuator used in a micro-mirror device [3].

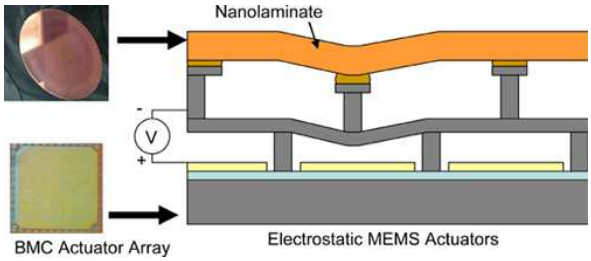

Figure 1: Illustration of an Electrostatic Actuator Used in Micro-mirror Device [3]

From this diagram one can develop a simplified model of the electrostatic actuator that captures the important system dynamics, as shown in Figure 2.

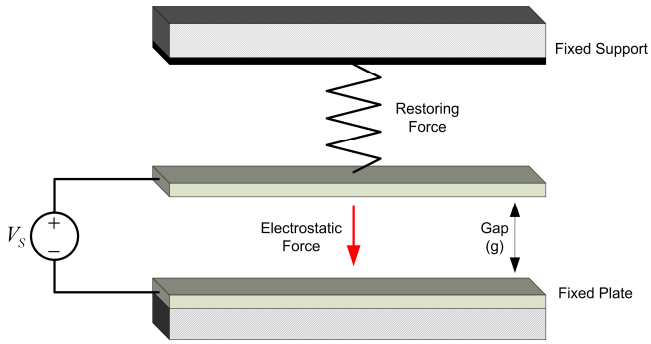

Figure 2: A Simplified Model of the Electrostatic Actuator

In Figure 2, a parallel-plate micro-actuator consists of a movable plate and a fixed plate in an electric field. When the movable plate is displaced from its original position, the capacitance formed between the two plates is changed. Therefore, one can change the displacement of the movable plate through a voltage control of the gap of the capacitor. However, as the gap between the two plates is decreasing to two thirds of the original gap, a pull-in (or snap-down) phenomenon will cause the instability of the system and drag the movable plate to the fixed plated, immediately reducing the gap to zero [4]. Thus the pull-in phenomenon can cause a failure of operation of the electrostatic actuator. Chapter 2 explains the physics behind the electrostatic actuation in more detail. Extending the traveling range of the movable plate beyond the pull-in limit has been attractive to more and more researchers and it is also the control goal of this thesis.

1.2 Applications of MEMS Electrostatic Actuators

MEMS electrostatic actuators are key components in many micro-systems. They have been used in micro-grippers, micro-relays, gyro sensors, micro-motors, cantilevers, optical shutters, variable optical attenuators and micro-mirrors. Electrostatic actuators and other MEMS devices in general, make the biggest impact when they are designed to tackle real-world problems in a novel way. One example of this innovative spirit is the use of micro-mirrors in Digital-Light-Processing (DLP) televisions. Figure 3 shows an array of pixels of a Deformable Mirror Device (DMD) [5, 6].

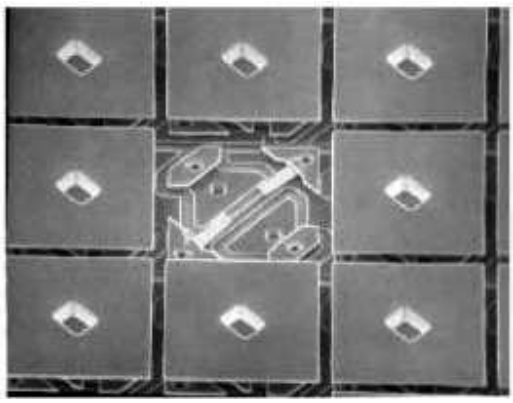

Figure 3: DMD Pixel Array [5, 6]

Figure 4 shows a close-up view of a single DMD pixel.

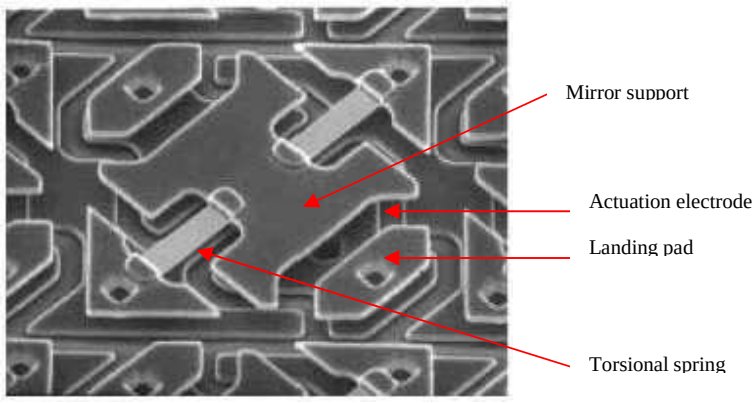

Figure 4: A single DMD Pixel [5, 6]

These mirrors reflect incident light into the image direction when the mirrors are in one position, or deflect the light out of the image direction when the mirror is tipped in a different direction. The tipping motion of the DMD device is based on the change of capacitance between two parallel plates, constituting an electrostatic actuator [6]. The electrostatically actuated micromirrors, as shown in Figure 5, can also be used in all optical switches [7].

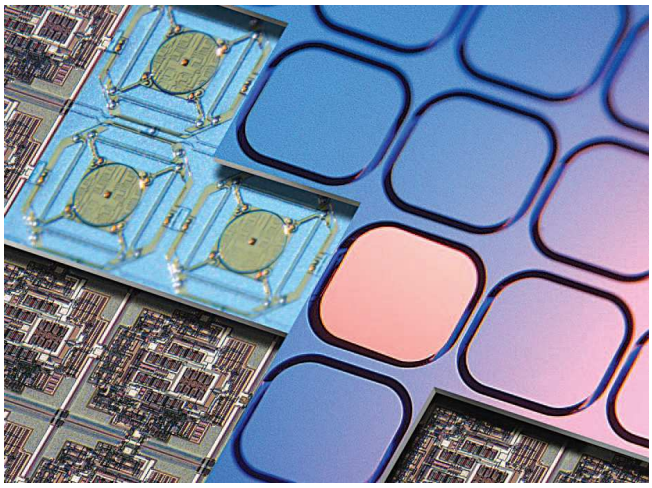

Figure 5: Electro-statically Actuated Micro-Mirror Array [7]

The electrostatic-actuator-based micro-mirror is a leading candidate to replace the optical-electrical-optical switching technology used today. MEMS technology allows high-precision micromechanical components such as micro-mirrors to be mass produced at low cost. These components can be precisely controlled to provide reliable high speed switching of optical beams in free space.

1.3 Control of Electrostatic Actuators

The majority of MEMS control techniques are resigned to academic labs and research institutions. As these designs become mature and are introduced into commercial applications the MEMS community will benefit from increased performance, reliability, accuracy and robustness against manufacturing variations. It was noted in [8] that "Most MEMS technologists do not have a background in control technology…." As a result the majority of MEMS devices were driven in an open-loop fashion. Improvements in dynamical behavior were the results of structural design improvements of the devices themselves. "MEMS actuators have therefore traditionally been gradually modified and improved in terms of mechanical design and better area-efficiency" [9]. As noted in [8], "as the sophistication level of MEMS devices increased, the electromechanical systems on a chip started to demand equally sophisticated integrated controls, including on-chip actuators."

However, closed-loop control of MEMS devices is not completely in its infancy. "The first MEMS devices incorporating feedback were closed-loop capacitive sensors,

with the objective of enhancing measurement accuracy" [8]. The slow adaptation of feedback control to MEMS design is not only due to a lack of control experiences in MEMS, but also due to the complexity of the implementation of the closed-loop controller. Unlike macro mechanical systems where the implementation of the feedback is relatively simple, it is quite problematic in the MEMS case. The incorporation of sensors and analog control circuitry into a MEMS device takes up valuable die real estate. In addition, it is difficult to operate these sensors and control circuitry at the same power level as the MEMS devices themselves. The inclusion of these circuits changes the dynamic behavior of the entire MEMS device. In the following sections we will look at some of the current control strategies used in design of MEMS electrostatic actuators.

1.3.1 Open-loop Control of Electrostatic Actuator

In the mechanical domain, there have been numerous suggested open-loop solutions to the pull-in phenomena. The most straightforward approach is to design the gap so large that the actuator is stable over the desired operating range. As an example if we needed an actuation range of 2 μm we would design the actuator gap to be 6 μm. The drawback of this approach is that the maximum gap is generally determined by the fabrication technology and cannot be easily changed by the designer [2].

Another approach is called leverage bending [10]. The idea behind the leverage bending method is to compensate for the pull-in instability by applying electrostatic force to only a portion of the structure, then using the rest of the structure as a lever to position specific parts of the structure through a large range of motion. The key is that the electro-

statically actuated portions of the structure deflect less than the pull-in limit, while the other portions of the structure can move through the entire gap. A drawback of this approach is that increased actuation voltages were required. Figure 6 shows the concept of leverage bending applied to a cantilever beam as reported in [10].

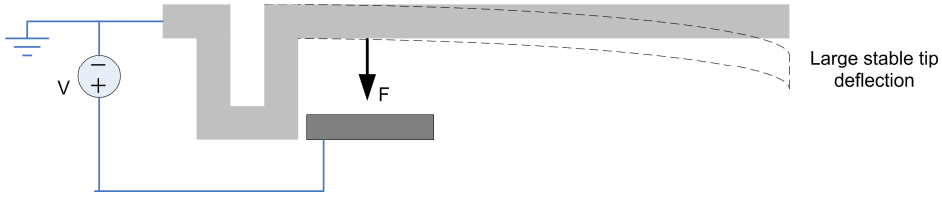

Figure 6: Leverage Bending [10]

Along with leverage bending, a technique called strain stiffening [10] was suggested as a way to supplement the elastic restoring force of the supports in a fixed-fixed beam (both ends anchored). The premise behind this technique is that as the beam deflects the tensile strength in the beam increases due to increasing strain in the beam. This increase in stiffness is a nonlinear restoring force that reduces the positive feedback that leads to pull-in, and thus extends the range of stable travel. It was shown in [10] that this technique extended the stable travel distance to about 3/5 of the gap.

In addition to the structural modifications in the mechanical domain, alteration of the control voltages in the electrical domain has been used. Introduction of more complex actuating signals into the electrostatic actuator has resulted in so-called “pre-shaped control” [11]. Here, the dynamical model of the device is used to construct a pre-shaped input signal that improves the performance of the device. The pre-shaped driving technique significantly improves the dynamic behavior of the actuator. Even the pre-shaped actuation, however, is sometimes not sufficient. The lack of accurate models and

repeatability of the device parameters, compounded by special requirements on the dynamical behavior, have opened the possibility of closed-loop applications [11].

1.3.2 Linear Feedback Control

While MEMS devices are typically driven directly in an open loop fashion [11], there have been some attempts at simple linear control schemes. A charge control approach in [2] demonstrated an increased travel range up to 83% of the gap compared to mechanical compensation. One of the difficulties in utilizing a charge control scheme is that the effects of parasitic capacitances require a charge drive with extremely low leakage current. The design of a current drive with sufficiently low leakage currents can be challenging. The use of a voltage control scheme alleviates this problem and has been the focus of the majority of researchers in this area. This thesis will only focus on the voltage control technique.

Utilizing a voltage source with a capacitor in series with the electrostatic actuator [12-13] has proven successful. Figure 7 illustrates the general idea of this control technique.

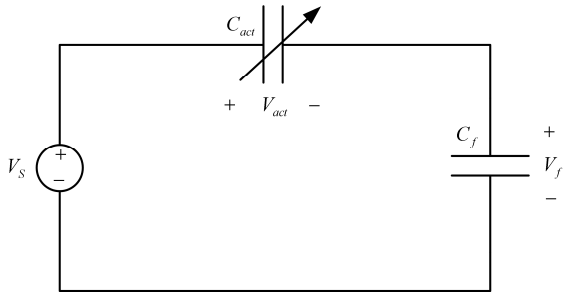

Figure 7: Voltage Control with Series Feedback Capacitor [12]

In Figure 7, V_S is the source voltage, V_{act} is the voltage across the electrostatic actuator (variable capacitor), and V_f is the voltage across the feedback capacitor C_f. From Figure 7, V_{act} is represented by (1.1).

$$V_{act} = \frac{V_{act}}{V_{act} + V_f} V_S . \tag{1.1}$$

The relation between the voltage and charge of a capacitor is given by

$$V = \frac{1}{C} q . \tag{1.2}$$

Substituting (1.2) into (1.1) yields

$$V_{act} = \frac{1}{1 + \frac{C_{act}}{C_f}} V_S , \tag{1.3}$$

where C_{act} is the capacitance of the actuator.

The capacitance of a parallel-plate capacitor is inversely proportional to the gap between the plates. If the source voltage is increased, the distance between the moveable plate of the electrostatic actuator and its fixed plate will decrease. Thus, the capacitance of the actuator will increase. Equation (1.3) shows that increasing C_{act} will cause the voltage across the actuator V_{act} to decrease. This decrease in voltage will cause the electrodes to separate from each other. The feedback capacitance C_f acts as a tuning parameter. The technique showed stable operations of the actuator at 30%, 60% and 90% of the nominal gap. The downside to this approach is that the uncertainty in the capacitance of the electrostatic actuator requires the C_f to be varied from device to

device in order to ensure a stable operating range. Therefore, it is dependent on an accurate model of the actuator. Another downside is that large actuation voltages are required.

The work of [14-16] utilized voltage control, position feedback and a phase optimization approach to design a Linear Time-Varying (LTV) proportional controller. The proportional gains were chosen at each displacement to maximize the phase margin. In addition to the LTV controller the authors in [14-16] designed a Linear Time-Invariant (LTI) proportional gain controller utilizing a Quantitative Feedback Theory (QFT) design methodology. The QFT is a frequency domain design technique that focuses on designing two-degree-of-freedom robust controllers utilizing design templates [17]. In the current literature, only the LTI controller introduced in [14-16] was implemented on actual hardware and was able to extend the traversal range to 60% of the gap.

The author in [14-16] suggested three reasons for the instability of the actuator above 60% of the gap. The first reason was that a reduced damping coefficient due to plate tilt resulted in reduced phase margins.

Since this thesis assumes a 1-DOF model of the actuator with vertical displacement, the problem proposed in [17] will be disregarded. A reason causing the instability of the actuator was the magnification of sensor noise [14-16]. It was noted that a large loop gain at frequencies for which the plant gain is small results in large noise amplification at the controller output (plant input). The situation of noise amplification is worsened when the DC gain of the actuator reduces as the plate displacement increases. A pure proportional controller design in [14-16] cannot attenuate the effects of high frequency noises enough to ensure the input to the plant did not saturate. This is one area

that we can improve upon the designs in [14-16]. We will definitely see the effects of sensor noise in the remaining parts of the thesis.

In addition, the proportional gain controller [14-16] failed to stabilize the electrostatic actuator over the entire gap under underdamped and slightly overdamped situations. The use of phase lead could rectify this problem at the expense of increased bandwidth and thus increased sensor noise.

It was also noted that the controller gain in [14-16] could be reduced through two ways. One way is to increase the actuator gain by increasing the area of the capacitor's plates. Another way is to decrease the distance of the unstable pole from the $j\omega$ axis by increasing the damping and/or reducing the mechanical bandwidth.

1.3.3 Nonlinear Feedback Control

More recently the application of nonlinear control approaches has emerged. Three of these approaches are flatness based control, Control Lyapunov Function (CLF) synthesis, and back-stepping design [17]. The nonlinear control approaches are further extended to the actuator models with parasitic capacitance [18]. In [18], two robust controllers are constructed, both based on the theory of input-to-state stabilization and back-stepping state feedback design. The designs of these controllers take two forms of uncertainty into account. The first type of uncertainty is the variation of the parasitic capacitance due to layout, fringing field, or the deformation of the movable plate. The second type of uncertainty is due to the variation of mechanical and electrical parameters such as the damping ratio and the resistance in the loop. Simulation results in [18]

demonstrate 90% gap traversal with minimal overshoot in the presence of parameter variations. The rise time is approximately 5 normalized time units with a control signal approximately twice the pull-in voltage.

In [4], it is shown that an electrostatic actuator is differentially flat. The authors in [4] use this fact to incorporate trajectory planning into nonlinear robust control to extend the travel range up to 100% of the gap. The term "differentially flat" implies that all the other states as well as the input can be obtained from the position state and its derivatives. Thus any reference trajectory can then be computed without integrating the corresponding differential equation. This allows the authors in [4] to make a time independent controller that runs in an "auto-scheduling" fashion. This design procedure is simulated on underdamped, critically damped, and overdamped actuator models and compared against a charge control scheme. The actuator displacement is controlled to be 20%, 40%, 60%, 80% and 100% of the full gap respectively. The normalized deflection shows no overshoot and the control voltage is kept within ±3 normalized control units. A 5% of the full gap disturbance of position is rejected, albeit with a large actuation voltage. Nevertheless, sensor noise is not included in the simulations in [4].

In general, the approaches in [4, 12-18] are effective, but their utility is somewhat offset by their mathematical complexity and their lack of noise attenuation. Furthermore, additional electrodes or sensors for measuring position are required [11] in order to use feedback to stabilize the actuator in [4, 12-18].

1.4 Proposed Control Methods

This thesis will present three linear, closed-loop control designs. All three of these designs are going to be formulated in the frequency domain. The three designs assume different levels of knowledge about the actuator plant to be controlled. The three controller designs will utilize the implementation of an Active Disturbance Rejection Controller (ADRC). ADRC handles unknown system dynamics effectively by treating them as an unknown disturbance and canceling them out in the control law. ADRC was chosen because the electrostatic actuator has a great deal of model uncertainty over its operating range. This controller design methodology appears to be a perfect fit for the control problems presented by the electrostatic actuator.

In the first approach, it is assumed that there is no detailed mathematical model of the electrostatic actuator available. The order of the model and the gain of the actuator are the only known parameters. It is also assumed there is only one measured output, which is the displacement of the moveable plate of the actuator. An ADRC with a 4^{th} order Extended State Observer (ESO) is going to be designed to control the electrostatic actuator. The nominal model of the electrostatic actuator in this design is going to be a third-order integrator.

The second design example assumes that partial knowledge of the actuator plant is available. In this case only the parameters that vary significantly over the operating range of the electrostatic actuator are considered unknown. It is also assumed that the displacement output of the actuator is measurable. This design will also utilize ADRC

with a 4^{th} order ESO. The known modeling information is utilized and included into the ESO yielding a type 1, third order nominal plant.

The third design is a multi-loop control design requiring two measured outputs, which are the displacement output and the charge output of the actuator. This design will employ ADRC with a 2^{nd} order ESO for the inner loop to control the charge output, along with a PI controller for the outer loop to control the displacement output.

1.5 Overview

The remaining parts of this thesis will be organized as follows.

Chapter 2 develops the mathematical modeling of a MEMS electrostatic actuator. A nonlinear actuator model suitable for control design will be developed. This model will then be normalized before being linearized. Finally the behavior of the linearized actuator model is investigated.

Chapter 3 introduces some control basics and control laws that will be used throughout this thesis. An ADRC in the state space formulation is described as a basis for a frequency domain formulation of the ADRC. State observers are investigated in the frequency domain. Finally, the frequency domain implementation of the ADRC is derived.

Chapter 4 talks about linear control designs. The three different control designs described previously are developed in this chapter. Performance and stability analyses will be conducted based on these three control designs.

Chapter 5 provides simulation results of the control designs on both the linearized and the nonlinear models of the actuator. Noise attenuation is demonstrated and a comparison of the performances of the three controller designs is conducted in the chapter.

Chapter 6 will offer conclusions and suggest future research directions.

CHAPTER II

MATHEMATICAL MODELING

This chapter will discuss the derivation of a simplified mathematical model of an electrostatic actuator that is suitable for control system design. The first section will introduce the basic physical principles involved in the operation of the electrostatic actuator. Two different modeling approaches will be presented in the section. They are based on first principles and the Lagrange equation respectively. The first-principle-based modeling will use force balance equations to determine the mathematical model. The Lagrange method will utilize the concept of energy to derive the same model. The second section will introduce the normalization of the nonlinear equations derived through the two modeling approaches. The second section will be followed by model linearization, transfer function representation, and the model behavior of the electrostatic actuator.

2.1 Mathematical Modeling

MEMS electrostatic actuators are generally divided into two varieties, comb-drive and parallel-plate. This thesis will focus on the latter. The key model component of a parallel-plate electrostatic actuator is the parallel-plate capacitor as shown in Figure 8.

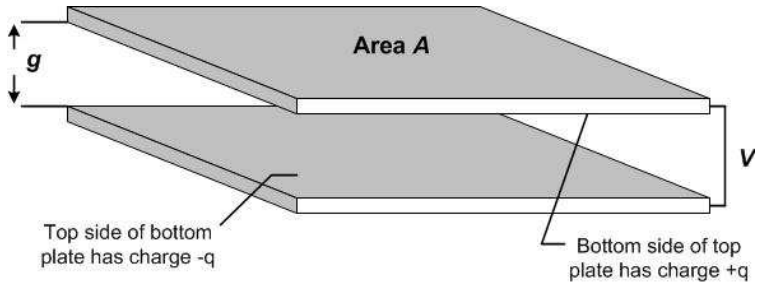

Figure 8: Parallel-Plate Capacitor

A parallel-plate capacitor has two electrodes (plates) of equal area (A) separated by a gap (g). When a voltage (V) is applied across the upper and lower plates of the actuator an equal and opposite charge (Q) builds on the upper and lower plates. Because of the opposite charges on the two plates, there is a force of attraction (electrostatic force) between the two plates [1]. The charge Q and the voltage V are proportional to each other and are related by the capacitance. This relationship between the charge and voltage is given by (2.1).

$$Q = CV \tag{2.1}$$

The capacitance, denoted by (2.2), of a parallel-plate capacitor depends both on the area of one plate and the distance between them.

$$C = \frac{\varepsilon A}{g} \tag{2.2}$$

In (2.2), ε is the permittivity of the air between the plates, g is the gap between the two plates and A is the area of the capacitor's plate. As can be seen in (2.2) capacitance depends only on the capacitor's geometry, not on the applied voltage or the accumulated charge. Increasing the plate area or decreasing the gap between the two plates are the only ways to change the capacitance.

To determine the stored potential energy (W) between the plates of the capacitor, one can take the integral of the instantaneous power as given in (2.3).

$$W(Q) = \int VI \, dt \tag{2.3}$$

The equation for the potential energy in (2.3) can be simplified by using the fact that $I = dQ/dt$. Then (2.3) can be rewritten as (2.4).

$$W(Q) = \int \left(\frac{1}{C} Q \right) \frac{dQ}{dt} \, dt \tag{2.4}$$

Performing the integration in (2.4) results in (2.5).

$$W(Q) = \frac{1}{2C} Q^2 \tag{2.5}$$

In a fixed-plate capacitor, the input voltage can be varied so as to change the amount of charge accumulated on the faces of the plates. The electrostatic force that acts on the two plates is of no great concern for the fixed-plate capacitor. In an electrostatic actuator, one of the electrodes is free to move. This allows the use of the accumulated charge as an intermediate variable that can be used to control the gap between the two

plates. In the following discussion it will be assumed that it is the upper electrode that is movable. Once the upper electrode moves, one must account for the dynamics this moveable plate introduces. The time-varying dependence of the capacitance on the change in gap is represented by (2.6).

$$C(t) = \frac{\varepsilon A}{g(t)} \tag{2.6}$$

From (2.5) and (2.6), the energy stored in an electrostatic actuator is a function of an electrical variable (charge) and a mechanical variable (displacement). One can use the principle of virtual work to model this actuator system. Imagine that the spacing of the plates is increased by the small amount Δg, the mechanical work done by moving the plates would be

$$\Delta W(g) = F\Delta g\,. \tag{2.7}$$

In (2.7), the variable F represents the electrostatic force acting between the plates. This work must be equal to the change in the electrostatic energy of the capacitor. The energy of the capacitor was originally

$$W(Q) = \frac{1}{2C}Q^2\,. \tag{2.8}$$

The change in energy (holding the charge constant) is

$$\Delta W(Q) = \frac{1}{2}Q^2\Delta\left(\frac{1}{C}\right). \tag{2.9}$$

Setting (2.7) equal to (2.9) yields

$$F\Delta g = \frac{1}{2}Q^2\Delta\left(\frac{1}{C}\right). \tag{2.10}$$

Equation (2.10) can be rewritten as

$$F\Delta g = -\frac{Q^2}{2C^2}\Delta C\,. \tag{2.11}$$

From (2.2) the inverse of the capacitance is

$$\left(\frac{1}{C}\right) = \frac{g}{\varepsilon A}\,. \tag{2.12}$$

The change in the capacitance can be related to the change in gap as in (2.13).

$$\Delta\left(\frac{1}{C}\right) = \frac{\Delta g}{\varepsilon A} \tag{2.13}$$

Utilizing (2.10) and (2.13) the electrostatic force can be written as

$$F = \frac{Q^2}{2\varepsilon A}\,. \tag{2.14}$$

The electrostatic force is proportional to the square of the charge.

The fact that the stored energy is a function of charge and gap leads to the realization of a two-port capacitor to describe this electrostatic actuator, in which one port denotes the electrical domain and the other port denotes the mechanical domain. The actuator can convert electrical energy into mechanical energy, and vice versa [19]. Figure 9 gives a graphical representation of this two-port actuator.

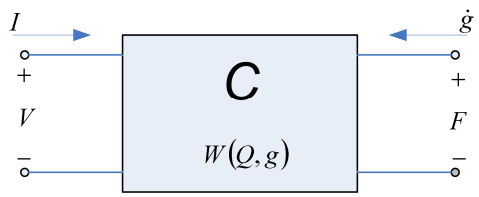

Figure 9: Two Port Capacitor [6]

In Figure 9, $W(Q,g)$ represents the potential energy stored in this device. Both mechanical and electrical stored potential energy is included in the two port capacitor.

A simplified one-degree-of-freedom electrostatic actuator model was selected based on [6]. The electro-mechanical model of the actuator is shown in Figure 10.

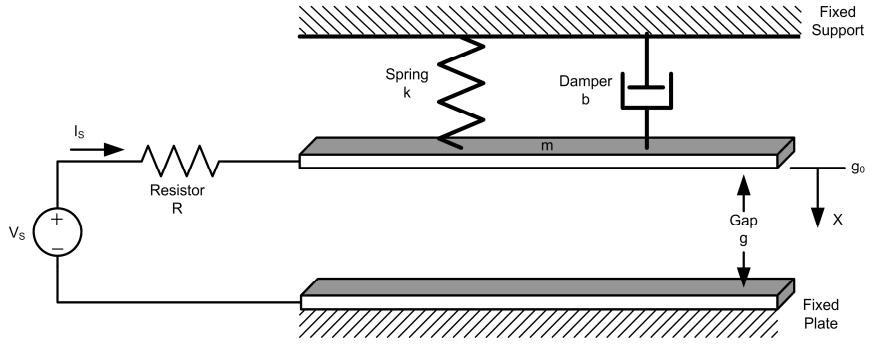

Figure 10: Electrostatic Actuator Model [6]

From Figure 10, we can see that an electrostatic actuator consists of a parallel-plate capacitor with one fixed electrode and one varying electrode. The input voltage source V_S is modeled with a series source resistance, *R*. The variable I_S is the input current. The gap with zero applied voltage is denoted by g_0. The gap *g* is positive in the direction of increasing gap, while *X* is the displacement of the moving plate and *X* is positive in the direction of decreasing gap. The relationship between *g* and *X* is given by

$$g = g_0 - X \tag{2.15}$$

As the charge on the two plates builds, the force of attraction grows, bringing the plates closer together. In order to keep the plates from "snapping down," there needs to be an equal and opposite force resisting this motion. This force is modeled by the restoring force of a mechanical spring with spring constant *k*. A damping term, *b*,

represents the squeezed-film damping coefficient. It should now be clear that this device is operating in two energy domains, electrical and mechanical. For analytical purposes this electromechanical system will be divided into three parts, a purely electrical part, a purely mechanical part and a coupling part as shown in Figure 11.

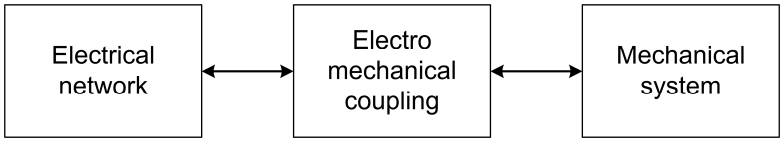

Figure 11: An Electromechanical System [20]

Figure 12 shows an equivalent circuit model of a decoupled electrostatic actuator.

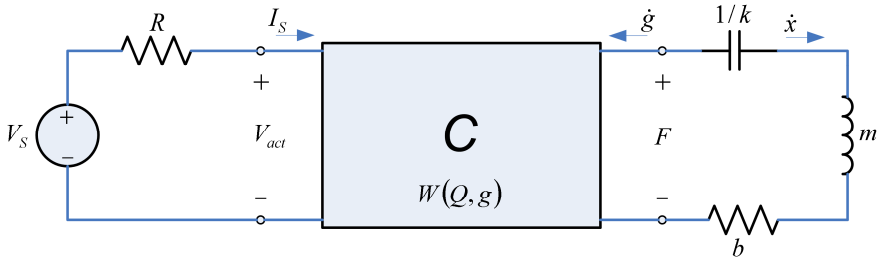

Figure 12: An Equivalent Circuit Model of the Electrostatic Actuator [6]

From Figure 12, the mechanical sub-system of the actuator is modeled as an equivalent series RLC circuit. This is due to the fact that the damper, mass, and spring share the same displacement. The equivalent circuit for the electrical sub-system is modeled as a voltage source in series with a source resistance. The two-port capacitor provides a description for the electro-mechanical coupling. The equations that describe both energy domains and the coupling that occurs between them will be derived in the next section.

2.1.1 First Principles Modeling

First principles modeling for the electrostatic actuator involves using Newton's laws of motion in the mechanical domain and Kirchoff's Current and Voltage Laws in the electrical domain. This method of modeling deals with force vectors as opposed to the energy method used in the Lagrangian method. Modeling in the mechanical domain begins with the free-body diagram of the electrostatic actuator as shown in Figure 13.

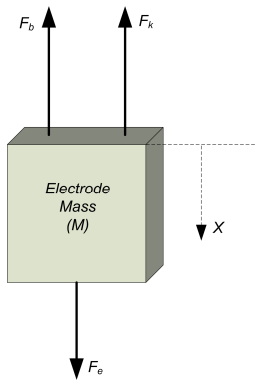

Figure 13: A Free-body Diagram of the Electrostatic Actuator

According to Newton's 2nd law, we have,

$$m\ddot{X} = F_e - F_b - F_k\,, \tag{2.16}$$

where $F_b = b\dot{X}$ is the linear squeeze film damping force, $F_k = kX$ is the linear mechanical spring force and $F_e = Q^2 / 2\varepsilon A$ is the nonlinear electrostatic force. Equation (2.16) can be rewritten as

$$m\ddot{X} = \frac{Q^2}{2\varepsilon A} - b\dot{X} - kX\,. \tag{2.17}$$

Note that the scale of the model is measured in microns. Thus the mass of the upper plate of the capacitor is so small that the gravitational force acting on the actuator can be neglected.

Now considering the electrical domain, the current through the series resistor R can be obtained by the application of Kirchoff's Voltage Law (KVL). Applying the KVL to the actuator's electrical model gives

$$I_S = \frac{1}{R}\left(V_S - V_{act}\right), \tag{2.18}$$

where V_{act} is the voltage across the capacitor plates. Utilizing the relation $Q = CV$ and (2.2) the voltage across the actuator can be represented by

$$V_{act} = \frac{Qg}{\varepsilon A}. \tag{2.19}$$

The current can be solved by substituting (2.19) into (2.18). Using the fact $I_S = \dot{Q}$, we have

$$\dot{Q} = \frac{1}{R}\left(V_S - \frac{Qg}{\varepsilon A}\right). \tag{2.20}$$

One now needs to relate the gap g to the displacement X. This relation is given in (2.15). Substituting (2.15) into (2.20) leaves

$$\dot{Q} = \frac{1}{R}\left(V_S - \frac{Q\left(g_0 - X\right)}{\varepsilon A}\right). \tag{2.21}$$

Equations (2.17) and (2.21) constitute the mathematical model of the electrostatic actuator.

2.1.2 Lagrange's Equations

The principle of Lagrange's equations is based on a quantity called the Lagrangian, and is stated as follows: For a dynamic system in which the work of all forces is accounted for in the Lagrangian, an admissible motion between specific configurations of the system at time t_1 and t_2 is a natural motion if, and only if, the energy of the system remains constant.

The Lagrangian is a quantity that describes the balance between kinetic and potential energies (excluding dissipative energies). In particular, it is written

$$L = K_e - V_e, \tag{2.22}$$

where L denotes the Lagrangian quantity, K_e is the kinetic energy, and V_e is the potential energy.

The Lagrange equation is given by

$$\frac{d}{dt}\left(\frac{\partial L}{\partial \dot{q}_i}\right) - \frac{\partial L}{\partial q_i} + \frac{\partial P}{\partial \dot{q}_i} = F_i. \tag{2.23}$$

In (2.23), P denotes the power function (describing the dissipation of energy in the system), F_i generalized external inputs (forces) acting on the system (for the electrostatic actuator, the external input is the source voltage V_S), and q_i the generalized coordinates of the system (for the electrostatic actuator, they will be the charge Q and the displacement X). A lumped-parameter model of an electrostatic actuator is derived as below.

The kinetic energy for the system is given by

$$K_e = \frac{1}{2} m\dot{X}^2, \tag{2.24}$$

where m is the mass of the upper movable plate. The potential energy V_e represented by (2.25) has electrical and mechanical components due to the capacitance and the restoring spring respectively.

$$V_e = \underbrace{\frac{1}{2C} Q^2}_{capacitor} + \underbrace{\frac{1}{2} kX^2}_{spring} \tag{2.25}$$

As noted previously, in this system, the capacitance is not a constant, but a nonlinear function of X, as shown in (2.26).

$$C = \frac{\varepsilon A}{g_0 - X} \tag{2.26}$$

Substituting (2.26) into (2.25) yields

$$V_e = \frac{1}{2\varepsilon A}(g_0 - X)Q^2 + \frac{1}{2} kX^2. \tag{2.27}$$

The power dissipation function P includes both electrical and mechanical parts due to the source resistance and squeeze-film damping and it is given by (2.28).

$$P = \underbrace{\frac{1}{2} R\dot{Q}^2}_{resistor} + \underbrace{\frac{1}{2} b\dot{X}^2}_{damper}. \tag{2.28}$$

Combining (2.24) and (2.27) produces the Lagrangian as follows.

$$L = \underbrace{\frac{1}{2} m\dot{X}^2}_{kinetic} - \underbrace{\frac{1}{2\varepsilon A}(g_0 - X)Q^2 - \frac{1}{2} kX^2}_{potential} \tag{2.29}$$

The Lagrange equation (2.23) shows that we must take the partial derivatives of (2.28) and (2.29) with respect to the generalized coordinates X and Q and their first derivatives. The results of these partial derivatives are shown in (2.30) and (2.31).

$$\frac{\partial L}{\partial \dot{X}} = m\dot{X}\ , \quad \frac{\partial L}{\partial X} = \frac{Q^2}{2\varepsilon A} - kX\ , \quad \frac{\partial P}{\partial \dot{X}} = b\dot{X} \tag{2.30}$$

$$\frac{\partial L}{\partial \dot{Q}} = 0\ , \quad \frac{\partial L}{\partial Q} = \frac{(g_0 - X)Q}{\varepsilon A}\ , \quad \frac{\partial P}{\partial \dot{Q}} = R\dot{Q} \tag{2.31}$$

The time derivatives of the partial derivatives of the Lagrangian with respect to the time derivatives of the generalized coordinates are given by (2.32)

$$\frac{d}{dt}\left(\frac{\partial L}{\partial \dot{q}_i}\right) \tag{2.32}$$

Performing the operation of (2.32) on the applicable terms in (2.30) and (2.31) results in

$$\begin{aligned} \frac{d}{dt}\left(\frac{\partial L}{\partial \dot{X}}\right) &= \frac{d}{dt}\left(m\dot{X}\right) = m\ddot{X} \\ \frac{d}{dt}\left(\frac{\partial L}{\partial \dot{Q}}\right) &= \frac{d}{dt}(0) = 0 \end{aligned} \quad . \tag{2.33}$$

Substituting (2.30), (2.31) and (2.33) into (2.23) yields

$$\begin{aligned} m\ddot{X} + b\dot{X} + kX - \frac{1}{2\varepsilon A}Q^2 &= 0 \\ R\dot{Q} + \frac{1}{\varepsilon A}(g_0 - X)Q &= V_S \end{aligned} \quad . \tag{2.34}$$

Equation (2.34) gives the differential equations (nonlinear model) describing the dynamics of the electrostatic actuator.

2.2 Equation Normalization

This section will present the results of the normalization of the nonlinear model of the actuator. The normalized equations can simplify the later performance analysis and controller design for the electrostatic actuator. It will also allow for a direct comparison between the controller performance in this thesis and the one in the references [4, 17-18]. More details about the normalization procedure can be found in Appendix A.

2.2.1 Normalization Results of the Nonlinear Model of the Electrostatic Actuator

The position of the upper plate relative to the lower plate (X), time (t), the charge built up on the plates (Q), the voltage across the plates (V_{act}), and the source voltage (V_S) are normalized as shown in (2.35)

$$x = \frac{X}{g_0} \quad \tau = \omega_0 t \quad q = \frac{Q}{q_{pi}} \quad v_{act} = \frac{V_{act}}{v_{pi}} \quad v_s = \frac{V_s}{v_{pi}} \tag{2.35}$$

In (2.35) the displacement is normalized by the gap with zero applied voltage (g_0), time is normalized by the natural frequency (ω_0) of the actuator, charge is normalized by the accumulation of charge at pull-in (q_{pi}), the voltage across the actuator and the source voltage are both normalized by the pull-in voltage (v_{pi}). From [4] the equations that govern the pull-in voltage, the amount of charge at pull-in and the capacitance at zero gap are given in (2.36).

$$q_{pi} = \frac{3}{2} C_0 v_{pi} \quad v_{pi} = \sqrt{\frac{8kg_0^2}{27C_0}} \quad C_0 = \frac{\varepsilon A}{g_0} \tag{2.36}$$

From Appendix A, the results of the normalization of (2.34) are given in (2.37) and (2.38).

$$\ddot{x} + 2\varsigma\dot{x} + x = \frac{1}{3}q^2 \tag{2.37}$$

$$\dot{q} + \frac{1}{r}(1-x)q = \frac{2}{3r}v_s \tag{2.38}$$

In (2.37) and (2.38), the variables ς, ω_0 and r are defined as follows.

$$\varsigma = \frac{b}{2m\omega_0} \qquad \omega_0 = \sqrt{\frac{k}{m}} \qquad r = \omega_0 RC_0 \tag{2.39}$$

2.3 Model Linearization

In order to simplify the controller design, the nonlinear model of the electrostatic actuator needs to be linearized. The linearized model will be used to determine local stability of an equilibrium point of the actuator system.

2.3.1 Standard Model

We choose the state variables of the normalized model of the actuator as *x(t)*, *q(t)*, and *s(t)*, where *s(t)* is the velocity of the movable plate of the actuator, i.e. $s(t) = \dot{x}(t)$. For small-signal linearization, the equilibrium values of the state variables, which are represented by X_{eq}, Q_{eq}, and S_{eq}, have to be determined so that all the state equations

associated with the state variables are equal to zero. Then the nonlinear equation will be expanded in terms of perturbations from these equilibrium values.

Each state variable can be decomposed into the equilibrium value of the state variable and a deviation variable from the equilibrium value as shown in (2.40), where $\delta x(t)$ is the deviation variable for *x(t)*, $\delta q(t)$ is the deviation variable for *q(t)*, and $\delta v(t)$ is the deviation variable for *v(t)*.

$$\begin{aligned} x(t) &= X_{eq} + \delta x(t) \\ q(t) &= Q_{eq} + \delta q(t) \\ v(t) &= V_{eq} + \delta v(t) \end{aligned} \tag{2.40}$$

If the state variables are represented in terms of the deviation variables, one can define the following three states for the electrostatic actuator:

$$\begin{aligned} x_1(t) &= x(t) - X_{eq} \\ x_2(t) &= s(t) - S_{eq} \\ x_3(t) &= q(t) - Q_{eq} \end{aligned}, \tag{2.41}$$

where $x_1(t)$ denotes $\delta x(t)$, $x_2(t)$ denotes $\delta s(t)$, and $x_3(t)$ denotes $\delta q(t)$. The explicit time dependence will be eliminated in future equations for brevity. Incorporating the new state variables defined by (2.41) into the nonlinear equations (2.37) and (2.38) yields the state equations (2.42) of the normalized actuator model.

$$\begin{aligned} \dot{x}_1 &= x_2 = f_1 \\ \dot{x}_2 &= -x_1 - 2\varsigma x_2 + \frac{1}{3}x_3^2 = f_2 \\ \dot{x}_3 &= -\frac{1}{r}(1 - x_1)x_3 + \frac{2}{3r}v_s = f_3 \end{aligned} \quad . \tag{2.42}$$

The equilibrium points are determined by solving (2.43).

$$\begin{aligned}\dot{x}_1 &= x_2 = 0 \\ \dot{x}_2 &= -x_1 - 2\zeta x_2 + \frac{1}{3}x_3^2 = 0 \\ \dot{x}_3 &= -\frac{1}{r}(1-x_1)x_3 + \frac{2}{3r}v_s = 0\end{aligned} \tag{2.43}$$

Setting f_1 equal to zero, one can see that S_{eq} will be zero. This simplifies f_2, as in (2.44), which can be used to solve for the equilibrium gap.

$$X_{eq} = \frac{1}{3}Q_{eq}^2 \tag{2.44}$$

Recalling the normalization of these equations, one can do a quick check by setting the charge $Q_{eq} = 1$, the pull-in gap will become 1/3, as expected. Substituting (2.44) into the equation for f_3 yields

$$Q_{eq}^3 - 3Q_{eq} + 2v_s = 0\,. \tag{2.45}$$

There are three possible solutions to the equilibrium charge. One of the solutions is negative for a positive input voltage and can thus be disregarded. The other two solutions hint at the fact that there are two equilibrium positions for each input voltage. One of these operating points will be stable and the other will be unstable. When the pull-in voltage is reached, the two solutions will be repeated, suggesting there is only one unstable equilibrium point. In order to solve for these equilibrium points (2.44) and (2.45) must be used to relate the displacement to the input voltage. This is performed in the equation development as follows.

Equation (2.45) can be rewritten as (2.46).

$$Q_{eq}\left(Q_{eq}^2 - 3\right) + 2v_s = 0 \tag{2.46}$$

Substituting (2.44) into (2.46) gives (2.47).

$$Q_{eq}\left(3X_{eq}-3\right)+2v_s=0 \tag{2.47}$$

Equation (2.47) can be rewritten as (2.48).

$$Q_{eq}=\frac{2}{3\left(1-X_{eq}\right)}v_s \tag{2.48}$$

From (2.48), we have

$$Q_{eq}^2=\frac{4}{9\left(1-X_{eq}\right)^2}v_s^2. \tag{2.49}$$

Substituting (2.44) into (2.49), we have

$$X_{eq}=\frac{4}{27\left(1-X_{eq}\right)^2}v_s^2. \tag{2.50}$$

The left side of (2.50) gives the spring force (as $k = 1$), the right side gives the electrostatic force. Figure 14 illustrates the relationship between the spring force (solid line) and the electrostatic force (dashed line) in (2.50) as the input voltage v_s varies. Particularly the figure shows both stable and unstable equilibrium points which are the intersections between the straight line of the spring force and the curves of the electrostatic forces as the input voltages are *0.6*, *0.8*, and *1*.

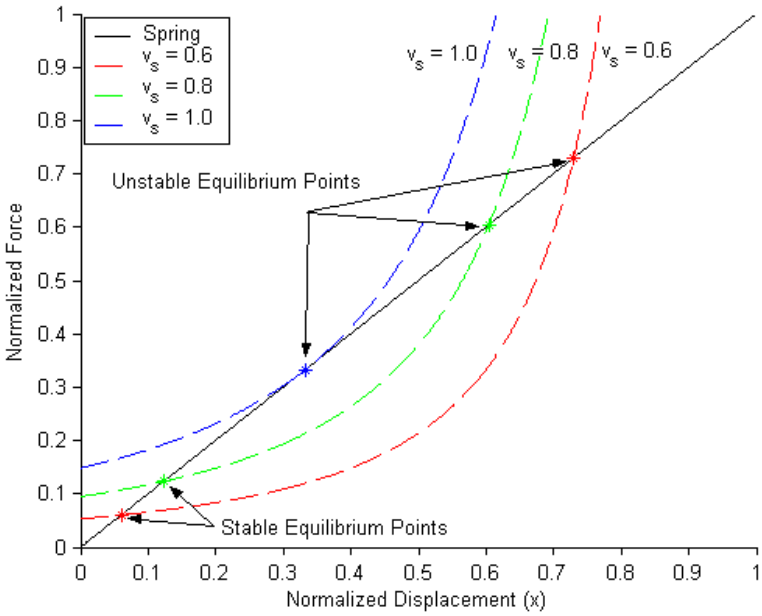

Figure 14: Stable and Unstable Equilibrium Points

From Figure 14, we can see that for normalized input voltages ($v_S = 0.6$ and 0.8) below the normalized pull-in voltage $(v_{pi} = 1)$ there are two equilibrium positions, one stable and one unstable. For normalized displacements less than *1/3* of the full gap, perturbing the equilibrium displacement will result in the actuator returning to its equilibrium point. The restoring force of the linear spring is greater than the electrostatic force in the direction of increased displacement. As the normalized displacements are greater than or equal to *1/3* of the full gap, a perturbation in position will result in the electrostatic force dominating the linear spring force. Thus pull-in instability will occur. As the normalized pull-in voltage is reached $(v_s = v_{pi} = 1)$ there will be only one unstable equilibrium point as shown in Figure 14. Any voltage applied above the pull-in voltage will result in zero equilibrium points.

As long as the equilibrium points are found, the nonlinear model (2.43) of the electrostatic actuator will be linearized around the equilibrium values. The linearized model is given in (2.51), where V represents the control voltage input.

$$\begin{bmatrix} \delta\dot{x}_1 \\ \delta\dot{x}_2 \\ \delta\dot{x}_3 \end{bmatrix} = \left[\begin{matrix} \frac{\delta f_1}{\delta x_1} & \frac{\delta f_1}{\delta x_2} & \frac{\delta f_1}{\delta x_3} \\ \frac{\delta f_2}{\delta x_1} & \frac{\delta f_2}{\delta x_2} & \frac{\delta f_2}{\delta x_3} \\ \frac{\delta f_3}{\delta x_1} & \frac{\delta f_3}{\delta x_2} & \frac{\delta f_3}{\delta x_3} \end{matrix} \right]_{X_{eq}, S_{eq}, Q_{eq}} \begin{bmatrix} \delta x_1 \\ \delta x_2 \\ \delta x_{31} \end{bmatrix} + \left[\begin{matrix} \frac{\delta f_1}{\delta U} \\ \frac{\delta f_2}{\delta U} \\ \frac{\delta f_3}{\delta U} \end{matrix} \right]_{X_{eq}, S_{eq}, Q_{eq}} \delta V \qquad (2.51)$$

Performing each of the partial derivatives in (2.51) produces Table I, in which $X_1 = X_{eq}$, and $X_3 = Q_{eq}$.

TABLE I: PARTIAL DERIVATIVES

$$\frac{\delta f_1}{\delta x_1} = 0 \qquad \frac{\delta f_1}{\delta x_2} = 1 \qquad \frac{\delta f_1}{\delta x_3} = 0 \qquad \frac{\delta f_1}{\delta v} = 0$$

$$\frac{\delta f_2}{\delta x_1} = -1 \qquad \frac{\delta f_2}{\delta x_2} = -2\zeta \qquad \frac{\delta f_2}{\delta x_3} = \frac{2}{3} X_3 \qquad \frac{\delta f_2}{\delta v} = 0$$

$$\frac{\delta f_3}{\delta x_1} = \frac{1}{r} X_3 \qquad \frac{\delta f_3}{\delta x_2} = 0 \qquad \frac{\delta f_3}{\delta x_3} = \frac{1}{r}(X_1 - 1) \qquad \frac{\delta f_3}{\delta v} = \frac{2}{3r}$$

The output of this electrostatic actuator is δx_1. Then from (2.51) and Table I, a complete linearized model of the electrostatic actuator along with the output equation can be written as (2.52).

$$\begin{bmatrix} \delta\dot{x}_1 \\ \delta\dot{x}_2 \\ \delta\dot{x}_3 \end{bmatrix} = \underbrace{\begin{bmatrix} 0 & 1 & 0 \\ -1 & -2\varsigma & \frac{2}{3}X_3 \\ \frac{1}{r}X_3 & 0 & \frac{1}{r}(X_1 - 1) \end{bmatrix}}_{A} \begin{bmatrix} \delta x_1 \\ \delta x_2 \\ \delta x_{31} \end{bmatrix} + \underbrace{\begin{bmatrix} 0 \\ 0 \\ \frac{2}{3r} \end{bmatrix}}_{B} \delta U$$

$$\delta y = \underbrace{\begin{bmatrix} 1 & 0 & 0 \end{bmatrix}}_{C} \begin{bmatrix} \delta x_1 \\ \delta x_2 \\ \delta x_{31} \end{bmatrix} \tag{2.52}$$

In (2.52), the Jacobian matrices (A and B) and output matrix are defined as (2.53).

$$A = \begin{bmatrix} 0 & 1 & 0 \\ -1 & -2\varsigma & \frac{2}{3}X_3 \\ \frac{1}{r}X_3 & 0 & \frac{1}{r}(X_1 - 1) \end{bmatrix} \quad B = \begin{bmatrix} 0 \\ 0 \\ \frac{2}{3r} \end{bmatrix} \quad C = \begin{bmatrix} 1 & 0 & 0 \end{bmatrix}. \tag{2.53}$$

2.4 Transfer Function Derivation

For the convenience of future frequency-domain analysis a transfer function representation of the linearized electrostatic actuator model will be derived in the following subsection.

2.4.1 Linearized Actuator Model

The state space representation of the electrostatic actuator derived in (2.52) is repeated below in (2.54)

$$\begin{bmatrix} \delta\dot{x}_1 \\ \delta\dot{x}_2 \\ \delta\dot{x}_3 \end{bmatrix} = \begin{bmatrix} 0 & 1 & 0 \\ -1 & -2\varsigma & \frac{2}{3}X_3 \\ \frac{1}{r}X_3 & 0 & \frac{1}{r}(X_1 - 1) \end{bmatrix} \begin{bmatrix} \delta x_1 \\ \delta x_2 \\ \delta x_3 \end{bmatrix} + \begin{bmatrix} 0 \\ 0 \\ \frac{2}{3r} \end{bmatrix} \delta V \tag{2.54}$$

Taking the Laplace transform of the linearized differential equation (assuming zero initial conditions) for the displacement gives:

$$s^2 X(s) = -X(s) - 2\varsigma s X(s) + \frac{2}{3} Q_{eq} Q(s), \tag{2.55}$$

where $Q(s)$ is the charge on the plates, $X(s)$ is the displacement of the movable plate.

Equation (2.55) can be reduced further to

$$X(s) = \frac{2Q_{eq}}{3(s^2 + 2\varsigma s + 1)} Q(s). \tag{2.56}$$

The Laplace transform of the charge equation yields

$$rsQ(s) = Q_{eq} X(s) - (1 - X_{eq}) Q(s) + \frac{2}{3} V(s), \tag{2.57}$$

where $V(s)$ is the source voltage. Equation (2.57) can be reduced to

$$Q(s) = \frac{Q_{eq}}{(rs + (1 - X_{eq}))} X(s) + \frac{2}{3(rs + (1 - X_{eq}))} V(s). \tag{2.58}$$

Equations (2.56) and (2.58) can be visually represented by a block diagram as shown in Figure 15.

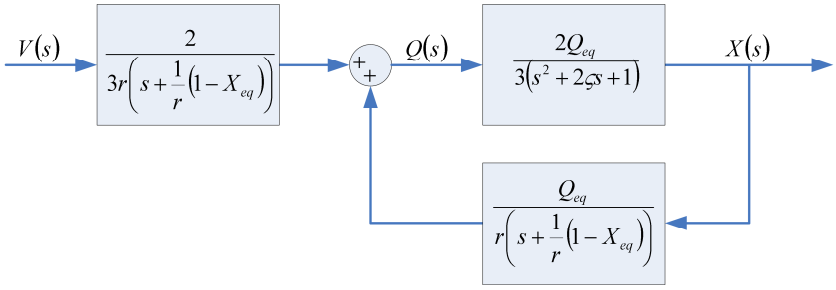

Figure 15: Transfer Function Equivalent Model of the Electrostatic Actuator

The block diagram in Figure 15 can be simplified as the one in Figure 16, where $V_{act}(s)$ provides positive feedback and acts as a destabilizing signal.

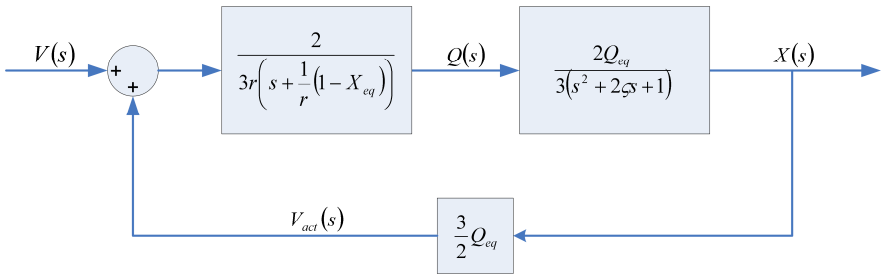

Figure 16: Simplified Transfer Function Equivalent Model

Substituting (2.58) into (2.56) gives

$$X(s)=\frac{2Q_{eq}}{3\left(s^2+2\zeta s+1\right)}\left[\frac{Q_{eq}}{\left(rs+\left(1-X_{eq}\right)\right)}X(s)+\frac{2}{3\left(rs+\left(1-X_{eq}\right)\right)}V(s)\right]. \tag{2.59}$$

Factoring out the common denominator of (2.59) yields

$$X(s)=\frac{2Q_{eq}}{3\left(s^2+2\zeta s+1\right)\left(rs+\left(1-X_{eq}\right)\right)}\left[Q_{eq}X(s)+\frac{2}{3}V(s)\right]. \tag{2.60}$$

In order to simplify (2.60), we define $G(s)$ as

$$G(s)=\frac{1}{3\left(s^2+2\zeta s+1\right)\left(rs+\left(1-X_{eq}\right)\right)}. \tag{2.61}$$

Substituting (2.61) into (2.60) leaves

$$X(s) = 2Q_{eq}G(s)\left[Q_{eq}X(s) + \frac{2}{3}V(s) \right]. \tag{2.62}$$

Collecting the displacement terms in (2.62) produces (2.63).

$$\left(1 - 2Q_{eq}^2 G(s)\right)X(s) = 2Q_{eq}G(s)\left[\frac{2}{3}V(s) \right] \tag{2.63}$$

From (2.63), we can get the transfer function between $X(s)$ and $V(s)$ as given in (2.64).

$$\frac{X(s)}{V(s)} = \frac{4Q_{eq}G(s)}{3\left(1 - 2Q_{eq}^2 G(s)\right)} \tag{2.64}$$

Equation (2.64) can be rewritten as

$$\frac{X(s)}{V(s)} = \frac{4Q_{eq}}{3\left(G^{-1}(s) - 2Q_{eq}^2\right)}. \tag{2.65}$$

The inverse of (2.61) is

$$G^{-1}(s) = 3\left(s^2 + 2\varsigma s + 1\right)\left(rs + \left(1 - X_{eq}\right)\right). \tag{2.66}$$

Substituting (2.66) into (2.65) yields

$$\frac{X(s)}{V(s)} = \frac{4Q_{eq}}{3\left(3\left(s^2 + 2\varsigma s + 1\right)\left(rs + \left(1 - X_{eq}\right)\right) - 2Q_{eq}^2\right)}. \tag{2.67}$$

Expanding the denominator of (2.67) yields

$$\frac{X(s)}{V(s)} = \frac{4Q_{eq}}{9\left(rs^3 + \left(1 - X_{eq} + 2\varsigma r\right)s^2 + \left(2\varsigma\left(1 - X_{eq}\right) + r\right)s + \left(1 - X_{eq} - \frac{2}{3}Q_{eq}^2\right)\right)}. \tag{2.68}$$

Equation (2.68) can be simplified further by utilizing the relationship between X_{eq} and Q_{eq} given in (2.44). The simplified (2.68) is given as follows.

$$\frac{X(s)}{V(s)} = \frac{4Q_{eq}}{9\left(rs^3 + \left(1 - X_{eq} + 2\varsigma r\right)s^2 + \left(2\varsigma\left(1 - X_{eq}\right) + r\right)s + \left(1 - 3X_{eq}\right)\right)} \tag{2.69}$$

When $X_{eq} = 1/3$, the transfer function of (2.69) will have a pole at the origin. So any operating point with a displacement greater than 1/3 will produce a pole in the right half plane. This shows explicitly how the transfer function becomes unstable at the pull-in displacement of 1/3.

2.5 Electrostatic Actuator Model Behavior

This section will study some special properties of the linearized model of the electrostatic actuator that can make feedback controller design very challenging. In addition, a transfer function representation of the linearized model will be chosen for use in controller design.

2.5.1 Pull-in Phenomenon and Noise Amplification of the Actuator

From (2.69), we can see that the magnitude of $\frac{X(j\omega)}{V(j\omega)}$ at $\omega = 0$ yields a steady state gain as shown in (2.70).

$$\left|\frac{X(j\omega)}{V(j\omega)}\right|_{\omega=0} = \frac{4Q_{eq}}{9(1-3X_{eq})} \tag{2.70}$$

Utilizing (2.44), we can rewrite the steady state gain (2.70) as a function of displacement in (2.71).

$$\left|\frac{X(j\omega)}{V(j\omega)}\right|_{\omega=0} = \frac{4\sqrt{3X_{eq}}}{9(1-3X_{eq})} \tag{2.71}$$

Equation (2.71) has a singularity at $X_{eq} = 1/3$. This singularity is referred to as pull-in. Figure 17 shows the steady state gain across the stable operating range of the electrostatic actuator.

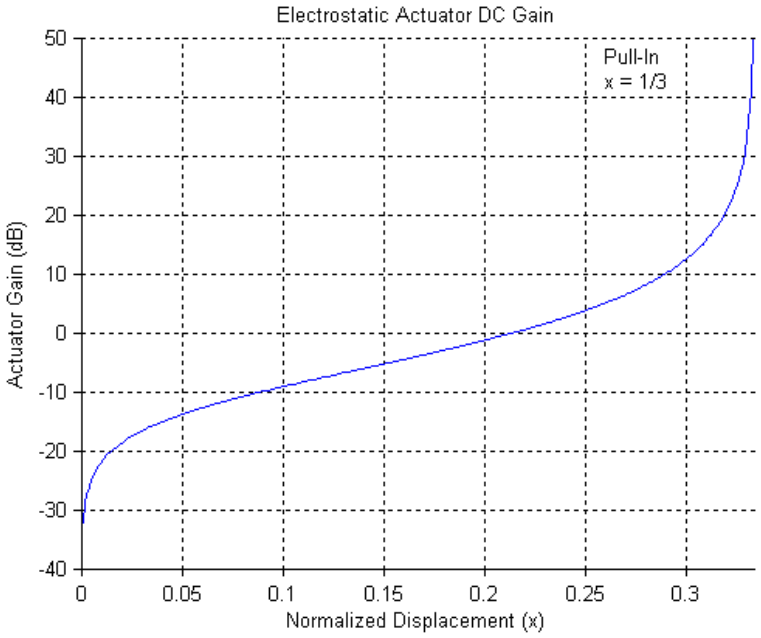

Figure 17: The Steady State Gain of the Electrostatic Actuator

From Figure 17, we can see that the steady state gain of the electrostatic actuator is a function of normalized displacement. The pull-in phenomenon occurs as the

actuator's displacement approaches 1/3 of the normalized displacement. One can also see from Figure 17 that at small displacements (less than 0.21 of the full gap) the electrostatic actuator attenuates the input commands. In Chapter 4 it will be shown that this low system gain also contributes to the amplification of sensor noise. In addition, unstable poles can also contribute to noise amplification. A bandwidth constraint must be satisfied in the presence of unstable poles, which will be described below.

The electrostatic actuator in the unstable regime can be described by the general transfer function of (2.72), where b_0, a_0, a_1, and a_2 are positive numbers.

$$P(s) = \frac{b_0}{(s+a_0)(s+a_1)(s-a_2)} \tag{2.72}$$

Equation (2.72) can be factored into a stable part and an unstable all-pass function as shown in (2.73).

$$P(s) = \underbrace{\frac{b_0}{(s+a_0)(s+a_1)(s+a_2)}}_{P_S}\underbrace{\frac{(s+a_2)}{(s-a_2)}}_{A} \tag{2.73}$$

In (2.73), $P_S(s)$ is the stable part, and $A(s)$ is the unstable part. The magnitude of A(s) is one for all frequencies (all pass function). The plant can now be written as

$$P(s) = P_S(s)A(s). \tag{2.74}$$

The phase contribution of A(s) is computed as

$$\angle A(j\omega) = -\pi + \tan^{-1}\left(\frac{\omega}{a_2}\right) - \tan^{-1}\left(-\frac{\omega}{a_2}\right). \tag{2.75}$$

Equation, (2.75) can be reduced to

$$\angle A(j\omega) = -\pi + 2\tan^{-1}\left(\frac{\omega}{a_2}\right). \tag{2.76}$$

The phase contribution from the all-pass transfer function *A(s)* starts with 180° of phase lag which decreases to 90° of lag at $\omega = a_2$. Table II shows how the phase lag, attributable to the unstable pole, is reduced by increasing the crossover frequency (bandwidth) of the system.

TABLE II: UNSTABLE POLE PHASE LAG

ω_{co}	a_2	$2a_2$	$3a_2$	$4a_2$
Phase Lag	-90.00	-53.13	-36.87	-28.07

Table II suggests that in order to stabilize a plant, a control system needs to be able to react sufficiently fast. This requires that the closed-loop bandwidth is larger than (approximately) $2a_2$ for a real RHP-pole a_2 [21].

In order to attenuate measurement noise the high frequency response needs to decrease as fast as possible while meeting the phase margin constraint. Phase-lag filters are utilized to accomplish this. This requires a certain amount of phase above the phase margin. An unstable pole, with its phase lag contribution limits the rate that the high frequency response can roll off.

In addition to the noise amplification problems there is also a concern for the magnitude of the control signal entering the plant. Any system with an unstable transfer function represented by *L(s)* is conditionally stable because the gain factor *K* of *L(s)* = *Kn(s)/d(s)*, where *n(s)* and *d(s)* are numerator and denominator of the transfer function

respectively, must be large enough to move the RHP poles of *L(s)* into the LHP [16]. This leads to the conclusion that for an unstable plant a minimum input usage *u* is required. In the case of the electrostatic actuator this will put a lower bound on the voltage that must be applied across the actuator.

2.5.2 Linear Models

According to [18], we use the following parameter values for the linearized model of the electrostatic actuator of (2.69).

$$\begin{aligned} \varsigma &= 2 \\ r &= 0.95 \end{aligned} \tag{2.77}$$

In order to determine the operating points, first a desired equilibrium displacement X_{eq} is chosen. With the chosen X_{eq}, (2.44) is used to compute the corresponding equilibrium charge Q_{eq}. Next, (2.45) can be utilized to solve for the equilibrium voltage V_{eq}. An alternative to directly using (2.45) is to substitute (2.44) into (2.45) which results in the equation for the equilibrium voltage given in (2.78).

$$V_{eq} = \frac{3}{2} Q_{eq} \left(1 - X_{eq}\right) \tag{2.78}$$

The equilibrium values of the displacement and charge (X_{eq} and Q_{eq}) corresponding to different percentages of the displacements with respect to full gap are calculated and given in Table III and Table IV.

TABLE III: EQUILIBRIUM POINTS PART I

X_{eq}	0.05	0.10	0.20	0.30	0.33	0.40
Q_{eq}	0.3873	0.5477	0.7746	0.9487	1.0000	1.0954
V_{eq}	0.5519	0.7394	0.9295	0.9961	1.0000	0.9859

TABLE IV: EQUILIBRIUM POINTS PART II

X_{eq}	0.50	0.60	0.70	0.80	0.90	0.95
Q_{eq}	1.2247	1.3416	1.4491	1.5492	1.6432	1.6882
V_{eq}	0.9185	0.8050	0.6521	0.4648	0.2465	0.1266

As stated before, the electrostatic actuator can be described by the generic plant given by (2.79).

$$P_{\%}(s) = \frac{b_0}{(s+a_0)(s+a_1)(s+a_2)} \tag{2.79}$$

In (2.79), the subscript % of $P_{\%}(s)$ represents the percentage of the displacement with respect to full gap. Utilizing (2.69), (2.78), and the equilibrium values of X_{eq} and Q_{eq} listed in Table III and Table IV, we can obtain the parameter values b_0, a_0, a_1, and a_2 for (2.79) as listed in Table V.

TABLE V: PLANT VARIATION

Plant	b_0	a_0	a_1	a_2	**DC Gain**
P_{05}	0.18119	3.721	1.050	0.2290	0.2025
P_{10}	0.25624	3.710	1.048	0.1895	0.3478
P_{20}	0.36238	3.689	1.044	0.1093	0.8609
P_{30}	0.44383	3.669	1.041	0.0276	4.2164
P_{33}	0.46784	3.662	1.104	0.0000	NA
P_{40}	0.51249	3.650	1.038	-0.0556	NA
P_{50}	0.57298	3.631	1.035	-0.1400	NA
P_{60}	0.62767	3.614	1.033	-0.2256	NA
P_{70}	0.67796	3.597	1.031	-0.3122	NA
P_{80}	0.72477	3.581	1.029	-0.3999	NA
P_{90}	0.76873	3.566	1.028	-0.4883	NA
P_{95}	0.7898	3.559	1.027	-0.5329	NA

It is clear from Table V that the plant has a varying plant gain (DC gain) along with a pole (a_2) that moves from the left-half plane into the right-half plane as the gap traversal moves beyond 1/3 of the initial gap. The other two poles (a_0 and a_1) do not introduce much variation.

2.6 Closed Loop Transfer Functions

Several closed-loop transfer functions will be used to demonstrate the effectiveness of the controller designs presented in this thesis. Figure 18 shows a general two-degree-of-freedom (2DOF) feedback control system.

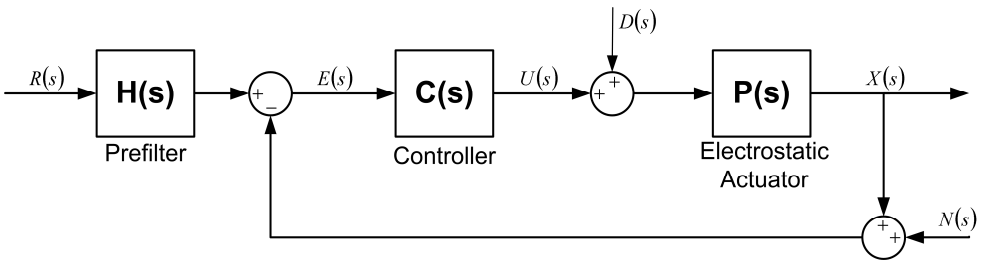

Figure 18: A General 2DOF Control System

In Figure 18, the electrostatic actuator is represented by plant $P(s)$, the controller is represented by $C(s)$ and the prefilter is represented by $H(s)$. There are three input signals: $R(s)$ is the reference signal, $D(s)$ is an input disturbance signal, and $N(s)$ is a sensor noise signal. There are also three output signals of interest: the measured output signal $X(s)$, the control signal $U(s)$, and the error signal $E(s)$. The outputs of the system are given by

$$X(s) = \frac{HPC}{1+PC} R(s) + \frac{P}{1+PC} D(s) - \frac{PC}{1+PC} N(s) \tag{2.80}$$

$$U(s) = \frac{CH}{1+PC} R(s) + \frac{PC}{1+PC} D(s) - \frac{C}{1+PC} N(s) \tag{2.81}$$

$$E(s) = \frac{H}{1+PC} R(s) - \frac{P}{1+PC} D(s) - \frac{1}{1+PC} N(s) \tag{2.82}$$

The loop transmission function $L(s)$ is a key component of these closed loop transfer functions and is defined in (2.83).

$$L(s) = P(s)C(s) \tag{2.83}$$

The sensitivity function $S(s)$ and the complementary sensitivity function $T(s)$ are shown in (2.84) and (2.85).

$$S(s) = \frac{1}{1 + L(s)} \tag{2.84}$$

$$T(s) = \frac{L(s)}{1 + L(s)} \tag{2.85}$$

Equation (2.86) shows the transfer function from the noise input $N(s)$ to the control signal $U(s)$ *(C(s)S(s))*. This transfer function will be used to investigate the amplification of sensor noise.

$$C(s)S(s) = \frac{C(s)}{1 + L(s)} \tag{2.86}$$

Equation (2.87) is the transfer function from the disturbance input $D(s)$ to the displacement $X(s)$ *(P(s)S(s))*. This transfer function will be used to gauge the disturbance rejection capabilities of the system.

$$P(s)S(s) = \frac{P(s)}{1 + L(s)} \tag{2.87}$$

Equation (2.88) shows the transfer function from the reference signal $R(s)$ to the displacement $X(s)$ *(H(s)T(s))*. This transfer function will be used to determine the step

response of the closed loop actuator system. All these transfer functions will be utilized extensively in Chapter 4.

$$H(s)T(s) = \frac{H(s)L(s)}{1+L(s)} \tag{2.88}$$

CHAPTER III

CONTROL TECHNIQUES

The first section in this chapter briefly discusses why feedback control can be beneficial for MEMS. The second section introduces the basic operating principles of a state space implementation of the ADRC. Then frequency-domain observers including classical Luenberger observers and extended-state observers will be developed. The chapter concludes with the derivation of the frequency-domain ADRC that will be used in the remaining part of this thesis.

3.1 Feedback Control for MEMS

Since the 1980's open-loop control schemes have dominated MEMS. This has led to much advancement in the design, fabrication and modeling of MEMS actuators. Open-loop control's main advantages are that it uses simpler driving electronics and it doesn't need sensing electronics. The importance of these two facts should not be underestimated. Real estate area on a silicon wafer is at a premium. In addition, the driving electronics and sensing electronics are at the same scale as the MEMS devices themselves. Incorporating them into the design will change the behavior of the MEMS device itself.

One of the key drawbacks of open-loop control is that it needs a fairly accurate model of the system in order to shape the inputs. This makes it susceptible to parameter variations. Another disadvantage is that it is not robust against un-measurable disturbances. Feedback control can provide several advantages over open-loop control. These advantages include the ability to:

1) Stabilize systems that are open-loop unstable.
2) Reduce the effects of un-measurable disturbances on the system response.
3) Reduce the effects of plant modeling errors and variations on the system response.

It should be noted that the use of feedback can also detract from these properties. Systems can be destabilized, and the effects of disturbances and plant uncertainty can be amplified. The use of feedback control also requires the use of sensors. The effect of plant disturbance cannot be attenuated without a measurement of its effect upon the

system output. There also exists a well-known tradeoff between the response of a feedback system to plant disturbances and to sensor noise. Even with these drawbacks, with the sophistication level of MEMS reaching an all time high, the use of feedback control will be inevitable if stringent performance requirements have to be met.

3.2 State Space Representation of ADRC

This section will briefly introduce ADRC design in its state space representation as a basis for the frequency domain derivation of the controller to be performed later in this chapter. ADRC was originally formulated as a nonlinear controller, thus using nonlinear gains. The nonlinear tuning parameters made control design difficult for all but the most experienced designers. ADRC was later simplified using linear and parameterized gains in [22]. It is often referred to as Linear ADRC (LADRC). The LADRC provided a more transparent tuning method that allowed the design and implementation of ADRC outside purely academic circles. ADRC was also formulated into a discrete-time version exhibited in [23]. Due to the nature of the design problems of the electrostatic actuator, a continuous-time ADRC is the focus of this thesis.

From (2.37) and (2.38), the nonlinear model of the electrostatic actuator can be represented by a third order model given in (3.1).

$$\dddot{y} = f\left(y, \dot{y}, \ddot{y}, d, t\right) + bu \tag{3.1}$$

In (3.1), y is the displacement output of the actuator, the function $f\left(y, \dot{y}, \ddot{y}, d, t\right)$, which will be taken as f in the following discussion, represents the internal plant dynamics and

an external unknown disturbance *d*. The function *f* is assumed to be unknown and is referred to as the generalized disturbance. The input to the plant is given by the control signal (*u*) and the plant gain (*b*).

ADRC estimates this generalized disturbance *f* and actively rejects the disturbance in real time. Eventually it reduces the electrostatic actuator model to a triple integrator plant with an input gain *b*. This reduced model is then controlled with a Proportional Derivative (PD) controller. An Extended State Observer (ESO) is utilized in the ADRC to estimate not only the disturbance but also the derivatives of the measured variable *y*. Figure 19 shows a general framework of the ADRC controller.

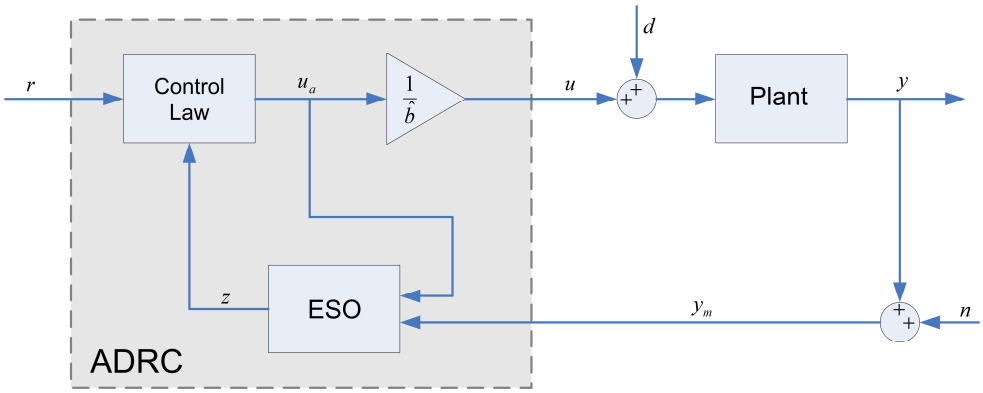

Figure 19: The Framework of ADRC

In Figure 19, the reference signal, *r*, along with the estimated states is fed into the yet undefined control law. The output of this control law u_a is fed back to the ESO along with the measured plant output y_m. The output of the control law is also scaled by $1/\hat{b}$ before being sent to the plant, where $\hat{b}$ is an estimate of *b*. The output of the ESO is the estimated state vector *z* which contains the estimated general disturbance along with the estimate of *y* and its derivatives.

In order to implement the ADRC in Figure 19, the nonlinear model of the electrostatic actuator in (3.1) is first converted to a state space representation with f included as an augmented state. The state variables are assigned as: $x_1 = y$, $x_2 = \dot{y}$, $x_3 = \ddot{y}$ and $x_4 = f$. Assuming $h = \dot{f}$ and h is bounded, the state space representation of (3.1) can be written as

$$\begin{cases} \dot{x}_1 = x_2 \\ \dot{x}_2 = x_3 \\ \dot{x}_3 = x_4 + bu \\ \dot{x}_4 = h(t) \\ y = x_1 \end{cases}. \tag{3.2}$$

Equation (3.2) can be rewritten as a matrix form:

$$\begin{aligned} \dot{x} &= Ax + Bu + Eh \\ y &= Cx \end{aligned}, \tag{3.3}$$

where

$$A = \begin{bmatrix} 0 & 1 & 0 & 0 \\ 0 & 0 & 1 & 0 \\ 0 & 0 & 0 & 1 \\ 0 & 0 & 0 & 0 \end{bmatrix},\ B = \begin{bmatrix} 0 \\ 0 \\ b \\ 0 \end{bmatrix},\ E = \begin{bmatrix} 0 \\ 0 \\ 0 \\ 1 \end{bmatrix}, \tag{3.4}$$

$$C = \begin{bmatrix} 1 & 0 & 0 & 0 \end{bmatrix}.$$

From [24], the augmented state $f\ (x_4)$ and the other states (x_1, x_2, and x_3) can be estimated using the ESO given as follows.

$$\begin{aligned} \dot{z} &= Az + Bu + L(y - \hat{y}) \\ \hat{y} &= Cz \end{aligned} \tag{3.5}$$

In (3.5), z is the estimated state vector and $z = \begin{bmatrix} z_1 & z_2 & z_3 & z_4 \end{bmatrix}^T$, where z_1, z_2, z_3, and z_4 are the estimated x_1, x_2, x_3,and x_4 respectively. The observer gain vector L is chosen so that all the observer poles are located at one location. As the observer gains are given by (3.6), the characteristic equation of the ESO will be $(s + \omega_o)^4$.

$$L = \begin{bmatrix} 4\omega_o & 6\omega_o^2 & 4\omega_o^3 & \omega_o^4 \end{bmatrix}^T \tag{3.6}$$

With a well tuned observer, the estimated states z_1, z_2, z_3, and z_4 will closely track y, $\dot{y}$, $\ddot{y}$ and f [22].

The control law of the ADRC is chosen as (3.7).

$$u = \frac{1}{\hat{b}}(u_0 - z_4) \tag{3.7}$$

Equation (3.7) reduces the original plant (3.1) to the desired triple integral plant as shown in (3.8).

$$\dddot{y} = u_0 \tag{3.8}$$

Equation (3.8) can be controlled by the control law in (3.9)

$$u_0 = k_p(r - z_1) - k_{d1}z_2 - k_{d2}z_3 - z_4 \tag{3.9}$$

In (3.9), the controller gains k_p, k_{d1}, k_{d2} are chosen to place all the closed loop poles of the controller at $-\omega_c$. Thus the values of the controller gains are given by (3.10).

$$\begin{aligned} k_p &= \omega_c^3 \\ k_{d1} &= 3\omega_c^2 \\ k_{d2} &= 3\omega_c \end{aligned} \tag{3.10}$$

Additional information about the ADRC can be found in [22-27]. The ADRC has been broadly used in macro systems [28-30]. It has also been applied to MEMS gyroscopes recently [31-32]. However, the ADRC has never been employed onto the MEMS electrostatic actuator before. The thesis research modified the controller and initially applied it onto the electrostatic actuators. The details about the application of the controller onto the actuator are given as follows.

3.3 Frequency Domain Observers

This section will look at the classic Luenberger observer and the ESO from a frequency domain perspective. The ESO, used in this thesis, utilizes a Luenberger observer with an augmented state for tracking disturbances. Comparing the differences between a classic Luenberger observer and the ESO will show the advantages of the ESO over the classic Luenberger observer.

3.3.1 Frequency Domain Observer Principles

The principle idea behind an observer is that by combining a measured feedback signal with a knowledge of the components of the control system, the behavior of the plant can be observed/estimated with greater precision than using the feedback signal alone [33]. This section will introduce several classic Luenberger observers represented by transfer function blocks. Figure 20 depicts an open-loop observer with an output error

(*e*) as the output. In this figure, *P* is the actual physical system (plant) under consideration, P_N is the nominal model (mathematical model) of the plant *P*, *y* is the output of the plant, $\hat{y}$ is the approximated output, and *u* is the control signal.

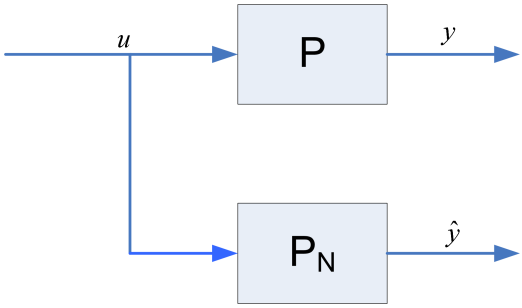

Figure 20: Open-loop Observer

From Figure 20, the actual output *y* and the approximated output $\hat{y}$ can be represented by the following equation.

$$\begin{aligned} y &= Pu \\ \hat{y} &= P_N u \end{aligned} \tag{3.11}$$

The difference between *y* and $\hat{y}$ can be used to construct an error signal (*e*). If the nominal model is fairly close to the actual model the error signal given by (3.12) will be very small. Then we can say that $\hat{y}$ is an observed/estimated *y*.

$$e = \left(P - P_N\right)u \tag{3.12}$$

The disadvantage of the open-loop observer shown in Figure 20 is that it is not robust against the initial conditions of the plant and system parameter variations. A compensator *C* can be added to drive this error *e* to zero by feeding back a correction signal u_e to the input of the nominal plant. This compensator *C* is internal to the

observer structure and is used to correct the output of the nominal plant instead of the real plant. This modified closed-loop observer is shown in Figure 21.

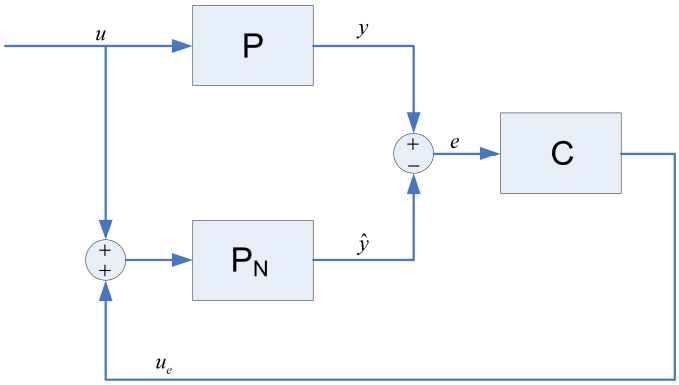

Figure 21: Closed-loop Observer

Figure 21 shows the following relations:

$$y = Pu, \quad \hat{y} = P_N(u + u_e), \quad u_e = C(y - \hat{y}). \tag{3.13}$$

Solving the equations of (3.13) for $\hat{y}$ gives (3.14).

$$(1 + P_N C)\hat{y} = P_N u + P_N C y \tag{3.14}$$

Equation (3.14) can be rewritten as

$$\hat{y} = \frac{P_N}{1 + P_N C} u + \frac{P_N C}{1 + P_N C} y. \tag{3.15}$$

The control signal u is defined in (3.16).

$$u = P^{-1} y \tag{3.16}$$

Substituting (3.16) into (3.15), we have (3.17).

$$\hat{y} = \frac{P_N}{1 + P_N C}(P^{-1} y) + \frac{P_N C}{1 + P_N C} y \tag{3.17}$$

When $P_N = P$, the estimated output $\hat{y}$ is approximately equal to *y* as shown in (3.18).

$$\hat{y} = \frac{1}{1+P_N C} y + \frac{P_N C}{1+P_N C} y = y \tag{3.18}$$

From (3.18), we can see that the estimate $\hat{y}$ tracks the real output *y* perfectly. Another interesting case is when $|C(j\omega)| >> 1$, the following derivation will be obtained.

$$\hat{y} \approx \frac{P_N C}{1+P_N C} y \approx \frac{P_N C}{P_N C} y \approx y \tag{3.19}$$

Equation (3.19) suggests that when the compensator gain is large, the estimate can track the actual value whether the nominal model is accurate or not. Conversely, when the magnitude of *C* is small, the estimated output is reduced to (3.20).

$$\hat{y} \approx \frac{P_N}{1+P_N C} u \approx P_N u \tag{3.20}$$

From (3.20), we can see that unless the nominal model is an accurate description of the plant, this estimate will be erroneous.

The observer analysis above is for an ideal system where sensor noise and disturbances were disregarded. Figure 22 shows the case where there is an input disturbance acting on the system.

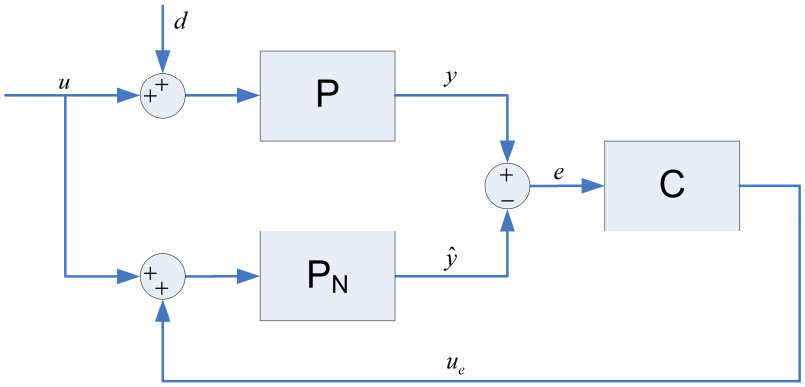

Figure 22: Closed-loop Observer with Disturbance

From Figure 22 the output signal is

$$y = P(u + d). \tag{3.21}$$

The estimated output is

$$\hat{y} = P_N(u + u_e). \tag{3.22}$$

The correction signal is

$$u_e = C(y - P_N(u + u_e)). \tag{3.23}$$

Equation (3.23) can be rewritten as

$$(1 + P_N C)u_e = Cy - P_N Cu\,. \tag{3.24}$$

From (3.24), we have

$$u_e = \frac{C}{1 + P_N C} y - \frac{P_N C}{1 + P_N C} u\,. \tag{3.25}$$

Note from (3.25) that when the magnitude of the compensator $|C(j\omega)| >> 1$, (3.25) is reduced to (3.26).

$$u_e \approx \frac{1}{P_N} y - u \tag{3.26}$$

Utilizing (3.21) and (3.26) gives

$$u_e \approx P_N^{-1}\left(P(u+d)\right) - u\,. \tag{3.27}$$

Equation (3.27) can be simplified to the form shown in (3.28).

$$u_e \approx P_N^{-1} P d + \left(P_N^{-1} P - 1\right) u \tag{3.28}$$

The difference between the actual system and the model is defined as $\Delta P = P - P_N$, substituting this relation into (3.28) gives

$$u_e \approx P_N^{-1}\left(P d + \Delta P u\right). \tag{3.29}$$

From (3.29) we can see that as the accuracy of the nominal model approaches that of the actual plant, $P_N^{-1} P \to 1$ and $\Delta P \to 0$. Then (3.29) reduces to $u_e \approx d$. If the nominal plant provides an accurate estimate of the physical system, u_e will act as an estimate of *d*.

Figure 23 shows the frequency-domain observer with sensor noise added at the plant output.

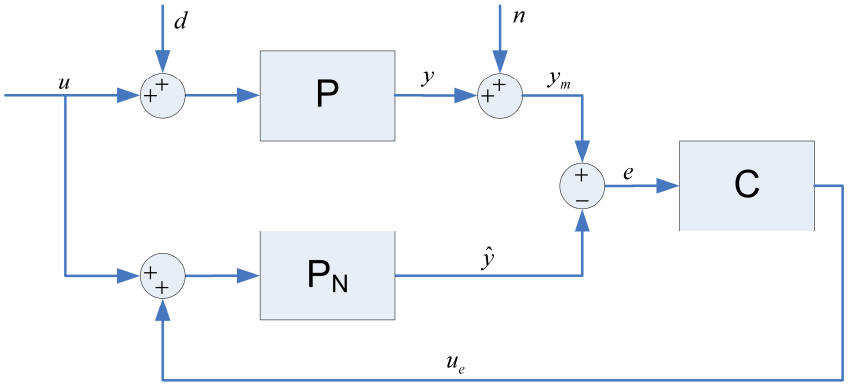

Figure 23: Closed-loop Observer with Sensor Noise

The equation that governs the frequency-domain observer when sensor noise is included is given in (3.30), where y_m is the noise corrupted output signal.

$$u_e = \frac{C}{1+P_N C} y_m - \frac{P_N C}{1+P_N C} u \tag{3.30}$$

Equation (3.30) can now be rewritten as

$$u_e = \frac{C}{1+P_N C}(y+n) - \frac{P_N C}{1+P_N C} u\,. \tag{3.31}$$

In the frequency range where $|C(j\omega)| >> 1$, (3.31) can be simplified as (3.32).

$$u_e \approx \frac{1}{P_N}(y+n) - u \tag{3.32}$$

Utilizing (3.32) and the same process that was used to derive (3.29), the final relation for the disturbance estimate can be obtained as

$$u_e \approx P_N^{-1}(Pd + \Delta P u + n). \tag{3.33}$$

From (3.33), it can be seen that as $|P_N(j\omega)| < 1$, the compensator u_e will magnify the sensor noise by the inverse of the nominal model.

The research findings of this section are summarized as follows. Equation (3.19) showed that when the compensator gain is large the estimated state tracks the actual state. From (3.20) we can see that when the compensator gain is small the estimated output will follow the nominal model. Equation (3.33) shows that when the model is accurate it will be possible to acquire an estimate of the disturbance *d*. We can also infer from (3.33) that the compensator can be considered as a combination of an external disturbance and

an internal disturbance (plant uncertainty). These two kinds of disturbances constituted the generalized disturbance that is the basis of the ADRC. The results of this section are dependent on the behavior of the observer's internal compensator *C*. In the sections that follow, the compensators for a Luenberger observer and an ESO will be derived in order to compare the compensators for the two designs.

3.3.2 Classic Luenberger Observer

In order to better understand the distinction between a classic Luenberger observer and an extended state observer, the structure of both observers will be compared. In this section a frequency domain description of a third order Luenberger observer will be derived. This observer structure will then be compared to the ESO in Section 3.3.3.

Suppose the plant under study is a third order integrator of the form in (3.34).

$$\dddot{y} = u \tag{3.34}$$

If *y* is the measured output, the following state variables will be defined.

$$\begin{aligned} x_1 &= y \\ x_2 &= \dot{y} \\ x_3 &= \ddot{y} \end{aligned} \tag{3.35}$$

The state space model of this plant (3.34) is given in (3.36).

$$\begin{bmatrix}\dot{x}_1\\ \dot{x}_2\\ \dot{x}_3\end{bmatrix}=\begin{bmatrix}0 & 1 & 0\\ 0 & 0 & 1\\ 0 & 0 & 0\end{bmatrix}\begin{bmatrix}x_1\\ x_2\\ x_3\end{bmatrix}+\begin{bmatrix}0\\ 0\\ 1\end{bmatrix}u$$
$$y=\begin{bmatrix}1 & 0 & 0\end{bmatrix}\begin{bmatrix}x_1\\ x_2\\ x_3\end{bmatrix} \tag{3.36}$$

The form of the Luenberger observer is given in (3.37), where z is the observed state vector and $z=\begin{bmatrix}z_1 & z_2 & z_3\end{bmatrix}^T$, and L is the observer gain vector.

$$\begin{aligned}\dot{z} &= Az + Bu + L(y-\hat{y})\\ \hat{y} &= Cz\end{aligned} \tag{3.37}$$

Equation (3.37) can be rewritten as in (3.38).

$$\begin{aligned}\dot{z} &= (A-LC)z + Bu + Ly\\ \hat{y} &= Cz\end{aligned} \tag{3.38}$$

In (3.38), the state matrices are represented as follows.

$$A=\begin{bmatrix}0 & 1 & 0\\ 0 & 0 & 1\\ 0 & 0 & 0\end{bmatrix}\quad B=\begin{bmatrix}0\\ 0\\ 1\end{bmatrix}\quad C=\begin{bmatrix}1 & 0 & 0\end{bmatrix}\quad L=\begin{bmatrix}L_1\\ L_2\\ L_3\end{bmatrix} \tag{3.39}$$

The Laplace transform of the observer (3.38) is given in (3.40).

$$sZ(s)=(A-LC)Z(s)+BU(s)+LY(s) \tag{3.40}$$

Equation (3.40) can be rewritten as

$$Z(s)=(sI-A+LC)^{-1}[BU(s)+LY(s)]. \tag{3.41}$$

In order to obtain $Z(s)$, the following matrix N must be computed.

$$N = \left(sI - A + LC\right) = \begin{bmatrix} s + L_1 & -1 & 0 \\ L_2 & s & -1 \\ L_3 & 0 & s \end{bmatrix} \tag{3.42}$$

The determinant of matrix N is

$$\det\left(N\right) = s^3 + L_1 s^2 + L_2 s + L_3 . \tag{3.43}$$

The inverse of (3.42) is

$$\left(sI - A + LC\right)^{-1} = \frac{1}{\det\left(N\right)} \begin{bmatrix} s^2 & s & 1 \\ -\left(L_2 s + L_3\right) & s\left(s + L_1\right) & s + L_1 \\ -L_3 s & -L_3 & s^2 + L_1 s + L_2 \end{bmatrix}. \tag{3.44}$$

Substituting (3.44) and (3.39) into (3.41), we will have (3.45).

$$\begin{bmatrix} Z_1(s) \\ Z_2(s) \\ Z_3(s) \end{bmatrix} = \frac{1}{\det\left(N\right)} \begin{bmatrix} s^2 & s & 1 \\ -\left(L_2 s + L_3\right) & s\left(s + L_1\right) & s + L_1 \\ -L_3 s & -L_3 & s^2 + L_1 s + L_2 \end{bmatrix} \begin{bmatrix} 0 \\ 0 \\ 1 \end{bmatrix} U(s) + \frac{1}{\det\left(N\right)} \begin{bmatrix} s^2 & s & 1 \\ -\left(L_2 s + L_3\right) & s\left(s + L_1\right) & s + L_1 \\ -L_3 s & -L_3 & s^2 + L_1 s + L_2 \end{bmatrix} \begin{bmatrix} L_1 \\ L_2 \\ L_3 \end{bmatrix} Y(s) \tag{3.45}$$

From (3.45), we will have the following three estimated states.

$$\begin{aligned} Z_1(s) &= \frac{1}{s^3 + L_1 s^2 + L_2 s + L_3} U(s) + \frac{L_1 s^2 + L_2 s + L_3}{s^3 + L_1 s^2 + L_2 s + L_3} Y(s) \\ Z_2(s) &= \frac{s + L_1}{s^3 + L_1 s^2 + L_2 s + L_3} U(s) + \frac{s\left(L_2 s + L_3\right)}{s^3 + L_1 s^2 + L_2 s + L_3} Y(s) \\ Z_3(s) &= \frac{s^2 + L_1 s + L_2}{s^3 + L_1 s^2 + L_2 s + L_3} U(s) + \frac{L_3 s^2}{s^3 + L_1 s^2 + L_2 s + L_3} Y(s) \end{aligned} \tag{3.46}$$

We assume that we use the closed-loop observer as shown in Figure 21. The estimated output given by (3.15) is repeated in (3.47).

$$\hat{y} = \frac{P_N}{1 + P_N C} u + \frac{P_N C}{1 + P_N C} y \tag{3.47}$$

Since the original system is a triple integrator (3.34), we can define the nominal plant as follows.

$$P_N = \frac{1}{s^3} \tag{3.48}$$

Substituting (3.48) ($P_N(s)$) into (3.47), and comparing (3.47) and the equations in (3.46), we will have the compensators for each state as shown in (3.49).

$$\begin{aligned} C_1(s) &= L_1 s^2 + L_2 s + L_3 \\ C_2(s) &= \frac{s(L_2 s + L_3)}{s + L_1} \\ C_3(s) &= \frac{L_3 s^2}{s^2 + L_1 s + L_2} \end{aligned} \tag{3.49}$$

In (3.49), $C_1(s)$ is an ideal second-order PD compensator for the estimate of $Z_1(s)$, $C_2(s)$ is a phase lead compensator for the estimate of $Z_2(s)$, and $C_3(s)$ is a phase lead compensator for the estimate of $Z_3(s)$.

Because the compensator $C_1(s)$ in (3.49) does not have an integral action, the estimation error for the $Z_1(s)$ will not be driven to zero at steady state. In Section 3.3.3 we will see how the addition of the augmented state of the ESO helps to alleviate this shortcoming.

3.3.3 Transfer Function Representation of a Fourth-order ESO

The ESO contains an augmented state to estimate the generalized disturbances to the system. For a third order integrating plant, as given in (3.34) one needs to design a fourth order ESO in order to reject disturbances. The Laplace transform of the equations that govern the fourth order ESO are given in (3.50).

The state space model for the extended state observer is as follows.

$$\begin{aligned} \dot{z} &= (A - LC)z + Bu_a + Ly \\ \hat{y} &= Cz \end{aligned} \tag{3.50}$$

The state matrices of (3.50) are given in (3.51).

$$A = \begin{bmatrix} 0 & 1 & 0 & 0 \\ 0 & 0 & 1 & 0 \\ 0 & 0 & 0 & 1 \\ 0 & 0 & 0 & 0 \end{bmatrix},\ B = \begin{bmatrix} 0 \\ 0 \\ 1 \\ 0 \end{bmatrix},\ L = \begin{bmatrix} L_1 \\ L_2 \\ L_3 \\ L_4 \end{bmatrix} \tag{3.51}$$

$$C = \begin{bmatrix} 1 & 0 & 0 & 0 \end{bmatrix}$$

Assuming zero initial conditions the Laplace transform of (3.50) is

$$Z(s) = (sI - A + LC)^{-1}[BU(s) + LY(s)], \tag{3.52}$$

where $Z(s) = [Z_1(s),\ Z_2(s),\ Z_3(s),\ Z_4(s)]^T$, and $Z_i(s)$ ($i \in [1 \quad 4]$) is an estimated state. Define N as

$$N = (sI - A + LC) = \begin{bmatrix} s + L_1 & -1 & 0 & 0 \\ L_2 & s & -1 & 0 \\ L_3 & 0 & s & -1 \\ L_4 & 0 & 0 & s \end{bmatrix}. \tag{3.53}$$

The determinant of N is

$$\det(N) = s^4 + L_1 s^3 + L_2 s^2 + L_3 s + L_4 \tag{3.54}$$

In order to simplify (3.52), we define the matrix M as

$$M = (sI - A + LC)^{-1}. \tag{3.55}$$

The matrix of (3.55) is

$$M = \frac{1}{s^4 + L_1 s^3 + L_2 s^2 + L_3 s + L_4} \begin{bmatrix} M_1 \\ M_2 \\ M_3 \\ M_4 \end{bmatrix}. \tag{3.56}$$

In (3.56), the row vectors M_1, M_2, M_3, and M_4 are defined as follows.

$$\begin{aligned} M_1 &= \begin{bmatrix} s^3 & s^2 & s & 1 \end{bmatrix} \\ M_2 &= \begin{bmatrix} -(L_2 s^2 + L_3 s + L_4) & s^2(s + L_1) & s(s + L_1) & s + L_1 \end{bmatrix} \\ M_3 &= \begin{bmatrix} -s(L_3 s + L_4) & -(L_3 s + L_4) & s(s^2 + L_1 s + L_2) & s^2 + L_1 s + L_2 \end{bmatrix} \\ M_4 &= \begin{bmatrix} -L_4 s^2 & -L_4 s & -L_4 & s^3 + L_1 s^2 + L_2 s + L_3 \end{bmatrix} \end{aligned} \tag{3.57}$$

Each estimated state can be computed by the following equation.

$$\begin{aligned} Z_i(s) = &\frac{M_i L}{s^4 + L_1 s^3 + L_2 s^2 + L_3 s + L_4} Y(s) + \\ &\frac{M_i B}{s^4 + L_1 s^3 + L_2 s^2 + L_3 s + L_4} U(s) \end{aligned} \tag{3.58}$$

Using (3.51), (3.57), and (3.58) the estimated output $Z_1(s)$ is computed as

$$\begin{aligned} Z_1(s) = &\frac{(L_1 s^3 + L_2 s^2 + L_3 s + L_4)}{s^4 + L_1 s^3 + L_2 s^2 + L_3 s + L_4} Y(s) + \\ &\frac{s}{s^4 + L_1 s^3 + L_2 s^2 + L_3 s + L_4} U(s) \end{aligned}. \tag{3.59}$$

Recalling (3.47), the transfer function for the state observer is given by (3.60).

$$Z_i(s) = \frac{P_N C_i}{1 + P_N C_i} Y(s) + \frac{P_N}{1 + P_N C_i} U(s) \tag{3.60}$$

Solving (3.60) for the compensator $C_1(s)$ results in (3.61).

$$C_1(s) = L_1 s^2 + L_2 s + L_3 + L_4 \frac{1}{s} \tag{3.61}$$

This compensator in (3.61) clearly has an integral action. The nominal plant is

$$P_N(s) = \frac{1}{s^3}. \tag{3.62}$$

Next, one can use (3.58) to solve for $Z_2(s)$, as given in (3.63).

$$\begin{aligned} Z_2(s) = & \frac{s\left(L_2 s^2 + L_3 s + L_4\right)}{s^4 + L_1 s^3 + L_2 s^2 + L_3 s + L_4} Y(s) + \\ & \frac{s\left(s + L_1\right)}{s^4 + L_1 s^3 + L_2 s^2 + L_3 s + L_4} U(s) \end{aligned} \tag{3.63}$$

Solving for the compensator $C_2(s)$ gives (3.64).

$$C_2(s) = \frac{L_2 s^2 + L_3 s + L_4}{s + L_1} \tag{3.64}$$

The nominal plant is the same as the one given in (3.62). Solving (3.58) for $Z_3(s)$, we will obtain (3.65).

$$\begin{aligned} Z_3(s) = & \frac{s^2\left(L_3 s + L_4\right)}{s^4 + L_1 s^3 + L_2 s^2 + L_3 s + L_4} Y(s) + \\ & \frac{s\left(s^2 + L_1 s + L_2\right)}{s^4 + L_1 s^3 + L_2 s^2 + L_3 s + L_4} U(s) \end{aligned} \tag{3.65}$$

Solving for the compensator $C_3(s)$ yields (3.66).

$$C_3(s) = \frac{s(L_3 s + L_4)}{s^2 + L_1 s + L_2} \tag{3.66}$$

Then the estimate of the augmented state is

$$Z_4(s) = \frac{L_4 s^3}{s^4 + L_1 s^3 + L_2 s^2 + L_3 s + L_4} Y(s) - \frac{L_4}{s^4 + L_1 s^3 + L_2 s^2 + L_3 s + L_4} U(s) \tag{3.67}$$

Equation (3.67) can be rewritten as

$$Z_4(s) = \frac{L_4}{s^4 + L_1 s^3 + L_2 s^2 + L_3 s + L_4} \left[s^3 Y(s) - U(s) \right]. \tag{3.68}$$

It is shown in [34] that (3.68) can be viewed as a low-pass-filtered (LPF) disturbance estimate. Then (3.68) can be also expressed as

$$Z_4(s) = LPF\left[P_N^{-1} Y(s) - U(s) \right]. \tag{3.69}$$

Comparing (3.61) to (3.49), we can see that the use of the augmented state in the ESO allows the estimated output $Z_1(s)$ to track the plant output with zero steady state error. This gives the ESO a significant advantage in rejecting constant disturbances (internal and external) to the system.

3.4 Transfer Function Description of ADRC

In this section, a frequency-domain implementation of the ADRC will be derived for a third order plant. The derivation of a transfer function description of the ADRC for a second order plant was reported in [24]. The third-order electrostatic model requires a 4th order ESO and a second order controller. Figure 24 shows the essential components in an ADRC.

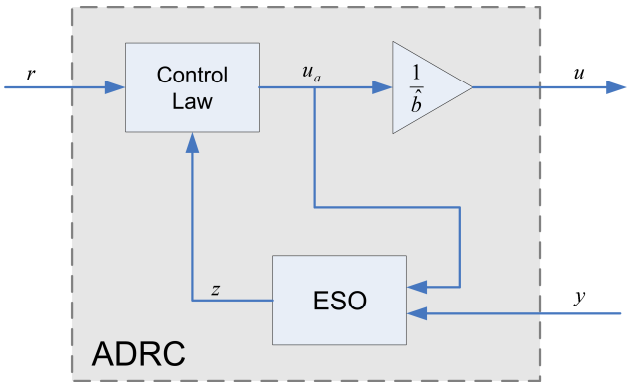

Figure 24: ADRC Topology

The state equations for the fourth-order extended state observer are given in (3.70).

$$\begin{aligned} \dot{z} &= (A - LC)z + Bu + Ly \\ \hat{y} &= Cz \end{aligned} \tag{3.70}$$

The state matrices of (3.70) are represented by (3.71).

$$A = \begin{bmatrix} 0 & 1 & 0 & 0 \\ 0 & 0 & 1 & 0 \\ 0 & 0 & 0 & 1 \\ 0 & 0 & 0 & 0 \end{bmatrix}, \; B = \begin{bmatrix} 0 \\ 0 \\ \hat{b} \\ 0 \end{bmatrix}, \; L = \begin{bmatrix} L_1 \\ L_2 \\ L_3 \\ L_4 \end{bmatrix} \tag{3.71}$$

$$C = \begin{bmatrix} 1 & 0 & 0 & 0 \end{bmatrix}$$

Assuming zero initial conditions for $z(t)$, we will have the Laplace transform of (3.70):

$$Z(s) = (sI - A + LC)^{-1}[BU(s) + LY(s)]. \tag{3.72}$$

From Figure 24, the control input *u* to the plant is given by (3.73).

$$u = \frac{1}{\hat{b}} u_a \tag{3.73}$$

In (3.73), the control law (u_a) is

$$u_a = k_p(r - z_1) - k_{d1} z_2 - k_{d2} z_3 - z_4. \tag{3.74}$$

Substituting (3.74) into (3.73), we have

$$u = \frac{1}{\hat{b}}\left(k_p r - \begin{bmatrix} k_p & k_{d1} & k_{d2} & 1 \end{bmatrix} z\right). \tag{3.75}$$

The controller gain vector *K* is defined in (3.76).

$$K = \begin{bmatrix} k_p & k_{d1} & k_{d2} & 1 \end{bmatrix} \tag{3.76}$$

Substituting (3.76) into (3.75), we will have the Laplace transform of (3.75) as given in (3.77).

$$U(s) = \frac{1}{\hat{b}}\left(k_p R(s) - KZ(s)\right) \tag{3.77}$$

Substituting (3.72) into (3.77), we have

$$U(s) = \frac{1}{\hat{b}}\left[k_p R(s) - K(sI - A + LC)^{-1}(BU(s) + LY(s))\right]. \tag{3.78}$$

In order to simplify (3.78), we define the matrix *M* as

$$M = (sI - A + LC)^{-1}. \tag{3.79}$$

Substituting (3.79) into (3.78) and simplifying the results, we have

$$\left(\hat{b} + KMB\right)U(s) = k_p R(s) - KMLY(s). \tag{3.80}$$

Equation (3.80) can be rewritten as

$$U(s) = \left[\frac{k_p}{\hat{b} + KMB} R(s) - \frac{KML}{\hat{b} + KMB} Y(s)\right]. \tag{3.81}$$

The transfer function (3.81) of the ADRC can be derived in the form of a two Degree-Of-Freedom (2-DOF) closed loop system as shown in Figure 25.

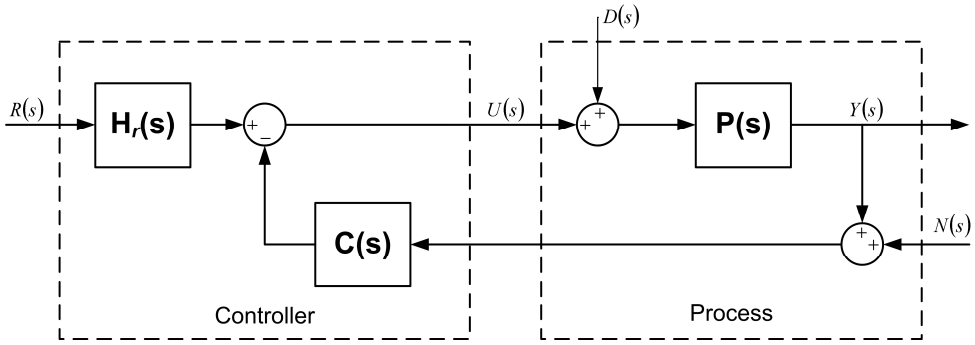

Figure 25: Block Diagram of the Closed-loop ADRC-controlled System with the Controller in a Feedback Path

In Figure 25, $H_r(s)$ is a prefilter, $C(s)$ is the controller in a feedback (return) path and $P(s)$ is the plant to be controlled. The prefilter and controller are presented in (3.82).

$$C(s) = \frac{KML}{\hat{b} + KMB} \quad H_r(s) = \frac{k_p}{\hat{b} + KMB} \tag{3.82}$$

The vector *K* in (3.76) can be defined as

$$K = \begin{bmatrix} k_p & k_{d1} & k_{d2} & 1 \end{bmatrix} = \begin{bmatrix} K_1 & K_2 & K_3 & 1 \end{bmatrix}. \tag{3.83}$$

Using, (3.83), the polynomial *KMB* in (3.82) was derived as (3.84).

$$KMB = \frac{\hat{b}\left(K_3 s^3 + (K_2 + K_3 L_1)s^2 + (K_1 + K_2 L_1 + K_3 L_2)s - L_4\right)}{s^4 + L_1 s^3 + L_2 s^2 + L_3 s + L_4} \tag{3.84}$$

The transfer function $\hat{b} + KMB$ is

$$\hat{b} + KMB = \frac{\hat{b}s\left(s^3 + N_1 s^2 + N_2 s + N_3\right)}{s^4 + L_1 s^3 + L_2 s^2 + L_3 s + L_4}, \tag{3.85}$$

where the coefficients of the numerator of (3.85) are

$$\begin{aligned} N_1 &= K_3 + L_1 \\ N_2 &= K_2 + L_2 + K_3 L_1 \\ N_3 &= K_1 + K_2 L_1 + K_3 L_2 + L_3 \end{aligned} . \tag{3.86}$$

The *KML* polynomial in (3.82) is

$$KML = \frac{F_1 s^3 + F_2 s^2 + F_3 s + F_4}{s^4 + L_1 s^3 + L_2 s^2 + L_3 s + L_4}, \tag{3.87}$$

where the numerator coefficients for (3.87) are

$$\begin{aligned} F_1 &= K_1 L_1 + K_2 L_2 + K_3 L_3 + L_4 \\ F_2 &= K_1 L_2 + K_2 L_3 + K_3 L_4 \\ F_3 &= K_1 L_3 + K_2 L_4 \\ F_4 &= K_1 L_4 \end{aligned} . \tag{3.88}$$

Recalling the format of the feedback controller in (3.82) gives (3.89).

$$C(s) = \frac{KML}{\hat{b} + KMB} \tag{3.89}$$

Substituting (3.85) and (3.87) into (3.89), we will have the controller shown as follows.

$$C(s) = \frac{1}{\hat{b}} \cdot \frac{N_{C1}s^3 + N_{C2}s^2 + N_{C3}s + N_{C4}}{s\left(s^3 + D_{C1}s^2 + D_{C2}s + D_{C3}\right)} \tag{3.90}$$

The numerator coefficients of (3.90) are found in (3.91).

$$\begin{aligned} N_{C1} &= K_1L_1 + K_2L_2 + K_3L_3 + L_4 \\ N_{C2} &= K_1L_2 + K_2L_3 + K_3L_4 \\ N_{C3} &= K_1L_3 + K_2L_4 \\ N_{C4} &= K_1L_4 \end{aligned} \tag{3.91}$$

The denominator coefficients of (3.90) are given in (3.92)

$$\begin{aligned} D_{C1} &= K_3 + L_1 \\ D_{C2} &= K_2 + L_2 + K_3L_1 \\ D_{C3} &= K_1 + K_2L_1 + K_3L_2 + L_3 \end{aligned} \tag{3.92}$$

The next step is to compute the prefilter. The prefilter is described by (3.93).

$$H_r(s) = \frac{k_p}{\hat{b} + KMB} = \frac{K_1}{\hat{b} + KMB} \tag{3.93}$$

Substituting (3.85) into (3.93), we have

$$H_r(s) = \frac{1}{\hat{b}} \cdot \frac{K_1\left(s^4 + L_1s^3 + L_2s^2 + L_3s + L_4\right)}{s\left(s^3 + D_{C1}s^2 + D_{C2}s + D_{C3}\right)}. \tag{3.94}$$

The denominator coefficients of (3.94) are given in (3.92). Both the controller (3.90) and the prefilter (3.94) have the same poles.

Next, the controller and prefilter will be derived for the controller in a feed-forward path as seen in Figure 26.

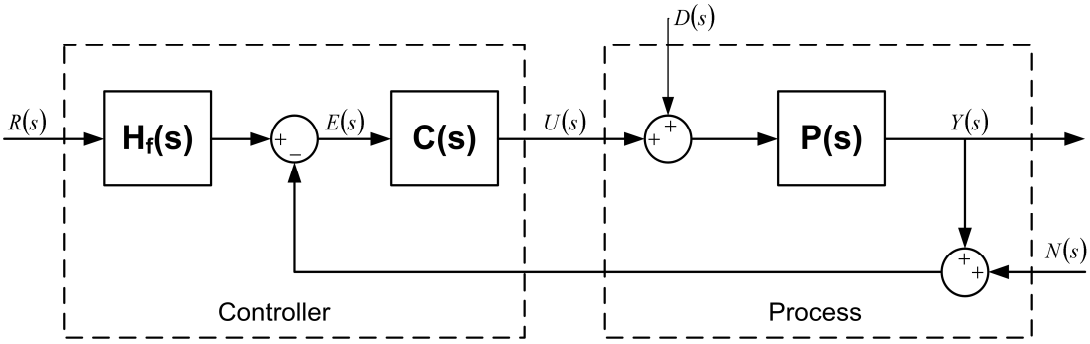

Figure 26: Block Diagram of the Closed-loop ADRC-controlled System with the Controller in a Feed-forward Path

In Figure 26, $H_f(s)$ is the prefilter, $C(s)$ is the controller in a forward path and $P(s)$ is the plant to be controlled. The control signal in Figure 26 is given in (3.95).

$$U(s) = C(s)E(s) \tag{3.95}$$

In (3.95), the error signal *E(s)* is found in (3.96).

$$E(s) = H_f(s)R(s) - Y(s) \tag{3.96}$$

Replacing the $E(s)$ in (3.95) with (3.96) we have

$$U(s) = C(s)\left[H_f(s)R(s) - Y(s)\right]. \tag{3.97}$$

Equation (3.81) shows the control signal for the ADRC as follows.

$$U(s) = \underbrace{\frac{k_p}{\hat{b} + KMB}}_{C(s)H_f(s)} R(s) - \underbrace{\frac{KML}{\hat{b} + KMB}}_{C(s)} Y(s) \tag{3.98}$$

Comparing (3.98) with (3.97), we have

$$C(s) = \frac{KML}{\hat{b} + KMB}. \tag{3.99}$$

We can see that the controller (3.99) in the forward path is the same as the one (3.89) in the feedback path. The prefilter is the only transfer function that has changed. Comparing (3.97) to (3.98), we have

$$C(s)H_f(s) = \frac{K_1}{\hat{b} + KMB}. \tag{3.100}$$

From (3.99) and (3.100), one can solve for $H_f(s)$ as given in (3.101).

$$H_f(s) = \frac{K_1}{\hat{b} + KMB} C^{-1}(s) \tag{3.101}$$

Substituting the inverse of the controller of (3.99) into (3.101) gives the transfer function for the prefilter.

$$H_f(s) = \left(\frac{K_1}{\hat{b} + KMB} \right) \left(\frac{\hat{b} + KMB}{KML} \right) = \frac{K_1}{KML} \tag{3.102}$$

Therefore as the controller $C(s)$ is placed into the feed-forward path as shown in Figure 26, we will have the transfer functions for the controller and the prefilter as given by (3.103) and (3.104) respectively.

$$C(s) = \frac{KML}{\hat{b} + KMB} \tag{3.103}$$

$$H_f(s) = \frac{K_1}{KML} \tag{3.104}$$

Replacing the *KML* in (3.104) with (3.87), we have the prefilter given as follows.

$$H_f(s) = \frac{K_1 \left(s^4 + L_1 s^3 + L_2 s^2 + L_3 s + L_4 \right)}{D_{H1} s^3 + D_{H2} s^2 + D_{H3} s + D_{H4}} \tag{3.105}$$

The denominator coefficients of (3.105) are given in (3.106).

$$\begin{aligned} D_{H1} &= K_1 L_1 + K_2 L_2 + K_3 L_3 + L_4 \\ D_{H2} &= K_1 L_2 + K_2 L_3 + K_3 L_4 \\ D_{H3} &= K_1 L_3 + K_2 L_4 \\ D_{H4} &= K_1 L_4 \end{aligned} \tag{3.106}$$

From the equation developments above, we can see that the transfer function of the controller in the forward path is identical to the feedback controller. However, the prefilters are different for the two cases. Next we will substitute the values of the controller and observer gains into the equations derived based on Figure 25 and Figure 26 to obtain the final representations of the controller and the corresponding prefilters.

The observer gain vector in (3.6) is repeated in (3.107).

$$L = \begin{bmatrix} L_1 & L_2 & L_3 & L_4 \end{bmatrix} = \begin{bmatrix} 4\omega_o & 6\omega_o^2 & 4\omega_o^3 & \omega_o^4 \end{bmatrix} \tag{3.107}$$

The controller gain vector in (3.10) is repeated in (3.108).

$$K = \begin{bmatrix} K_1 & K_2 & K_3 & 1 \end{bmatrix} = \begin{bmatrix} \omega_c^3 & 3\omega_c^2 & 3\omega_c & 1 \end{bmatrix} \tag{3.108}$$

Substituting (3.107) and (3.108) into (3.103), we have the controller:

$$C(s) = \frac{1}{\hat{b}} \cdot \frac{N_{C1} s^3 + N_{C2} s^2 + N_{C3} s + N_{C4}}{s\left(s^3 + D_{C1} s^2 + D_{C2} s + D_{C3}\right)}, \tag{3.109}$$

where the numerator coefficients for the controller in (3.109) are:

$$\begin{aligned} N_{C1} &= 4\omega_c^3 \omega_o + 18\omega_c \omega_o^2 + 12\omega_c \omega_o^3 + \omega_o^4 \\ N_{C2} &= 6\omega_c^3 \omega_o^2 + 12\omega_c^2 \omega_o^3 + 3\omega_c \omega_o^4 \\ N_{C3} &= 4\omega_c^3 \omega_o^3 + 3\omega_c \omega_o^4 \\ N_{C4} &= \omega_c^3 \omega_o^4 \end{aligned}, \tag{3.110}$$

and the denominator coefficients of (3.109) are:

$$\begin{aligned} D_{C1} &= 3\omega_c + 4\omega_o \\ D_{C2} &= 3\omega_c^2 + 12\omega_c\omega_o + 6\omega_o^2 \\ D_{C3} &= \omega_c^3 + 12\omega_c^2\omega_o + 18\omega_c\omega_o^2 + 4\omega_o^3 \end{aligned} \quad . \tag{3.111}$$

Substituting (3.107) and (3.108) into (3.94), we have the prefilter in Figure 25:

$$H_r(s) = \frac{1}{\hat{b}} \cdot \frac{\omega_c^3\left(s^4 + 4\omega_o s^3 + 6\omega_o^2 s^2 + 4\omega_o^3 s + \omega_o^4\right)}{s\left(s^3 + D_{C1}s^2 + D_{C2}s + D_{C3}\right)}. \tag{3.112}$$

The denominator coefficients of (3.112) are given in (3.111).

Substituting (3.107) and (3.108) into (3.104), we have the prefilter in Figure 26:

$$H_f(s) = \frac{\omega_c^3\left(s^4 + 4\omega_o s^3 + 6\omega_o^2 s^2 + 4\omega_o^3 s + \omega_o^4\right)}{D_{H1}s^3 + D_{H2}s^2 + D_{H3}s + D_{H4}}. \tag{3.113}$$

The denominator coefficients of the prefilter in (3.113) are given in (3.114)

$$\begin{aligned} D_{H1} &= 4\omega_c^3\omega_o + 18\omega_c^2\omega_o^2 + 12\omega_c\omega_o^3 + \omega_o^4 \\ D_{H2} &= 3\omega_c\omega_o^4 + 12\omega_c^2\omega_o^3 + 6\omega_c^3\omega_o^2 \\ D_{H3} &= 3\omega_c^2\omega_o^4 + 4\omega_c^3\omega_o^3 \\ D_{H4} &= \omega_c^3\omega_o^4 \end{aligned} \tag{3.114}$$

Looking at the two control structures in Figure 25 and Figure 26, we can see that the ADRC used in this design is a 2-DOF controller. The problem of 1-DOF controllers is that there is always a tradeoff between command following and disturbance rejection. The use of a 2-DOF controller solved this problem by allowing the reference signal *r* and the output measurement *y* to be treated independently by the controller, rather than by operating on their difference *y-r* as in a 1-DOF controller.

The choice between the topologies shown in Figure 25 and Figure 26 comes down to the prefilter. The prefilter in Figure 26 can not be implemented in Simulink while the prefilter in Figure 25 is appropriate for the simulations in Simulink®. Therefore, we will choose the control system shown in Figure 25 in our simulations. In addition, the control system represented by Figure 25 allows for the derivations of traditionally defined sensitivity function (S), complementary sensitivity function (T), and other various closed loop transfer functions that were used for controller design in Chapter IV.

CHAPTER IV

CONTROLLER DESIGNS AND PERFORMANCE ANALYSES

This chapter introduces the design strategies of three linear controllers for the linearized electrostatic actuator. Our control goal is to extend the travel range of the movable plate of the actuator to a desired value in the presence of the pull-in limit. The first design strategy assumes all the states and the generalized disturbance of the actuator are unknown, and utilizes a fourth-order ESO to observe both the system states and the generalized disturbance of the actuator. Based on accurate estimations of the ESO, a classic LADRC will reduce the original system model of the actuator to a third-order integrator and control the reduced model in real time. The second design strategy utilizes partially known modeling information of the actuator to design the ADRC where the ESO is only used to observe unknown states and the generalized disturbance. The third design strategy divides the original system model of the actuator into electrical and mechanical parts. A multi-loop control, consisting of a standard ADRC for an inner loop and a PI controller as an outer loop, is employed to control the charge output for the electrical part in the inner loop and the displacement output for the mechanical part in the outer loop respectively. All of the three design strategies take into consideration the effects of noise, and attenuate the noise effects using the controllers.

4.1 Classic LADRC Design

4.1.1 Controller Framework

In the frequency domain, the loop transmission function is a key tool in accessing the performance of a control system. The loop transmission function is derived from Figure 25 and is defined in (4.1), in which $P(s)$ is the plant to be controlled and $C(s)$ is the feedback controller.

$$L(s) = P(s)C(s) \tag{4.1}$$

From (2.69) the electrostatic actuator can be described by a third-order plant in the form of (4.2), in which b_0 is a constant numerator coefficient, and a_0, a_1, and a_2 are positive constants.

$$P(s) = \frac{b_o}{(s+a_0)(s+a_1)(s+a_2)} \tag{4.2}$$

As the ADRC is placed in the feedback path of the closed-loop control system for the actuator as shown in Figure 25, (4.3) gives the transfer function representation of the ADRC. Comparing (4.3) to (3.73), we have $c_0 = N_{C1}$, $c_1 = N_{C2}$, $c_2 = N_{C3}$, $c_3 = N_{C4}$, $d_0 = D_{C1}$, $d_1 = D_{C2}$, and $d_2 = D_{C3}$.

$$C(s) = \frac{1}{\hat{b}_0} \cdot \frac{c_0 s^3 + c_1 s^2 + c_2 s + c_3}{s\left(s^3 + d_0 s^2 + d_1 s + d_2\right)} \tag{4.3}$$

Substituting the plant of (4.2) and the controller of (4.3) into (4.1) yields the general loop transmission function $L(s)$ of (4.4).

$$L(s) = P(s)C(s) = \frac{b_o}{\hat{b}_0} \cdot \frac{c_0 s^3 + c_1 s^2 + c_2 s + c_3}{s(s+a_0)(s+a_1)(s+a_2)(s^3 + d_0 s^2 + d_1 s + d_2)} \quad (4.4)$$

Equation (4.4) will be used to investigate stability and robustness of the closed-loop system.

The control goal is to make the displacement output of the movable plate of the actuator track a desired reference position. As analyzed at the end of Chapter 3, the controller is placed in the feedback path, as shown in Figure 25, as the final framework of the ADRC control system. Thus from (3.94), the prefilter will be

$$H_r(s) = \frac{1}{\hat{b}_0} \cdot \frac{K_1(s^4 + L_1 s^3 + L_2 s^2 + L_3 s + L_4)}{s(s^3 + d_0 s^2 + d_1 s + d_2)}. \quad (4.5)$$

The poles of the controller (4.3) and the prefilter are the same in this configuration.

4.1.2 Classic ADRC Design

One of the main advantages of the ADRC is that it has few tuning parameters. The controller can be tuned utilizing three parameters. These parameters are the controller bandwidth ω_c, the observer bandwidth ω_o and the approximate input gain of the plant $\hat{b}_0$.

In this section, the ADRC with three different sets of tuning parameters will be discussed. The values of the three sets of tuning parameters for the ADRC are given in

Table VI, in which the ADRC with the first set of tuning parameters is taken as design one, the ADRC with the second set of tuning parameters is taken as design two, and the ADRC with the third set of tuning parameters is taken as design three.

TABLE VI: THREE SETS OF TUNING PARAMETERS

Design	$\hat{b}_0$	$\omega_c \ (rad/s)$	$\omega_o \ (rad/s)$
1	1.1	2	50
2	0.78	2	30
3	0.65	2	20

There was a preliminary tuning process performed to choose the parameter values listed in Table VI. The choice of the controller bandwidth ω_c was chosen based on the desired transient response of the system. The observer bandwidth ω_o is constrained by the amplification of sensor noise. The general rule of thumb is to select ω_o to be three to five times the bandwidth of ω_c [22]. The observer bandwidth should be chosen as large as the sensor noise will allow. The approximation of the input gain $\hat{b}$ was used to fine tune the frequency response of the loop transmission function (4.1) to maximize the stability margins of the system. From Table VI, we can see that the controller bandwidth is chosen fixed ($\omega_c = 2\, rad/s$) since this value gave the best compromise between performance and noise attenuation for the actuator. The details about the tuning process of the ADRC can be found in [22].

If we assume the ESO has accurately estimated the generalized disturbance, with the controller bandwidth set at 2 *rad / s*, the desired closed-loop transfer function P_{des} of the system shown in Figure 25 will be given by (4.6).

$$P_{des} = \frac{\omega_c^3}{s^3 + 3\omega_c s^2 + 3\omega_c^2 s + \omega_c^3} = \frac{8}{s^3 + 6s^2 + 12s + 8} = \frac{8}{(s+2)^3} \tag{4.6}$$

The step response of this desired plant is shown in Figure 27, where the magnitude of the reference signal is 1.

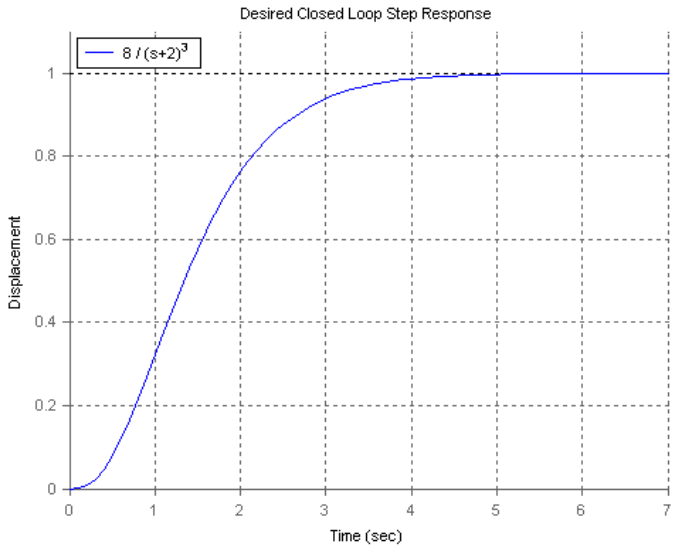

Figure 27: Desired Closed Loop Response to a Step Reference Signal

From Figure 27 we can see that the desired response has a rise time of about 2.66 seconds and has a settling time of 3.76 seconds. The performance of this desired response is comparable to the nonlinear controllers designed in [18-20].

4.1.2.1 Design 1

From Table VI, the controller parameter values of the first design are: $\omega_c = 2$, $\omega_o = 50$, $\hat{b} = 1.1$, in which the observer bandwidth is a rather high parameter. The controller for this design is based on (3.90) (associated with (3.91), (3.92), (3.107), and (3.108)) and is given in (4.7).

$$C(s) = \frac{8{,}574{,}182(s+1.322)(s^2+3.303s+4.009)}{s(s+105.6)(s^2+100.4s+5610)} \tag{4.7}$$

The prefilter that is used in this design for command following is based on (3.94) (associated with (3.92), (3.107) and (3.108)) and is given in (4.8)

$$H_r(s) = \frac{7.3(s+50)^4}{s(s+105.6)(s^2+100.4s+5610)} \tag{4.8}$$

The controller is tested on the electrostatic actuator model represented by (4.2). The values of the system parameters corresponding to different desired travel ranges (or displacements) of the moveable plate of the actuator can be found in Table V in Chapter 2. In the following analysis for the first design, we choose the desired displacements as 5%, 20% 33%, 50%, 75% and 95% of the full gap. Figure 28 shows Bode diagrams of the loop transmission function $L(j\omega)$ given by (4.4) for these different travel ranges. In Figure 28, *L05* represents the loop transmission function (4.4) for the desired travel range being 5% of the full gap. The plant for this travel range is denoted by *P05*. Similarly, *L20*, *L33*, *L50*, *L75*, and *L95* represent the loop transmission function for the desired travel ranges being 20% (for *P20*), 33% (for *P33*), 50% (for *P50*), 75% (for *P75*) and 95% (for *P95*) of the full gap.

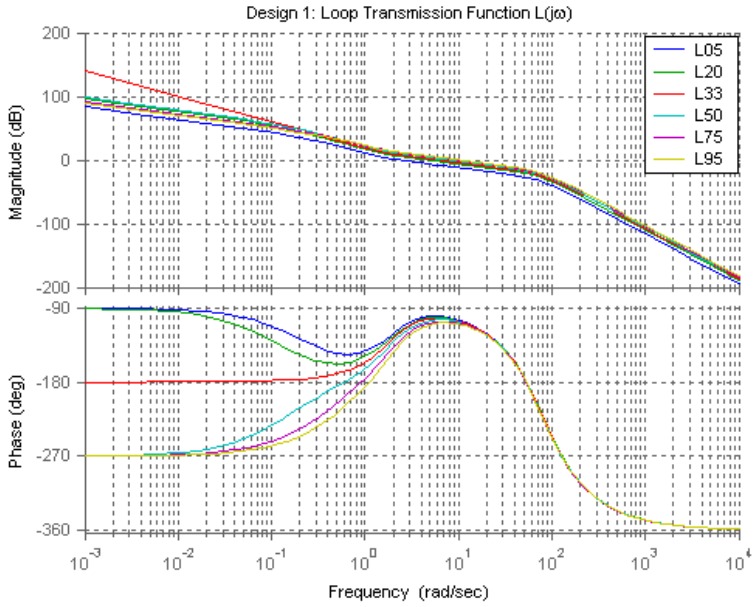

Figure 28: Bode Diagram of the Loop Transmission Function (4.4) for Design 1

We can see from the phase plot in Figure 28 that three of the plants have poles in the RHP (*P50*, *P75*, *P95*), one has a pole at the origin (*P33*), and the other two are stable (*P05*, *P20*). The plant denoted by *P33* is the linearized plant at the pull-in displacement. Table VII shows the gain (GM) and phase (PM) margins of the loop transmission transfer function (4.4) with different desired travel ranges for the first design.

TABLE VII: STABILITY MARGINS FOR DESIGN 1 $(\omega_o = 50)$

Plant Model	**Lower GM (dB)**	**Upper GM (dB)**	**PM (degrees)**	**BW (rad/sec)**
P05	NA	27.9	61.7	2.96
P20	NA	21.9	77.8	6.80
P33	NA	19.6	77.6	9.08
P50	-29.4	17.8	75.3	11.3
P75	-23.8	16.0	71.7	14.0
P95	-21.7	15.0	69.1	15.9

From Table VII, we can see that this design provides sufficient gain and phase margins.

Figure 29 shows the step responses (normalized displacement x) of the classic LADRC control system to the unit reference inputs (r) at 5%, 20%, 33%, 50%, 75%, and 95% of the full gap respectively for the first design. The transfer function from the reference input (r) to the normalized displacement (x) is given by (2.88).

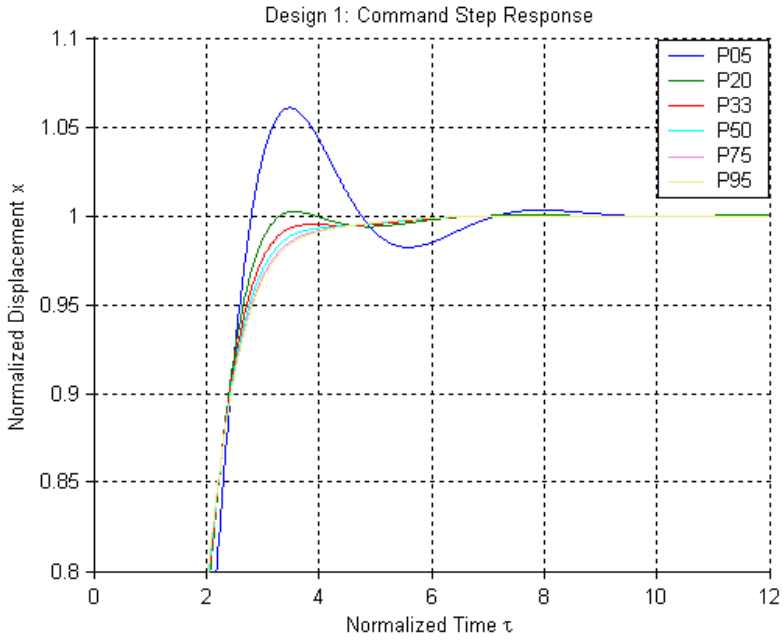

Figure 29: Step Responses of the First Design

In Figure 29, the largest overshoot percentage of 6% occurred for the plant transfer function of *P05*. The *P05* plant's overshoot is attributable to a dominant pair of underdamped low frequency poles in the closed loop transfer function. The overshoot at the small displacement (5% of full gap) is not much of a concern. However, at large displacements, big overshoot would lead to the upper and lower electrodes touching. Then the two electrodes could adhere together, causing the effect known as static friction.

In Figure 29, the step responses at the other displacements (except for *P05*) appear to follow the reference signal very well. Thus we can say that the first design of the classic LADRC shows excellent tracking performance. A comparison study of the percent Over-Shoot (%OS) and the Integral of the Squared Error (ISE) of the three designs will be shown at the end of Section 4.1.2.

4.1.2.2 Design 2

In design two, a more conservative observer bandwidth is selected. The tuning parameters for this design from Table VI are: $\omega_c = 2$, $\omega_o = 30$, $\hat{b} = 0.78$. The controller for this design is shown in (4.9).

$$C(s) = \frac{1{,}953{,}539(s+1.232)(s^2+2.836s+3.451)}{s(s+65.4)(s^2+60.6s+2169)} \tag{4.9}$$

The prefilter used in this design for command following is given in (4.10).

$$H_r(s) = \frac{10.3(s+30)^4}{s(s+65.4)(s^2+60.6s+2169)} \tag{4.10}$$

The Bode diagrams of the loop transmission function (4.4) corresponding to different displacements of the actuator are shown in Figure 30 for the second design.

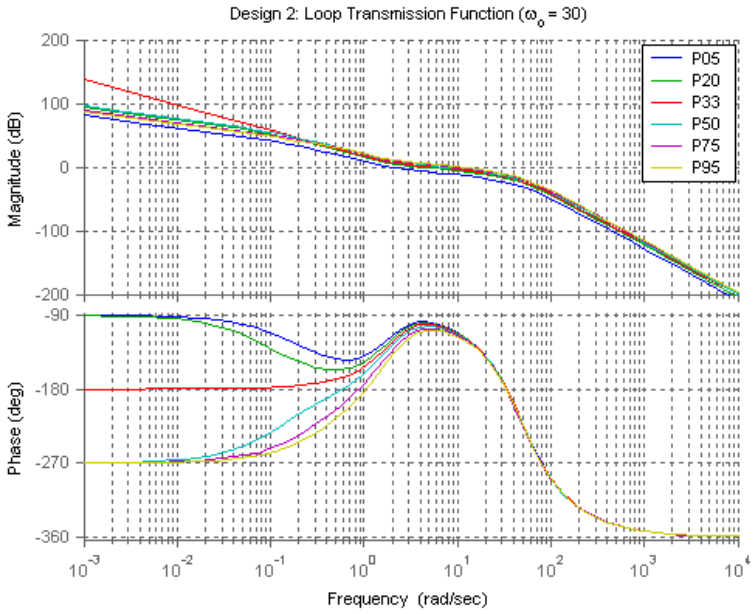

Figure 30: Bode Diagram of the Loop Transmission Function (4.4) for Design 2

Comparing the Bode phase plot of Figure 30 with Figure 28 we can see that the width of the frequency range of phase lead is larger for the higher bandwidth ESO (in design one). This reduction in the amount of phase lead in Figure 30 could have the effect of reduced phase margins for the set of linearized plants. Table VIII shows the gain and phase margins of (4.4) for the second design.

TABLE VIII: STABILITY MARGINS FOR DESIGN 2 $(\omega_o = 30)$

Plant Model	**Lower GM (dB)**	**Upper GM (dB)**	**PM (degrees)**	**BW (rad/sec)**
P05	NA	24.3	60.1	2.48
P20	NA	18.2	79.5	6.20
P33	NA	16.0	77.8	8.40
P50	-27.8	14.2	73.4	10.6
P75	-22.2	12.4	67.4	13.1
P95	-20.1	11.3	63.3	14.7

From Table VIII, we can see that the second design has reduced phase and gain margins as compared to design 1. The reduction in phase margin is most notable at the larger displacements (which are 50%, 75%, and 95% of full gap). The *P95* plant loses 5.8° of phase lead and 4.7 dB on its upper gain margin. The bandwidth in design 2 is also reduced but not significantly compared to design 1. Figure 31 shows the step responses for the classic LADRC control system to different reference inputs in design 2.

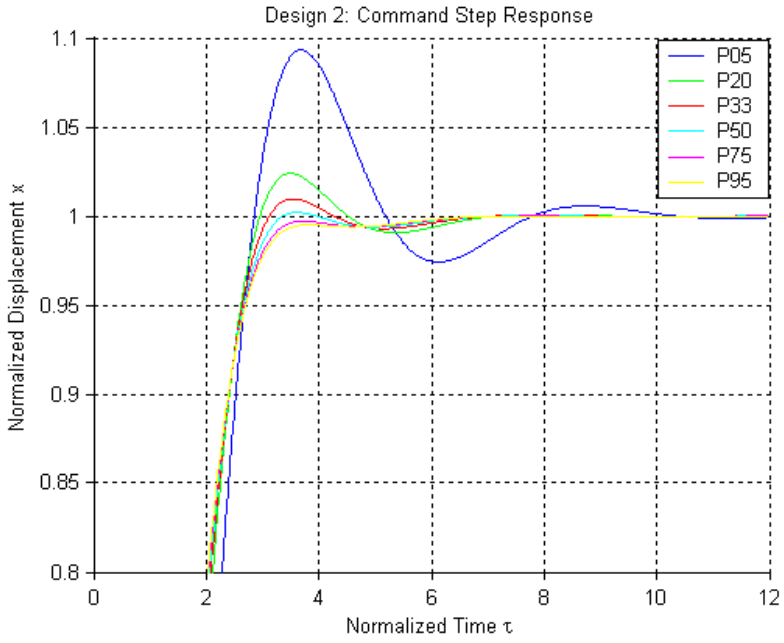

Figure 31: Step Responses of the Second Design

From Figure 29 and Figure 31, we can see that the overshoot percentage is increasing with the decreased observer bandwidth in design 2. In Figure 31, *P05* shows 9% overshoot at t = 3.6 seconds. The two transfer functions *P20* and *P33* exhibit overshoot of 2% and 1% respectively. The three functions *P50*, *P75*, and *P95* with higher displacements still do not exhibit noticeable overshoot.

4.1.2.3 Design 3

The third design is the most practical design of the three since we choose smallest observer bandwidth in this design. The design parameters for design 3 from Table V are: $\omega_o = 20$, $\omega_c = 2$, and $\hat{b} = 0.65$.

The controller and prefilter are given by (4.11) and (4.12) respectively.

$$C(s) = \frac{586{,}830.8(s+1.151)(s^2+2.423s+2.917)}{s(s+45.2)(s^2+40.8s+1048)} \tag{4.11}$$

$$H_r(s) = \frac{12.3(s+20)^4}{s(s+45.2)(s^2+40.8s+1048)} \tag{4.12}$$

The Bode diagrams of the loop transmission function (4.4) corresponding to different displacements of the actuator are shown in Figure 32 for the third design.

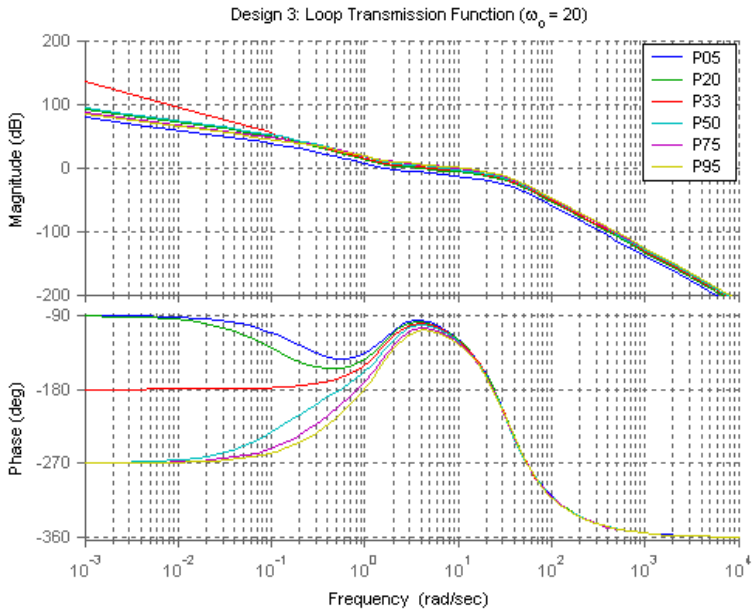

Figure 32: Bode Diagram of the Loop Transmission Function (4.4) for Design 3

The gain and phase margins of the loop transmission function for the third design are shown in Table IX. In Table IX, the gain margins of the *P75* and *P95* have been reduced to 10.2 *dB* and 9.13 *dB* respectively compared to design 1 and design 2. The phase margins for the *P05* and *P95* plants have fallen below 60°. The bandwidth is also reduced in this design. Figure 33 demonstrates the step responses for the six operating points in design 3.

TABLE IX: STABILITY MARGINS FOR DESIGN 3 $(\omega_o = 20)$

Plant Model	**Lower GM (dB)**	**Upper GM (dB)**	**PM (degrees)**	**BW (rad/sec)**
P05	NA	22.2	56.6	1.92
P20	NA	16.1	80.7	5.22
P33	NA	13.9	79.6	7.30
P50	-25.8	12.1	73.5	9.32
P75	-20.1	10.2	65.1	11.6
P95	-18.0	9.13	59.6	13.1

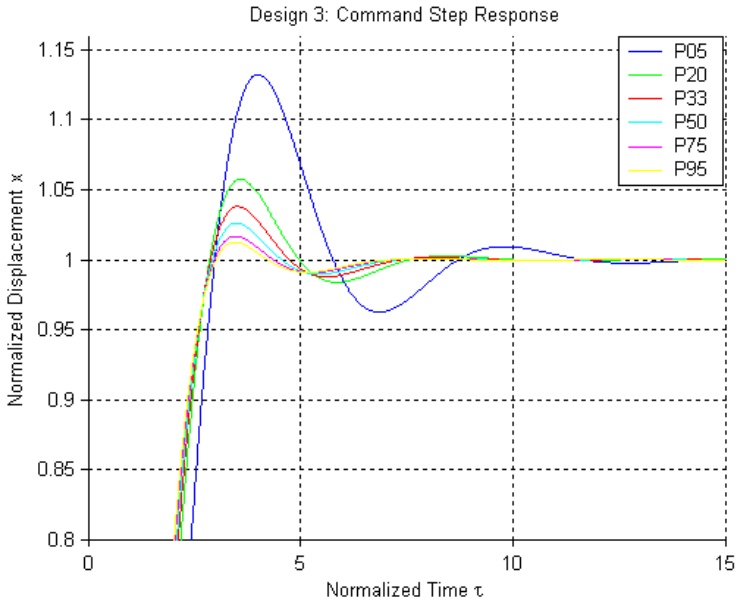

Figure 33: Step Responses of the Third Design

Figure 33 shows significant overshoot at small displacements. The actuator exhibits overshoot at all displacements. *P05* has an overshoot of 13% in this design. *P95* has an overshoot of 1% in this design. The overshoot at higher displacements is going to limit the effective travel range of the electrostatic actuator.

4.1.2.4 Design Comparison

Figure 34 shows the step responses of all three designs for the linearized model of the actuator with the displacement of 99% of the full gap.

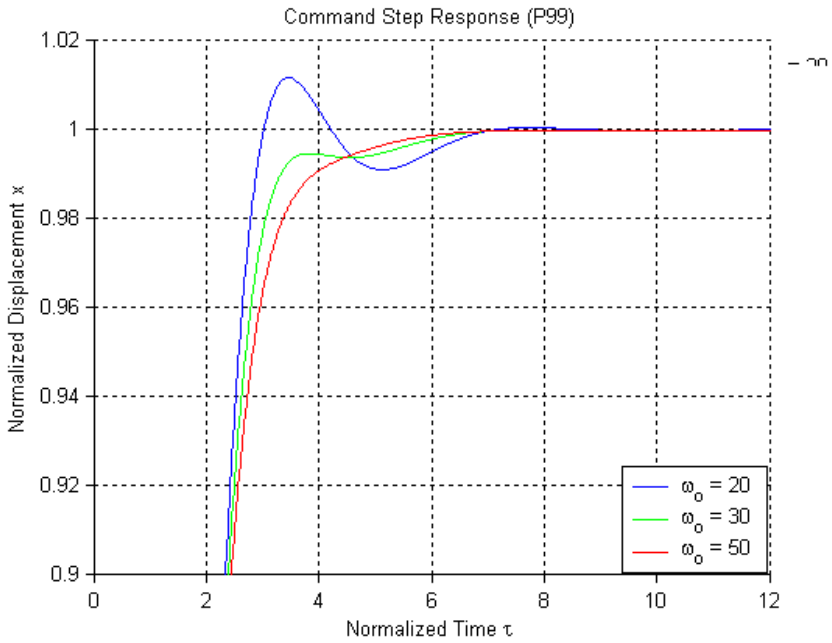

Figure 34: Step Responses of the Three Classic ADRC Designs for the Actuator with the Displacement of 99% of Full Gap

From Figure 34, one can see that the step response for design 3 ($\omega_o = 20\,rad/s$) shows a maximum overshoot percentage of 1%. This overshoot will limit the effective

travel range of the actuator to 99% of the full gap. In order to provide a quantitative measure of the tracking performances of the designs in this section the Integral-Squared-Error (ISE) is used. Equation (4.13) gives the general definition for the ISE, in which *r* is the setpoint, and *x* is the measured output.

$$ISE(e) = \int e^2(t)\,dt \qquad e = r - x \tag{4.13}$$

Tables X and XI show the Over-Shoot (%OS) percentages and ISE for the three designs. Table X clearly demonstrates that the low loop gain/bandwidth of the models linearized around small displacements leads to larger tracking error. Table X also shows that increasing the observer bandwidth reduces the tracking error. Table XI shows that the increasing the observer bandwidth also has the effect of increasing system damping over the operating range of the electrostatic actuator.

TABLE X: INTEGRAL OF THE SQUARED ERRORS FOR THE THREE DESIGNS

ISE			
Plant	*Design 1*	*Design 2*	*Design 3*
P05	1.2743	1.3369	1.4368
P20	1.1396	1.1692	1.2186
P33	1.1059	1.1267	1.1619
P50	1.0828	1.0974	1.1226
P75	1.0619	1.0707	1.0866
P95	1.0502	1.0560	1.0666
P99	1.0482	1.0534	1.0631

TABLE XI: OVERSHOOT PERCENTAGES OF THE THREE DESIGNS

%OS			
Plant	*Design 1*	*Design 2*	*Design 3*
P05	6	9	13
P20	NA	2	6
P33	NA	1	4
P50	NA	NA	3
P75	NA	NA	2
P95	NA	NA	1
P99	NA	NA	1

Figure 35 demonstrates the Bode diagrams for the three classic ADRC designs.

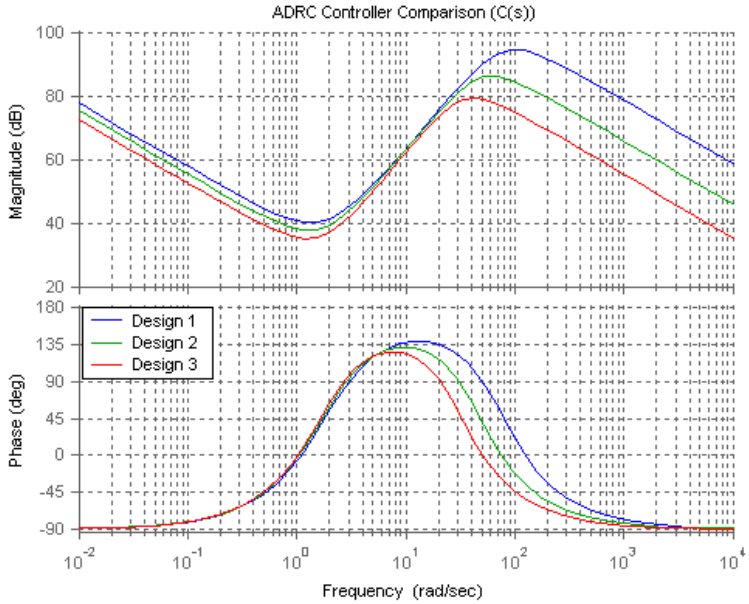

Figure 35: Bode Diagrams of the Control Systems for the Three Designs

Figure 35 shows that the frequency range of phase lead is reduced with the decrease of the bandwidth (ω_o) of the ESO. It also shows the high frequency gain will result in noise amplification of the 3 ADRC designs. In these designs, phase lead is sacrificed for reduced high frequency gain as the observer bandwidth is reduced. This is a classic tradeoff between system stability and noise attenuation. The effects of sensor noise will be further investigated in Section 4.3.

The performance data presented in this section consist of the percentage of overshoot and the ISE of the tracking error. Stability was also investigated with the use of phase and gain margins, with special emphasis on maximizing the phase margin across the entire set of operating points. Based on the stability and performance data, design 1 appears to be the most promising design, followed by design 2 and then design 3. Design 1 shows the benefits of a high gain/bandwidth controller. The cost associated with the use of the high gain controller is its increased sensitivity to noise. The effects of sensor noise and the noise attenuation capabilities of the three designs will be discussed in Section 4.3.

4.2 LADRC 4th Order Alternative Design

For the classic ADRC, both the internal dynamics and external disturbances are taken as an unknown generalized disturbance. An ESO is used to estimate the generalized disturbance. Based on the accurate estimation of the ESO, the ADRC reduces the original system model to a series of cascaded integrators and effectively

controls the reduced model using a PD controller. This classic ADRC minimizes the amount of modeling information required to design the controller. However, if there is additional modeling information available, it can be incorporated into the ESO. This thesis creatively used the partially available modeling information to design the ADRC. The details about this new control strategy will be introduced in the section.

4.2.1 Controller Framework

We consider the general linearized model for an electrostatic actuator given in (4.13).

$$P(s)=\frac{X(s)}{U(s)}=\frac{b}{(s+a_0)(s+a_1)(s+a_2)} \tag{4.13}$$

From Table V in Chapter 2, we can see that the plant gain b (or b_0) and one of the system poles a_2 are the two parameters that vary significantly over the electrostatic actuator's operating range. However, the other two parameters, a_0 and a_1, are not changing much. Therefore, we can assume a_0 and a_1 are known parameters while b and a_2 the unknown parameters. Then the model (4.13) can be divided into known and unknown parts as shown in (4.14).

$$P(s)=\frac{X(s)}{U(s)}=\underbrace{\frac{1}{(s+a_0)(s+a_1)}}_{known}\underbrace{\frac{b}{(s+a_2)}}_{unnkown} \tag{4.14}$$

We suppose the best estimate for the plant gain b is given by $\hat{b}$. After the control of the ADRC, the original electrostatic model (4.14) can be reduced to a nominal model which

is given by (4.15), where the known parts of the system remain while the uncertain part $b/(s+a_2)$ is reduced to an integrator.

$$P_n(s)=\frac{\hat{b}}{s(s+a_0)(s+a_1)} \tag{4.15}$$

Equation (4.14) can be also rewritten as (4.16).

$$\dddot{x}=-(a_0+a_1+a_2)\ddot{x}-(a_0a_1+a_0a_2+a_2a_1)\dot{x}-(a_0a_1a_2)x+bu \tag{4.16}$$

Let $f(\cdot)$ include all the unknown terms on the right hand side of (4.16), that is $f(\cdot)=-a_0\dddot{x}-a_0(a_1+a_2)\dot{x}-a_0a_1a_2x+(b-\hat{b})u$. Equation (4.16) can be rewritten as

$$\dddot{x}=-(a_1+a_2)\ddot{x}-(a_1a_2)\dot{x}+f(\ddot{x},\dot{x},x,(b-\hat{b})u)+\hat{b}u. \tag{4.17}$$

The generalized disturbance $f(\cdot)$ is estimated by an ESO. This estimate is fed back in the control law to decouple the disturbance dynamics. With the accurate estimation of the ESO, (4.17) can be reduced to (4.18).

$$\dddot{x}=-(a_1+a_2)\ddot{x}-(a_1a_2)\dot{x}+\hat{b}u \tag{4.18}$$

The plant of (4.17) can be controlled with the 2-DOF control law given in (4.19), where $\hat{f}(\cdot)$ is the estimate of $f(\cdot)$.

$$u=\frac{1}{\hat{b}}\left[K_1(r-x)-K_2\dot{x}-K_3\ddot{x}-\hat{f}(\cdot)\right] \tag{4.19}$$

Incorporating (4.19) into (4.17) results in the system described by (4.20).

$$\dddot{x}=-(a_1+a_2+K_3)\ddot{x}-(a_1a_2+K_2)\dot{x}-K_1x+K_1r \tag{4.20}$$

In addition to estimating the generalized disturbance $f(\cdot)$, the ESO will estimate the unmeasured system states $\ddot{x}$ and $\dot{x}$, and provide a filtered estimate of the measured displacement *x*. The differential equation describing the state observer is given in (4.21).

$$\dot{z} = (A - LC)z + Bu + Ly \tag{4.21}$$

Taking the Laplace transform of (4.21) results in (4.22).

$$Z(s) = (sI - A + LC)^{-1}[BU(s) + LY(s)] \tag{4.22}$$

In (4.22), the matrix *A*, and the vectors *L*, *B*, and *C* are defined in (3.71). The matrix $(sI - A + LC)$ is given in (4.23).

$$(sI - A + LC) = \begin{bmatrix} s + L_1 & -1 & 0 & 0 \\ L_2 & s & -1 & 0 \\ L_3 & a_1 a_2 & s + a_1 + a_2 & -1 \\ L_4 & 0 & 0 & s \end{bmatrix} \tag{4.23}$$

The inverse of the determinant of (4.23) gives is

$$\frac{1}{\det(sI - A + LC)} = \frac{1}{s^4 + A_0 s^3 + A_1 s^2 + A_2 s + A_3}. \tag{4.24}$$

The coefficients of the denominator of (4.24) are given in (4.25).

$$\begin{aligned} A_0 &= a_1 + a_2 + L_1 \\ A_1 &= a_1 a_2 + L_1(a_1 + a_2) + L_2 \\ A_2 &= L_1(a_1 a_2) + L_2(a_1 + a_2) + L_3 \\ A_3 &= L_4 \end{aligned} \tag{4.25}$$

The inverse of (4.23) is given in (4.26).

$$(sI - A + LC)^{-1} = \frac{1}{\det(sI - A + LC)}[G_1 \quad G_2 \quad G_3 \quad G_4] \tag{4.26}$$

In (4.26), the column vectors of $\begin{bmatrix} G_1 & G_2 & G_3 & G_4 \end{bmatrix}$ are provided in (4.27-4.30)

$$G_1 = \begin{bmatrix} s(s+a_1)(s+a_2) \\ -\left(L_2 s^2 + (L_2(a_1+a_2)+L_3)s + L_4\right) \\ -s(L_3 s - L_2 a_1 a_2 + L_4) \\ -L_4(s+a_1)(s+a_2) \end{bmatrix} \tag{4.27}$$

$$G_2 = \begin{bmatrix} s(s+a_1+a_2) \\ s(s+L_1)(s+a_1+a_2) \\ -\left(a_1 a_2 s^2 + (L_1 a_1 a_2 + L_3)s + L_4\right) \\ -L_4(s+a_1+a_2) \end{bmatrix} \tag{4.28}$$

$$G_3 = \begin{bmatrix} s \\ s(s+L_1) \\ s(s^2 + L_1 s + L_2) \\ -L_4 \end{bmatrix} \tag{4.29}$$

$$G_4 = \begin{bmatrix} 1 \\ s+L_1 \\ s^2 + L_1 s + L_2 \\ s^3 + A_0 s^2 + A_1 s + A_2 \end{bmatrix} \tag{4.30}$$

As stated in (3.55), the matrix *M* is defined in (4.31).

$$M = (sI - A + LC)^{-1} \tag{4.31}$$

Again, we suppose the controller $C(s)$ is in the feedback path of the ADRC controlled closed loop system as shown in Figure 25. The controller and prefilter are given by (3.82) and repeated in (4.32).

$$C(s) = \frac{KML}{\hat{b} + KMB}, \quad H(s) = \frac{K_1}{\hat{b} + KMB} \tag{4.32}$$

The term *KMB* in (4.32) is computed as in (4.33).

$$KMB = \frac{\hat{b}\left(K_3 s^3 + (K_2 + K_3 L_1)s^2 + (K_1 + K_2 L_1 + K_3 L_2)s - L_4\right)}{s^4 + A_0 s^3 + A_1 s^2 + A_2 s + A_3} \tag{4.33}$$

The result of $(\hat{b} + KMB)$ is given in (4.34).

$$\hat{b} + KMB = \frac{\hat{b}s\left(s^4 + B_0 s^3 + B_1 s^2 + B_2\right)}{s^4 + A_0 s^3 + A_1 s^2 + A_2 s + A_3} \tag{4.34}$$

The numerator coefficients of (4.34) are given in (4.35).

$$\begin{aligned} B_0 &= (K_3 + A_0) \\ B_1 &= (K_2 + K_3 L_1 + A_1) \\ B_2 &= (K_1 + K_2 L_1 + K_3 L_2 + A_2) \end{aligned} \tag{4.35}$$

The equation that describes the prefilter is given by (4.36).

$$H(s) = \frac{1}{\hat{b}} \cdot \frac{K_1\left(s^4 + A_0 s^3 + A_1 s^2 + A_2 s + A_3\right)}{s^4 + B_0 s^3 + B_1 s^2 + B_2 s} \tag{4.36}$$

The term *KML* in (4.32) is derived as in (4.37).

$$KML = \frac{N_1 s^3 + N_2 s^2 + N_3 s + N_4}{s^4 + A_0 s^3 + A_1 s^2 + A_2 s + A_3} \tag{4.37}$$

The numerator coefficients of (4.37) are presented in (4.38).

$$\begin{aligned} N_1 &= K_1 L_1 + K_2 L_2 + K_3 L_3 + L_4 \\ N_2 &= K_1 L_2 + K_2 L_3 + K_3 L_4 + (K_1 L_1 + K_2 L_2 + L_4)(a_1 + a_2) - a_1 a_2 L_2 K_3 \\ N_3 &= K_1 L_3 + K_2 L_4 + a_1 a_2 (K_1 L_1 + L_4) + (a_1 + a_2) K_1 L_2 \\ N_4 &= K_1 L_4 \end{aligned} \tag{4.38}$$

Substituting (4.34) and (4.37) into (4.32), we will have

$$C(s) = \frac{1}{\hat{b}} \cdot \frac{N_1 s^3 + N_2 s^2 + N_3 s + N_4}{s^4 + B_0 s^3 + B_1 s^2 + B_2 s}. \tag{4.39}$$

As stated in Chapter 3, the controller gains K_1, K_2, and K_3 in (4.19) are chosen to produce real repeated poles ω_c for the desired transfer function of the closed-loop system. The controller gains are given in (4.40).

$$\begin{aligned} K_1 &= \omega_c^3 \\ K_2 &= 3\omega_c^2 - a_1 a_2 \\ K_3 &= 3\omega_c - (a_1 + a_2) \end{aligned} \tag{4.40}$$

If we make a comparison between (3.108) and (4.40), we will be able to see that the choice of the reduced nominal model represented by (4.14) results in reduced controller gains.

4.2.2 Comparison Study of Classic and Alternative ADRC Designs

In the linear simulations that follow, the classic ADRC design introduced in Section 4.1 and the alternative ADRC design discussed in Section 4.2.1 are going to be compared. The observer bandwidth, controller bandwidth and plant gain estimate are chosen to be the same values for both designs. The controller parameters are

$$\begin{aligned} \omega_c &= 2 \\ \omega_o &= 20\,. \\ \hat{b} &= 0.65 \end{aligned} \tag{4.41}$$

The actual plant that will be used in these simulations is a linearized model of the electrostatic actuator at 95% of the displacement. From Table V in Chapter 2, a_0=3.559,

a_1=1.027, and a_2=-0.5329. Substituting the parameter values of a_0, a_1 and a_2 into (4.13), we will have the actuator model given by (4.42).

$$P_{95} = \frac{0.7898}{(s+1.027)(s+3.559)(s-0.5329)} \tag{4.42}$$

4.2.2.1 Classic ADRC Design

The reduced nominal model that will be used in the classic ADRC design is given in (4.43).

$$P_N = \frac{0.65}{s^3} \tag{4.43}$$

The transfer function of the classic ADRC controller (G_C) that was designed in (4.11) is repeated in (4.44).

$$G_C = \frac{586{,}831(s+1.151)(s^2+2.432s+2.917)}{s(s+45.2)(s^2+40.8s+1048)} \tag{4.44}$$

The transfer function of the prefilter (H) for the classic ADRC design given by (4.12) is repeated in (4.45).

$$H_r = \frac{12.3(s+20)^4}{s(s+45.2)(s^2+40.8s+1048)} \tag{4.45}$$

4.2.2.2 Alternative ADRC Design

From (4.15), the reduced nominal model of (4.42) is represented by (4.46).

$$P_N = \frac{0.65}{s(s+1.027)(s+3.559)} \tag{4.46}$$

The transfer function of the alternative ADRC controller is given by (4.47).

$$G_C = \frac{347{,}149(s+3.455)(s^2+2.432s+1.642)}{s(s+45.2)(s^2+40.8s+1048)} \tag{4.47}$$

The controller gains in (4.40) were chosen so that both the classic ADRC design (4.44) and the alternative ADRC design (4.47) would have the same poles. However the zeros of the two controller designs are different.

The transfer function of the prefilter for the alternate ADRC design given by (4.36) is presented in (4.48).

$$H_r = \frac{12.3(s+39.74)(s+5.129)(s^2+39.72s+784.9)}{s(s+45.2)(s^2+40.8s+1048)} \tag{4.48}$$

4.2.2.3 Classic and Alternative Controller Comparison

The Bode plots of the two controllers (4.44) and (4.47) are shown in Figure 36, in which, the alternative ADRC design sacrifices some phase lead in order to obtain a reduction in magnitude within the mid and high frequency range.

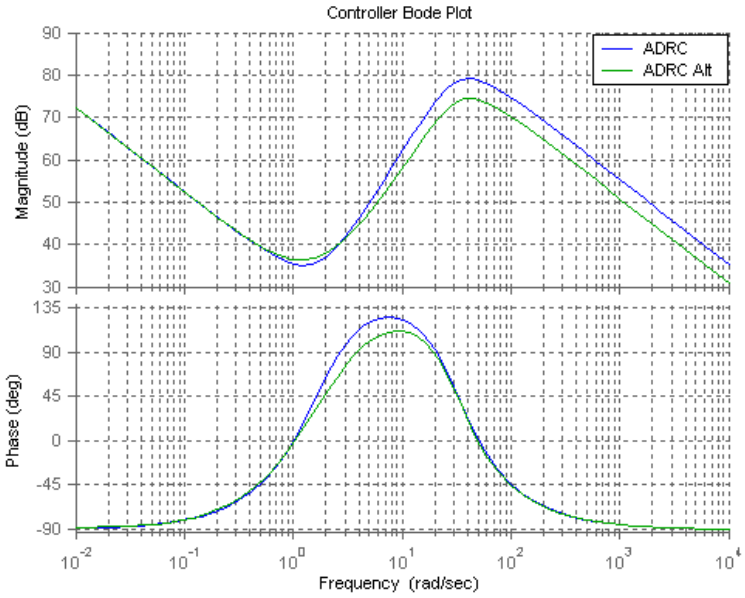

Figure 36: Bode Plots of Classic and Alternative ADRCs

Figure 37 shows the Bode plots of the actuator model (P_{95}) along with the Bode plots of the loop transmission functions ($P_{95}(s)C(s)$) for the two designs.

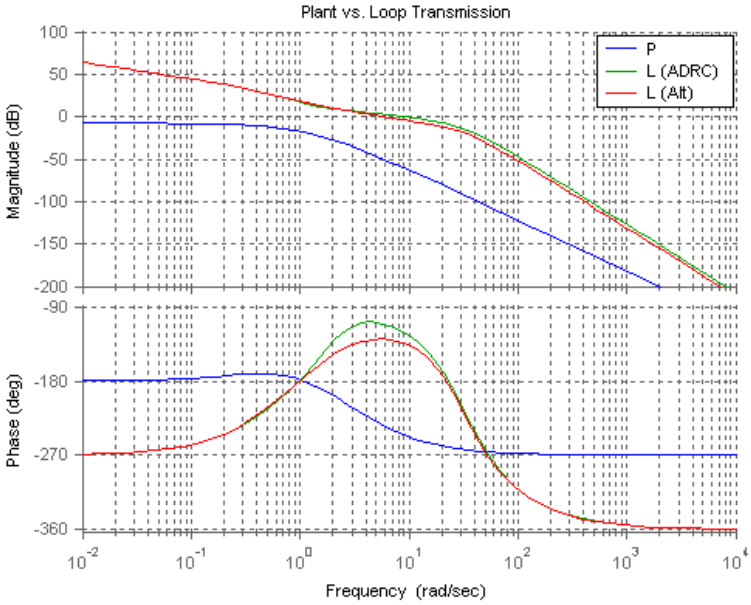

Figure 37: Bode Plots of Actuator Model and the Loop Transmission Functions for Both Classic and Alternative ADRC Designs

Table XII provides the upper and lower gain margins along with the phase margins for both designs.

TABLE XII: ALTERNATE ADRC COMPARISON

Design	**Lower GM (dB)**	**Upper GM (dB)**	**PM (degrees)**	**BW (rad/sec)**
ADRC	-18.0	9.13	59.6	13.0
ADRC Alt	-18.8	12.8	51.3	8.18

From the table, we can see that the alternative ADRC design has improved gain margins but suffers from a reduction of 8.3° of phase margin. The alternative ADRC design also has a much lower bandwidth than the classic ADRC design. This will be beneficial when noise sources are considered.

Figure 38 shows the Bode plots of the transfer functions represented by (2.82), which describes the sensitivity of the controller output to sensor noise, for both classic and alternative ADRC designs.

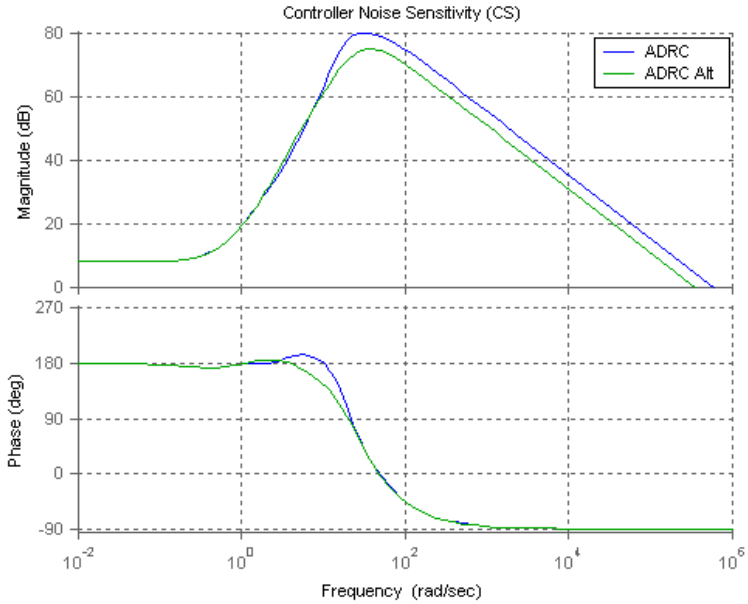

Figure 38: Bode Diagrams of Noise Sensitivity Transfer Functions for the Classic and Alternative ADRC Designs

From Figure 38, we can see that the alternative ADRC design sacrifices a little phase lead in order to decrease the high frequency gain of the controller noise sensitivity transfer function (C(s)S(s)) (2.86). The alternative ADRC design provides an extra 5 dB of noise attenuation at high frequencies.

The Bode plots of the closed-loop input disturbance transfer function (*P(s)S(s)*) (2.87) from an input disturbance to the measured output *x* for both designs are shown in Figure 39.

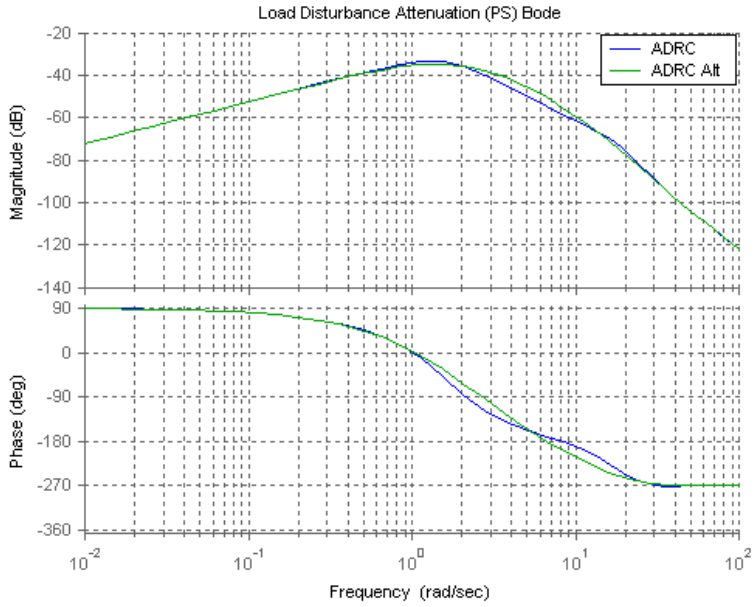

Figure 39: Bode Diagrams of the Closed-loop Transfer Functions between Input Disturbance and Output Displacement for the Classic and Alternative ADRC Designs

From Figure 39, we can see that both designs show excellent input disturbance rejections. The peak magnitude response for the classic ADRC design is -33.3 dB at 1.53 rad/s. The peak magnitude response for the alternative ADRC design is -34.8 dB at 1.53 rad/s.

The step responses of both designs are shown in Figure 40 for the electrostatic actuator model linearized around 95% gap traversal.

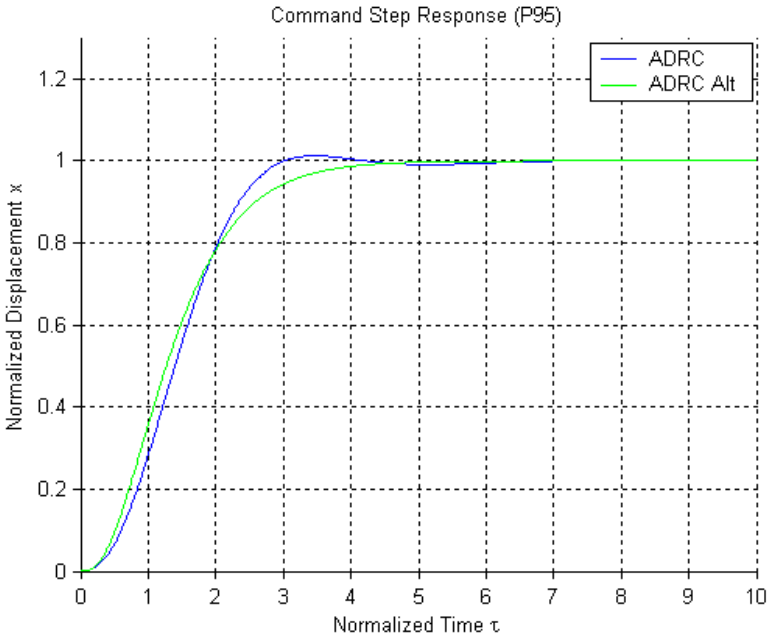

Figure 40: Step Responses of the Classic and Alternative ADRC Designs

From Figure 40, we can see that the step response of the alternative ADRC design reaches the set-point, which is 1, with no overshoot. However, the step response of the classic ADRC design has a slight overshoot of 1% of the commanded value. The responses of both the classic and the alternate ADRC designs reach the set-point at around 5 seconds. The ISE for the classic ADRC design is 1.0666, which is larger than the ISE for the alternative ADRC design that is 0.9765. Therefore, the tracking performance of the alternative ADRC design is better than the one of the classic ADRC design from the figure. In the next section the noise sensitivity of both designs will be investigated.

4.3 Controller Noise Analyses

In Figure 25 and Figure 26 of Chapter 3, we can see the noise present at the controller output is the key design constraint. Magnification of sensor noise is one of the costs of feedback control. In this section the noise sensitivity of the control system for the electrostatic actuator will be investigated in detail. In Section 4.3.1 some key transfer functions that will help with noise analyses are defined. Section 4.3.2 will demonstrate the sensitivities of the electrostatic actuator itself and the ADRC controlled actuators to a white noise source.

4.3.1 Electrostatic Actuator Noise Analysis

As analyzed in Chapter 2, the original Electro-Static Actuator (ESA) system is not stable over its entire operating range. The number of RHP poles increases from zero to one as the gap traversal moves beyond 1/3 of the initial gap. This RHP pole enforces a lower bound on the closed-loop bandwidth that one must achieve for a stable control system. The ESA is also subject to very small system gain. It will be seen in this section that this small system gain will contribute to the amplification of sensor noise. Both the RHP pole problem and the small system gain issues can be handled with a high-gain (high-bandwidth) controller. However, a high-bandwidth controller will magnify sensor noise. Thus sensor noise is going to be the limiting factor in how well the control system performs. In order to investigate how susceptible the controller is to noise we have to look at one of the operating points of the ESA. As the gap traversal of the actuator is 80% of the full gap, the actuator model can be represented by (4.49).

$$P80 = \frac{0.725}{(s+3.58)(s+1.03)(s-0.40)} \tag{4.49}$$

From (4.49) we can see that at this operating point, there is one RHP pole that is fairly close to the origin, which is good from a control's perspective because the farther this RHP pole is from the origin, the larger the price that must be paid to bring it into the LHP for stability. The DC gain of the actuator system represented by (4.49) is given in (4.50). It will be seen that the gain in (4.50) has a profound effect on low frequency noise amplification.

$$\frac{0.725}{(3.58)(1.03)(0.40)} \approx 0.4915 \tag{4.50}$$

4.3.1.1 Classic ADRC Comparison

The classic ADRC with two different sets of tuning parameters will be compared in this section. Both ADRC designs can track step references and step disturbances with zero steady-state errors. Since the electrostatic actuator is a third-order plant, the ESO is fourth-order. The two designs that will be compared are selected from Section 4.1.2. They are design 1 and design 3 respectively. The tuning parameters for design 1 and design 3 are given in Table XIII.

TABLE XIII: TUNING PARAMETERS OF CLASSIC LADRC CONTROLLERS

Design	ω_c	ω_o	$\hat{b}$
1	2	50	1.1
3	2	20	0.65

Both designs are implemented in transfer function form and are controlled by 2-DOF controllers consisting of a prefilter and a feedback controller. Since this thesis only deals with the sensor noise in the feedback loop (as shown in Figure 25) the prefilter can safely be ignored for this analysis. The feedback controllers of design 1 (C_1) and design 3 (C_3) are given by (4.51) and (4.52) respectively. The Bode diagrams of the two controllers ((4.51) and (4.52)) are shown in Figure 41.

$$C_1 = \frac{6{,}287{,}733(s+1.322)(s^2+3.303s+4.009)}{s(s+105.6)(s^2+100.4s+5610)} \tag{4.51}$$

$$C_3 = \frac{762{,}880(s+1.151)(s^2+2.423s+2.917)}{s(s+45.2)(s^2+40.8s+1048)} \tag{4.52}$$

We can see from Figure 41 that design 1 is the higher gain/bandwidth controller. In the low frequency range ($\omega < 1$ rad/s) design 1 has approximately 6 dB more gain than design 3. This will allow design 1 to benefit from improved command following and disturbance rejection. However, in the high frequency range ($\omega > 100$ rad/s) design 1 has approximately 20 dB more gain than design 3. This additional gain will help contribute to sensor noise amplification. Sensor noise amplification is the limiting factor in the achievable performance of the ADRC designs in this section.

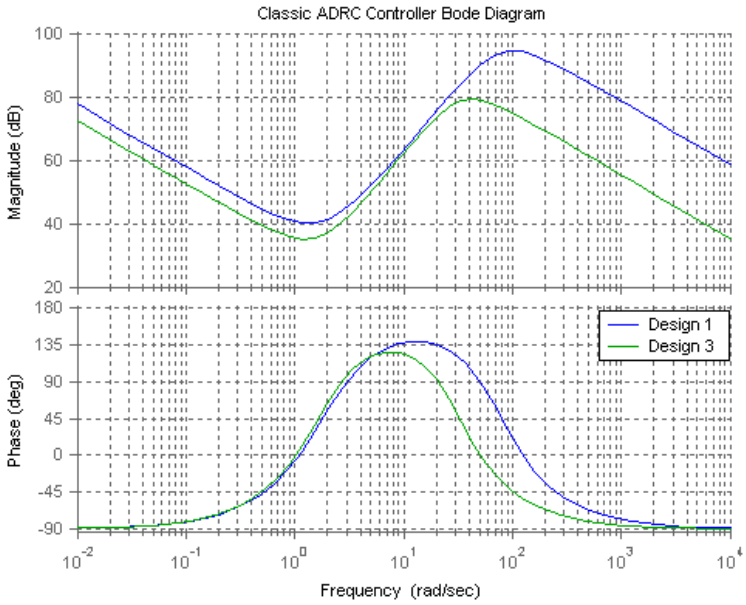

Figure 41: Bode Plots of the Controllers (C_1 and C_3) for Design 1 and Design 3

The equations of (4.51) and (4.52) can be rewritten as (4.53) and (4.54).

$$C_1 = 56.2516\left(\frac{105.6}{1.322}\right)\left(\frac{5610}{4.009}\right)\frac{(s+1.322)}{s(s+105.6)}\frac{\left(s^2+3.303s+4.009\right)}{\left(s^2+100.4s+5610\right)} \tag{4.53}$$

$$C_3 = 54.0715\left(\frac{45.2}{1.151}\right)\left(\frac{1048}{2.917}\right)\frac{(s+1.151)}{s(s+45.2)}\frac{\left(s^2+2.423s+2.917\right)}{\left(s^2+40.8s+1048\right)} \tag{4.54}$$

From (4.53) and (4.54), we can see that both designs include integral action. The integral action provides zero steady-state error to step disturbances. The pole/zero locations for the real valued lead compensators (represented by C_{lag1} and C_{lag3}) are given in (4.55) and (4.56).

$$C_{lag1} = \frac{s+1.322}{s} \tag{4.55}$$

$$C_{lag3} = \frac{s+1.151}{s} \tag{4.56}$$

The pole/zero locations for the complex valued lead compensators (represented by C_{lead1} and C_{lead3}) are given in (4.57) and (4.58).

$$C_{lead1} = \sqrt{\frac{5610}{4.009}} \cdot \left(\frac{s^2 + 3.303s + 4.009}{s^2 + 100.4s + 5610} \right) \tag{4.57}$$

$$C_{lead3} = \sqrt{\frac{1048}{2.917}} \cdot \left(\frac{s^2 + 2.423s + 2.917}{s^2 + 40.8s + 1048} \right) \tag{4.58}$$

In (4.57), C_{lead1} is the complex lead component of the controller (C_1) of design 1 and C_{lead3} is the complex lead component of controller (C_3) of design 3. The complex lead controller yields the same peak amount of phase lead but with less amplitude gain when compared to a second order real lead controller.

Single-pole low pass filters (LPF) represented by C_{lpf1} and C_{lpf2} are given by (4.59) and (4.60).

$$C_{lpf1} = \frac{105.6}{s + 105.6} \tag{4.59}$$

$$C_{lpf3} = \frac{45.2}{s + 45.2} \tag{4.60}$$

From the two equations above, we can see that the corner frequency for design 1 is 105.6 rad/s, the corner frequency for design 3 is 45.2 rad/s. Since the bandwidth of design 1 is larger than that of design 3, the latter will be less susceptible to sensor noise than the former.

The constant gains of the two controllers C_1 and C_3 are given in (4.61) and (4.62)

$$C_{p1} = \frac{56.2516}{1.322} \cdot \sqrt{\frac{5610}{4.009}} \approx 1591.72 \tag{4.61}$$

$$C_{p3} = \frac{54.0715}{1.151} \cdot \sqrt{\frac{1048}{2.917}} \approx 890.44 \tag{4.62}$$

Figure 42 shows the Bode plots for the phase lag, phase lead, LPF and constant gain components of design 1. Figure 43 shows the Bode Diagrams for the phase lag, phase lead, LPF and constant gain components of design 3.

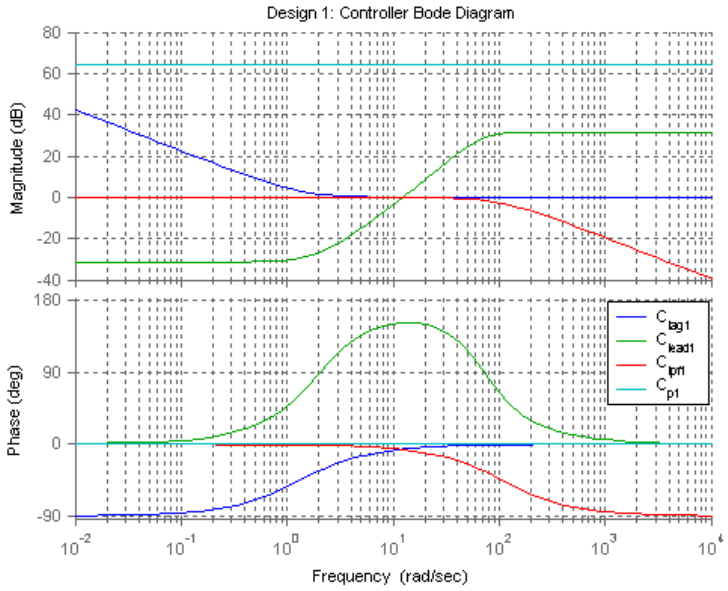

Figure 42: Bode Diagrams of Lead, Lag, LPF, and Constant Gain Components of the Classic LADRC for Design 1

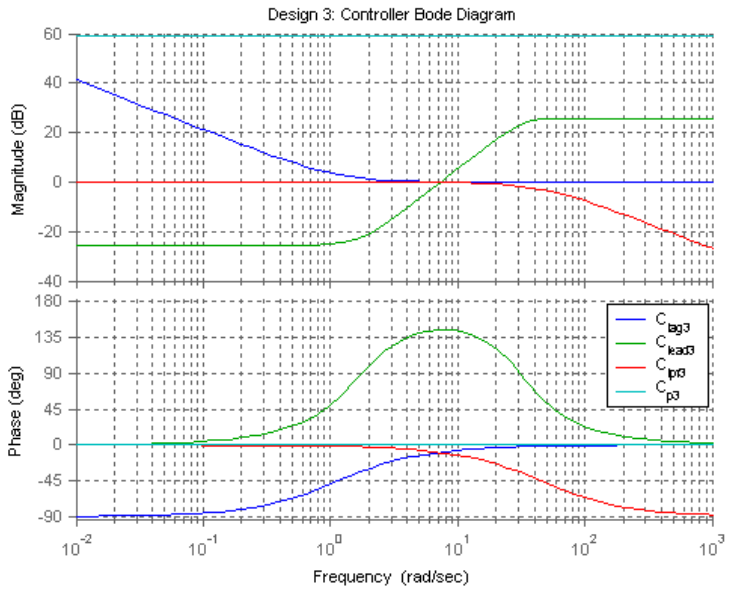

Figure 43: Bode Diagrams of Lead, Lag, LPF, and Constant Gain Components of the Classic LADRC for Design 3

Figure 44 clearly shows the magnitude frequency responses of the electrostatic actuator and the loop transmission function for design 1 (L_1) and design 3 (L_3). From Figure 44, we can see that the high frequency gain of design 3 is reduced at the expense of phase lead.

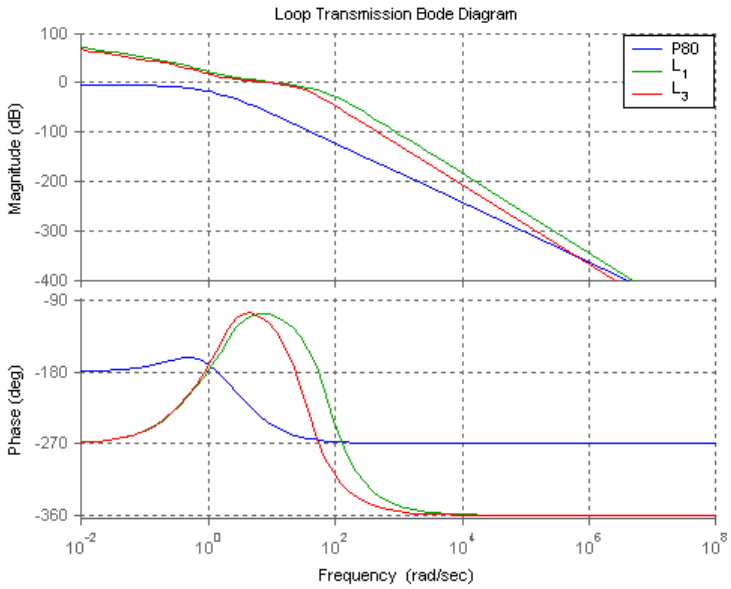

Figure 44: Bode Plots of the Actuator System and Loop Transmission Functions for Design 1 and Design 3

In Figure 44, the magnitude of L_3 intersects the magnitude of the plant (*P80*) at a frequency of approximately 10^6 rad/s. The controller will amplify sensor noise in the frequency range where the magnitude of the loop gain $|L(j\omega)|$ is greater than the magnitude of the plant *P80*. This noise amplification effect can be more clearly seen in Figure 45, which shows the magnitude frequency responses of the actuator plant, the loop transmission function, and the controller noise sensitivity function (*C(s)S(s)*) in (2.87) for design 3.

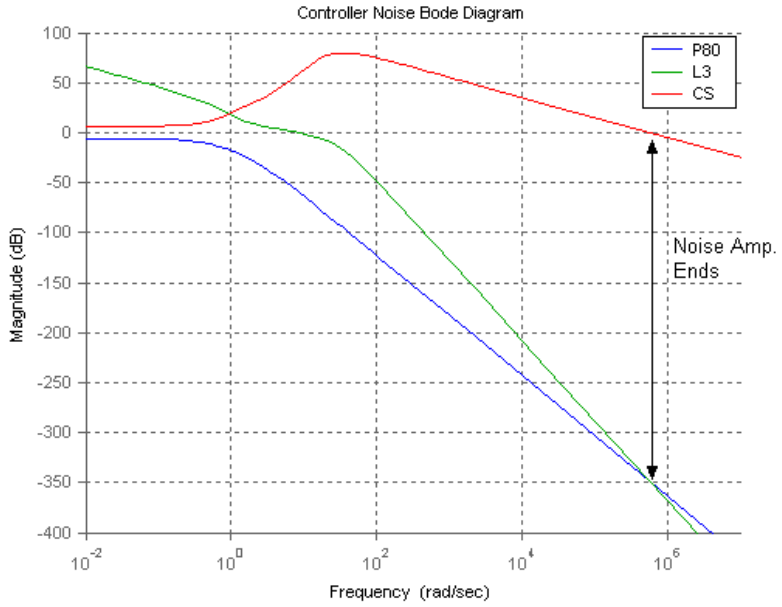

Figure 45: Magnitude Frequency Responses of the Actuator System, Loop Transmission Function, and Controller Noise Sensitivity Function for Design 3

Figure 45 shows the relationship between the controller noise sensitivity function *C(s)S(s)* (2.87) and the loop transmission function $L(j\omega)$ (2.84) for design 3. We can see that as long as the loop transmission function $L(j\omega)$ has a greater magnitude than the plant, sensor noise is amplified. Figure 46 shows the Bode diagram of the inverse of the actuator transfer function, the controller transfer function, and the controller noise sensitivity function (*C(s)S(s)*) for design 3. It shows how the plant and the controller contribute to the closed loop noise amplification.

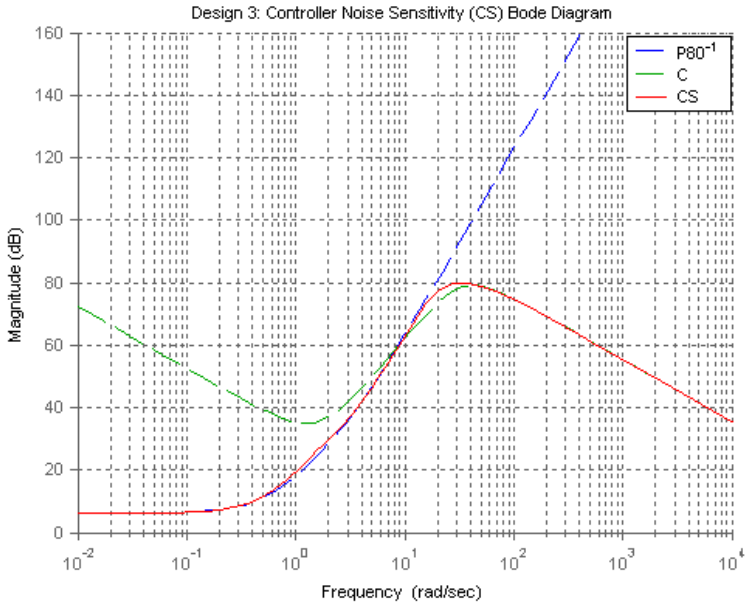

Figure 46: Magnitude Frequency Response of Controller Noise Sensitivity Function for Design 3

Figure 46 demonstrates the dependency of the controller noise sensitivity function *C(s)S(s)* on the plant (*P80*) and the controller (*C*). We can see that the noise amplification in the frequency range where the magnitude of the controller *C* is large, relative to the magnitude of the plant, the controller noise sensitivity (*C(s)S(s)*) function tracks the inverse of the plant. The controller has no effect on attenuating the noise in this frequency range since it is solely dependent on the plant. With the low plant gain of the electrostatic actuator this will result in increased low frequency noise amplification. During the frequency range in which the magnitude of the loop gain $L(j\omega) = P(j\omega)C(j\omega)$ is small (at high frequencies), *C(s)S(s)* tracks the controller *C*. Thus the high frequency roll off of the compensator (*C*) is the key to reducing sensor noise affecting the controller output signal.

Figure 47 shows the noise amplification at the controller output for both design 1 and design 3 when there is a white noise source.

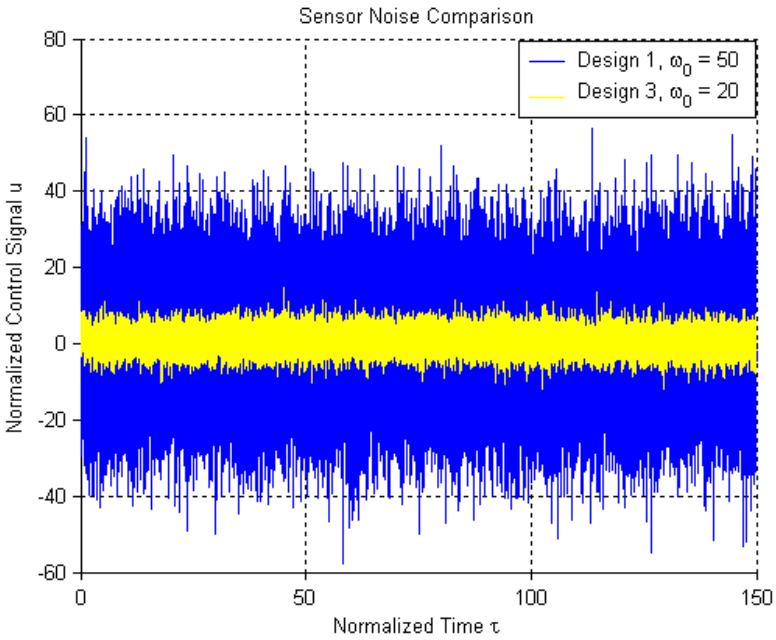

Figure 47: Control Signals of Design 1 and Design 3

Figure 47 shows the effects of white noise, added at the measured output, on the control signals. From the figure, we can see that there will be a good chance that design 1 would saturate the input of the plant. However, design 3 is less susceptible to the white noise source than design 1.

Figure 48 shows the Bode diagrams of the transfer functions from the sensor noise input to the control signal for six sets of the operating points of the electrostatic actuator. The classic ADRC controller from design 1 is used to create these plots. We can see from Figure 48 that all the plants, with the exception of *P33*, suffer from low frequency noise amplification. The *P33* plant, which represents the electrostatic actuator

at pull-in, has a pole at the origin (type-1 system) and thus has high plant gain at low frequencies.

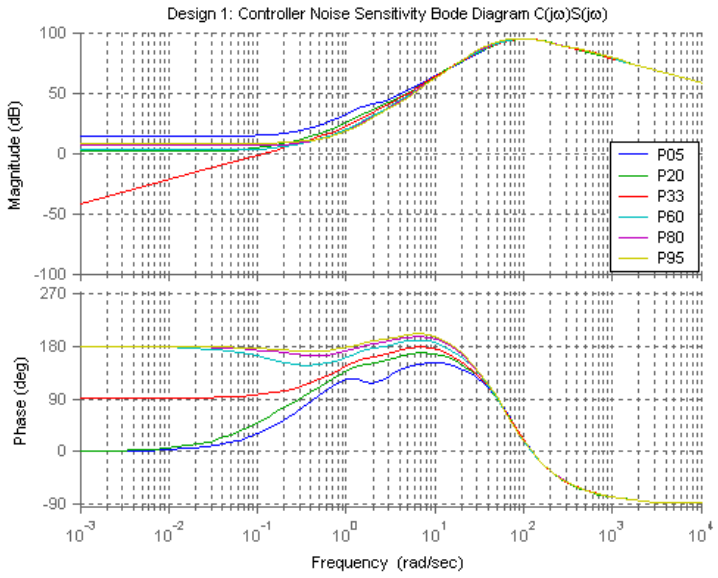

Figure 48: Bode Diagrams of the Controller Noise Sensitivity Transfer Functions (*C(s)S(s)*) for Multiple Equilibrium Points (Design 1)

While the low input gain of the electrostatic actuator is detrimental to noise attenuation, it does have its benefits when disturbance rejection is considered. Figure 49 shows the Bode diagrams of the input disturbance attenuation transfer function *P(s)S(s)* along with the actuator model, the inverse of the controller and the loop transmission function *L(s)*. The classic ADRC controller from design 1 is used to create these plots. In Figure 49, we can see at low frequencies where the magnitude of *L(s)* is large, *P(s)S(s)* (2.88) behaves like C^{-1}, while at high frequencies, where the magnitude of *L(s)* is small, it behaves like *P*. Thus if *C* has high gain at low frequencies (due to integral action), C^{-1} will attenuate low frequency disturbances. It is also interesting to note that when the

magnitude of *L(s)* is small, our controller has no control over high frequency disturbance rejection; disturbance rejection will follow the high frequency behavior of the plant.

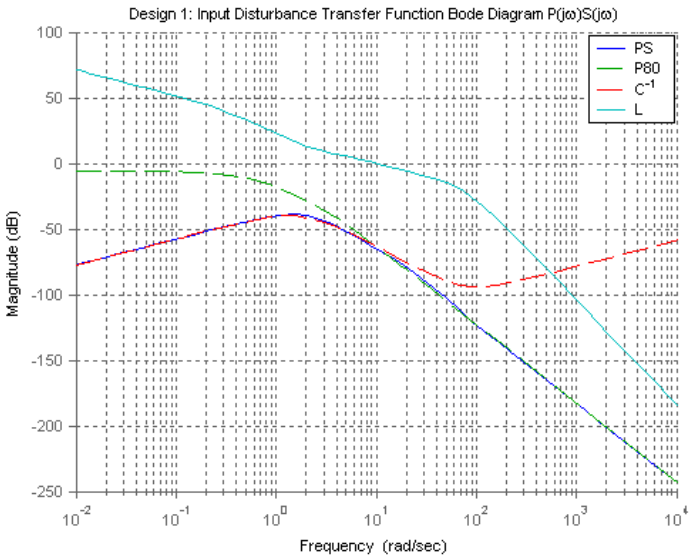

Figure 49: Bode Diagrams of Input Disturbance Transfer Function (*P(s)S(s)*), Actuator Model, the Inverse of the Controller, and Loop Transmission Function

From the analysis above, we can see that design 3 is clearly superior to design 1 when sensor noise is considered. Next, we will compare the classic LADRC (design 3) with the alternative ADRC design.

4.3.1.2 Comparison between Alternative and Classic ADRCs

In this subsection, design 3 of Section 4.1 will be compared with the alternative ADRC design of Section 4.2. The controller and observer parameters for both designs are identical. The controller bandwidth is set to 2 rad/s and the observer bandwidth is set at 20 rad/s.

The controller for the alternate ADRC design is given in (4.63).

$$C(s)=\frac{347{,}149(s+3.455)(s^2+2.432s+1.642)}{s(s+45.2)(s^2+40.8s+1048)} \tag{4.63}$$

Figures 39, 40 and 41 in Section 4.2 have shown some comparison results between classic ADRC (design 3) and alternative ADRC designs (including Bode diagrams of the transfer functions between input disturbance and position outputs, step responses, and Bode diagrams of the controller transfer functions for these two designs). Figure 50 shows the noise amplification of the two designs at the controller outputs (seen at the plant input).

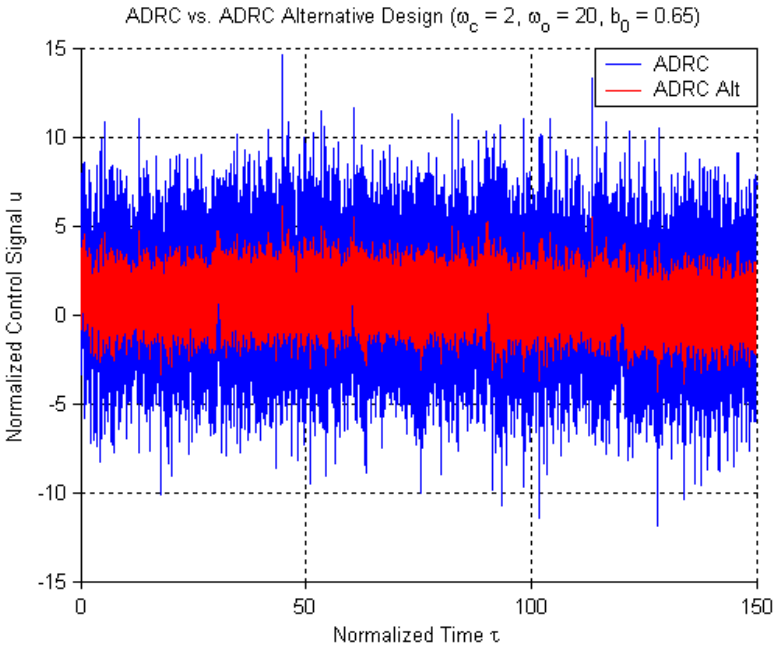

Figure 50: Noise Amplification at the Controller Outputs of Classic ADRC and Alternative ADRC Designs

We can see from Figure 50 that the alternative ADRC design provides a better compromise between performance and noise reduction than the classic ADRC design.

The amplitude of the alternative ADRC control signal is much smaller than the one of the Classic ADRC design in the presence of noise.

In the next section, multi-loop control will be introduced to provide another design strategy to control the electrostatic actuator.

4.4 Multi-loop Control

This section will introduce a special single-input-multiple-output (SIMO) control strategy for the electrostatic actuator. It will demonstrate that when one has access to extra measurements of the variables of the actuator, the effects of sensor noise and disturbances can be greatly reduced in the actuator system.

4.4.1 Transfer Function Derivation

As stated in Chapter 2, in the electrostatic actuator, there is an internal positive feedback mechanism that causes the system to become unstable at displacements greater than 1/3 of the full gap. In this section we suppose the electrostatic actuator can be divided into two sub-plants, which are P_1 and P_2, along with a positive feedback coupling constant K. The two sub-plants along with the feedback constant, which were shown in Chapter 2 (Figure 16), are explicitly defined in (4.64), (4.65) and (4.66).

$$P_1 = \frac{2Q_{eq}}{3\left(s^2 + 4s + 1\right)} \tag{4.64}$$

In (4.64), the variable Q_{eq} is the equilibrium charge of the electrostatic actuator

$$P_2 = \frac{2/(3r_n)}{s + (1/r_n)(1 - X_{eq})} \tag{4.65}$$

In (4.65), the normalized resistance $r_n = 0.95$ and the variable X_{eq} is the equilibrium displacement of the electrostatic actuator.

$$K = \frac{3}{2} Q_{eq} \tag{4.66}$$

The output of the first sub-plant (P_1) is the displacement *x*. The output of the second sub-plant (P_2) is the charge *q*. The two sub-plants of the electrostatic actuator and the two controllers ($C_1(s)$ and $C_2(s)$) which are used to control the two sub-plants are shown in Figure 51, where the positive gain *K* (4.66) constitutes the positive feedback path. The prefilter $F(s)$ and controller $C_2(s)$ constitute a 2-DOF control law of the ADRC.

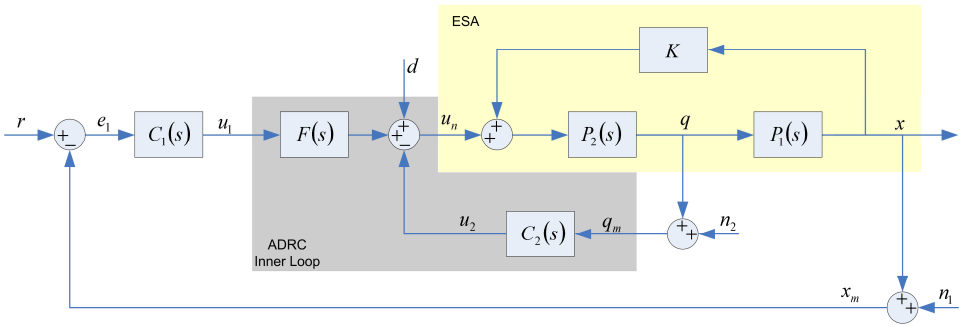

Figure 51: Electrostatic Actuator Multi-loop Control Architecture

In Figure 51, the displacement *x* is the primary process variable to be controlled by a Proportional Integral (PI) controller ($C_1(s)$). The reference signal *r* is the set-point

for this displacement. The secondary process variable q (charge) is the output of the sub-plant P_2 and is used as a control signal for the sub-plant P_1. It is assumed both q and x are measurable. These measurable signals along with the sensor noises (n_1 and n_2) are fed back to their respective controllers ($C_1(s)$ and $C_2(s)$). The control strategy shown in Figure 51 is denoted as multi-loop control, which consists of an inner loop controlled by an ADRC and an outer loop controlled by the PI controller.

Please also note that there is an input disturbance, d, acting on the system. This disturbance term represents internal and external disturbances, which include any couplings between the two sub-plants. Figure 52 shows an equivalent description of the model shown in Figure 51, where $P(s) = P_1(s)P_2(s)$.

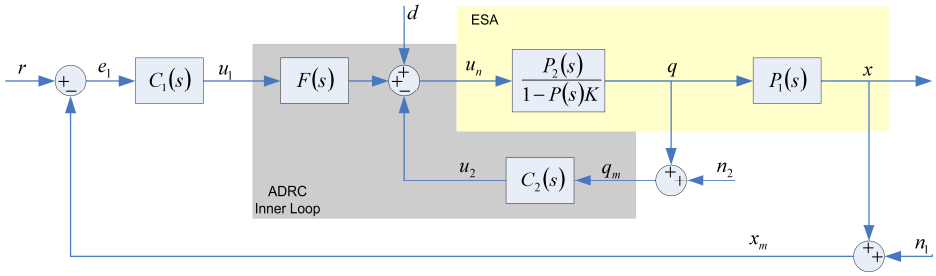

Figure 52: Simplified Block Diagram of Multi-loop Control System

In Figure 52, the transfer function representation of the displacement, x is given by (4.67).

$$x = \frac{1}{1 + P_2C_2 + PFC_1 - PK}\left(PFC_1r + Pd - PFC_1n_1 - PC_2n_2\right) \tag{4.67}$$

The transfer function representation of the charge output q is given by (4.68).

$$q = \frac{1}{1 + P_2C_2 + PFC_1 - PK}\left(P_2FC_1r + P_2d - P_2FC_1n_1 - P_2C_2n_2\right) \tag{4.68}$$

The effects of sensor noise at the control input (u_n) to the plant are represented by (4.69).

$$u_n = -\frac{FC_1(1-PK)}{1+P_2C_2+PFC_1-PK}n_1 - \frac{C_2(1-PK)}{1+P_2C_2+PFC_1-PK}n_2 \tag{4.69}$$

The loop transmission function (L_1), for the primary (outer) loop, is given in (4.70).

$$L_1 = \frac{PC_1F}{1+P_2(C_2-KP_1)} \tag{4.70}$$

The complementary sensitivity function T_1 for the outer loop is given in (4.71).

$$T_1 = \frac{L_1}{1+L_1} \tag{4.71}$$

The complementary sensitivity function T_1 can also be written as (4.72).

$$T_1 = \frac{L_1}{1+L_1} = \frac{PC_1F}{1+L_2} \tag{4.72}$$

In (4.72), L_2 is defined as the loop transmission function of inner loop. It is given as below.

$$L_2 = P_2C_2 + PFC_1 - PK \tag{4.73}$$

Equation (4.72) can be written as (4.74).

$$T_1 = \frac{PC_1F}{1+P_2C_2+PC_1F-PK} \tag{4.74}$$

The sensitivity function for the outer loop is given in (4.75).

$$S_1 = \frac{1}{1+L_1} \tag{4.75}$$

Substituting (4.70) into (4.74), we will have the sensitivity function rewritten as (4.76).

$$S_1 = \frac{1 + P_2 C_2 - PK}{1 + P_2 C_2 + PC_1 F - PK} \tag{4.76}$$

4.4.2 Linear Controller Design

This section will derive the controllers for the primary (outer) loop and the secondary (inner) loop. The secondary loop utilizes an ADRC (C_2), while the primary loop utilizes a PI controller (C_1).

4.4.2.1 Secondary Loop Design

The secondary (inner) loop for the electrostatic actuator model is a first order system. In this design, the filtered estimate of the position is used in the control law of the ADRC instead of the actual measured signal. The ADRC controller with a 2nd order ESO will be applied in the inner loop.

The transfer function representation of the estimated displacement is given in (4.77).

$$Z_1(s) = \frac{2\omega_o s + \omega_o^2}{(s+\omega_o)^2} Y(s) + \frac{s}{(s+\omega_o)^2} U(s) \tag{4.77}$$

The disturbance estimate is given in (4.78).

$$Z_2(s) = \frac{\omega_o^2 s}{(s+\omega_o)^2} Y(s) - \frac{\omega_o^2}{(s+\omega_o)^2} U(s) \tag{4.78}$$

The control law used to control and decouple the plant is given in (4.79).

$$U(s)=\frac{1}{\hat{b}}\left[k_p(R(s)-Z_1(s))-Z_2(s)\right] \tag{4.79}$$

Equations (4.77) and (4.78) can be substituted into (4.79) to yield the transfer functions for the controller and the prefilter as shown in (4.80).

$$U(s)=\frac{1}{\hat{b}}\left[\frac{k_p(s+\omega_o)^2}{s(s+2\omega_o+k_p)}R(s)-\frac{(2\omega_o k_p+\omega_o^2)s+k_p\omega_o^2}{s(s+2\omega_o+k_p)}Y(s)\right] \tag{4.80}$$

From (4.80), the controller in the feedback path is given in (4.81).

$$C_2(s)=\frac{1}{\hat{b}}\cdot\frac{(2\omega_o k_p+\omega_o^2)s+k_p\omega_o^2}{s(s+2\omega_o+k_p)} \tag{4.81}$$

The controller in (4.81) is a strictly proper controller with integral action. From (4.80), the prefilter is given in (4.82).

$$F(s)=\frac{1}{\hat{b}}\cdot\frac{k_p(s+\omega_o)^2}{s(s+2\omega_o+k_p)} \tag{4.82}$$

The ADRC controller parameters for the secondary loop are given in (4.83).

$$\omega_c=2 \quad \omega_o=20 \quad \hat{b}=0.7018 \tag{4.83}$$

The secondary loop plant transfer function (P_2) is given in (4.65).

4.4.2.2 Primary Loop

The primary (outer) loop utilizes a strictly proper PI controller that includes a first order noise filter. This controller is defined in (4.84), where K_{P1} is the proportional gain, K_I is the integral gain and ω_f is the cut-off frequency of the noise filter.

$$C_1 = \underbrace{\frac{K_{P1}s + K_I}{s}}_{PI} \cdot \underbrace{\frac{\omega_f}{s+\omega_f}}_{Noise\ Filter} \tag{4.84}$$

The PI controller values that were chosen for this design are given in (4.85).

$$\begin{aligned} K_{P1} &= 2.75 \\ K_I &= 0.75 \\ \omega_f &= 100 \end{aligned} \tag{4.85}$$

The primary (outer) loop plant transfer function is given in (4.64). The positive feedback constant *K* in Figure 51 is given in (4.66).

4.4.3 Controller Analysis

In the following plots, unless otherwise noted, the actuator model used in the simulations is linearized around the displacement of 90% of the full gap. Then the plant transfer function for the primary (outer) loop is given in (4.86).

$$P_1 = \frac{1.095}{s^2 + 4s + 1} \tag{4.86}$$

The plant transfer function for the secondary (inner) loop is given in (4.87).

$$P_2 = \frac{0.7018}{s + 0.1053} \tag{4.87}$$

The positive feedback coupling constant is given in (4.88).

$$K = 2.4648 \tag{4.88}$$

The Bode diagram of the primary loop transmission function (given by (4.70)) is shown in Figure 53.

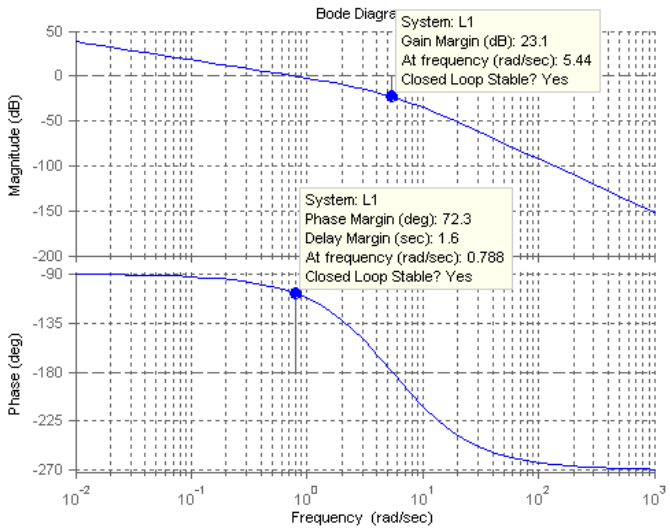

Figure 53: Bode Plot of Primary Loop (*L1*) Transfer Function

From Figure 53, we can see that the gain margin is 23.1 dB and the phase margin is 72.3°. So the system is stable with sufficient stability margins. The bandwidth of the primary (outer) loop is 1.1 rad/s. This outer loop mainly deals with gain variations of the plant. The secondary (inner) loop handles the pole uncertainty. The Bode plot of the loop transmission function for the secondary (inner) loop represented by (4.73) is shown in Figure 54.

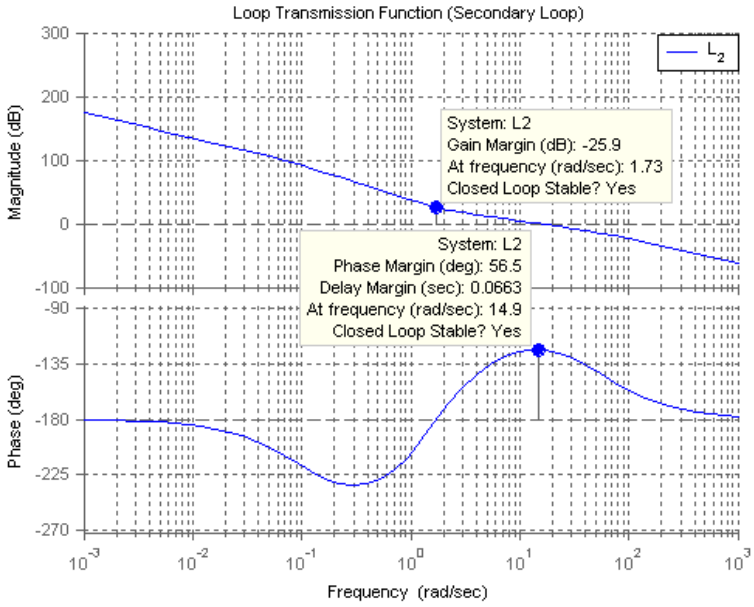

Figure 54: Bode Plot of Secondary Loop Transmission Function (*L2*)

From Figure 54, the gain margin is -25.9 dB and the phase margin is 56.5°. The bandwidth of this inner loop is 20 rad/s. The bandwidth is sufficiently fast to function like a lowpass filter to the primary (outer) loop.

Next, the step responses for the multi-loop control system will be investigated. Figure 55 shows the step responses for the linearized actuator models around the displacements of 10% (*P10*), 33% (*P33*), 50% (*P50*), 70% (*P70*) and 90% (*P90*) of the full gap. From Figure 55 one can see that the low loop gain of the *P10* model causes it to suffer from a long rise time. Thus the step response for *P10* is the slowest one compared with the other step responses.

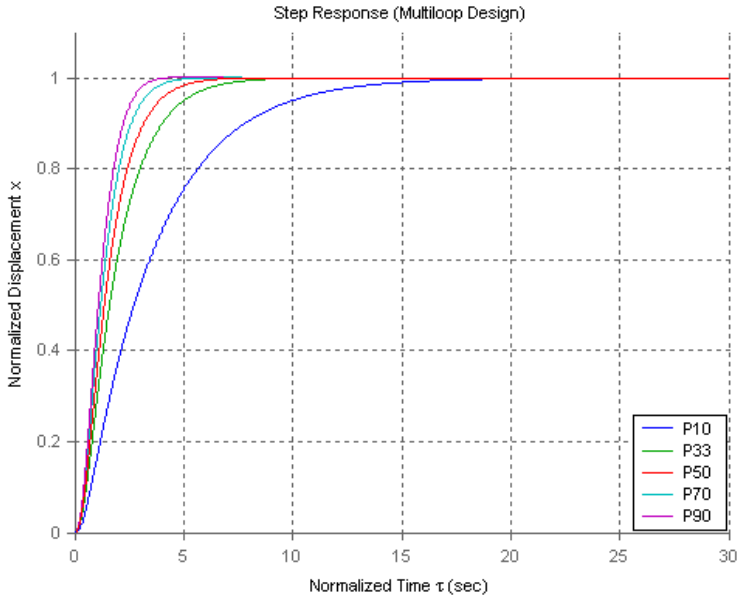

Figure 55: Step Responses of the Multi-loop Controlled Actuator System

The transfer functions from the noise sources (n_1 and n_2) to the controller outputs are given by (4.69). The Bode plots of these two transfer functions along with the Bode plot of the transfer function (2.86) for an earlier ADRC design (design 1) are shown for comparison in Figure 56. From Figure 56, we can see that the multi-loop control design offers significant advantages in noise attenuation over the classic ADRC design.

The Bode magnitude plot in Figure 57 shows the same information as in Figure 56 only except that the multi-loop control does not include noise filter (4.82) in Figure 57. Excluding the noise filter from the multi-loop control results in excessive sensor noise amplification. Thus the use of the noise filter is the preferred design.

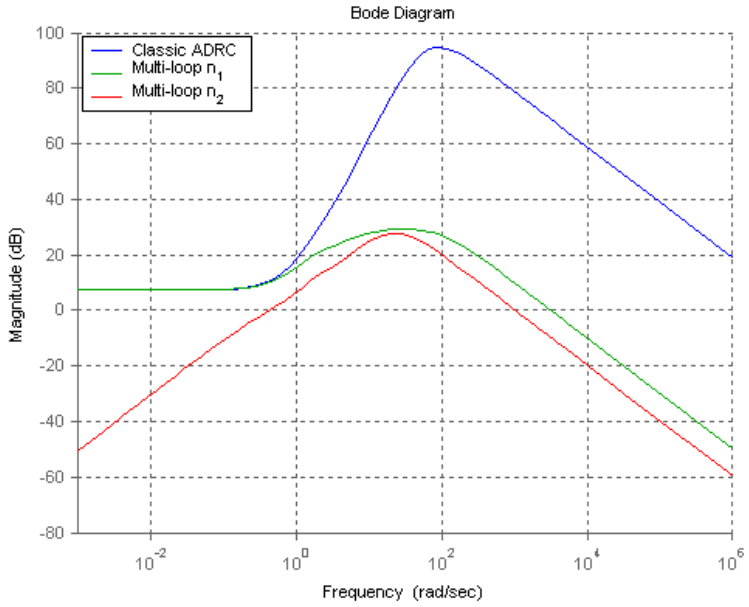

Figure 56: Magnitude Frequency Responses of Controller Noise Transfer Functions for Both Multi-loop (with noise filter) and Classic ADRC Designs

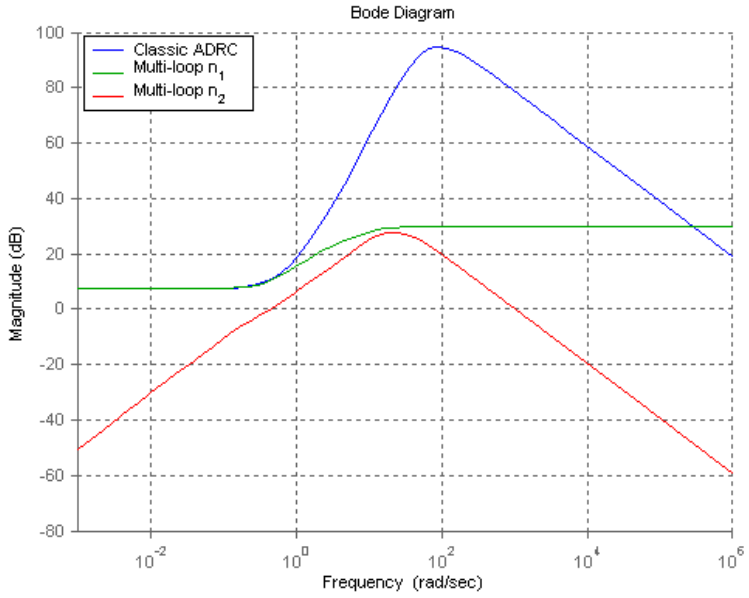

Figure 57: Magnitude Frequency Responses of Controller Noise Transfer Functions for Both Multi-loop (without noise filter) and Classic ADRC Designs

Equation (4.89) describes the effect of the input disturbances on the measured output *x*.

$$x = \frac{P}{1 + P_2 C_2 + P C_1 F - P K} d \tag{4.89}$$

Substituting (4.73) into (4.89), we can rewrite (4.89) as in (4.90).

$$x = \frac{P}{1 + L_2} d \tag{4.90}$$

From (4.90) $P/(1+L_2)$ is the input disturbance transfer function (*P(s)S(s)*). The Bode plot of the transfer function is shown in Figure 58.

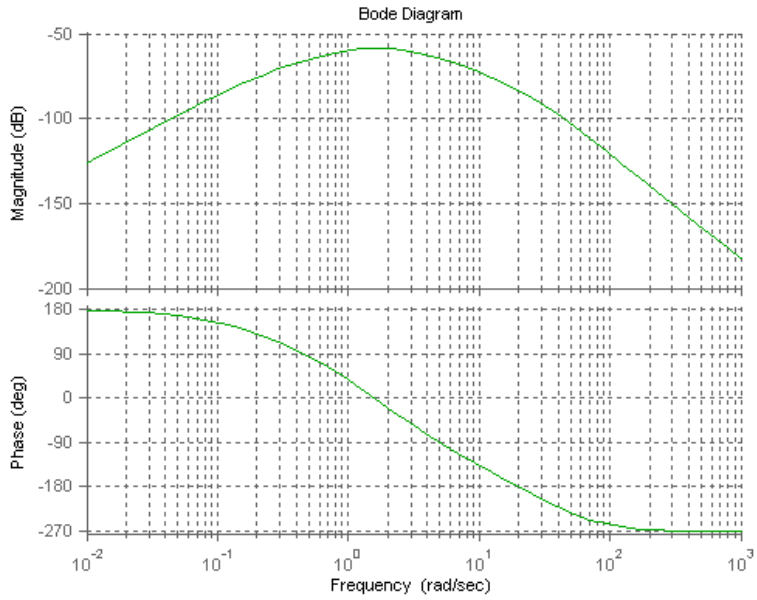

Figure 58: Bode Diagram of Input Disturbance Transfer Function

Figure 58 shows exceptional input disturbance rejection over the entire frequency range. Figure 59 shows how the input disturbance transfer function (*P(s)S(s)*) is affected by the plant and controller.

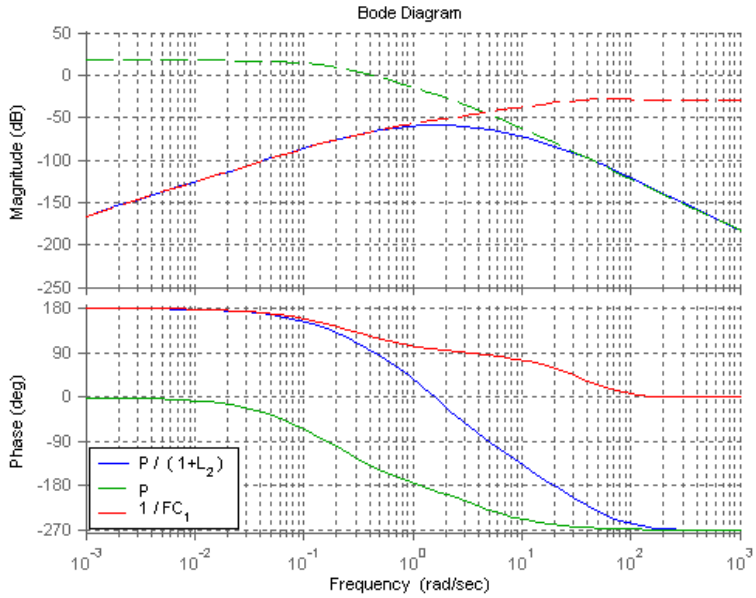

Figure 59: Bode Diagrams of Input Disturbance Transfer Function, Actuator Model, and Inverse of $F(s)C_1(s)$

In Figure 59, we can see that the inverse of $F(s)C_1(s)(FC_1)$ plays a dominant role in input disturbance rejection when the magnitude of $F(j\omega)C_1(j\omega)$ is large at low frequency. When the magnitude of $F(j\omega)C_1(j\omega)$ small (at high frequencies) the disturbance rejection is solely dependent on the plant. The electrostatic actuator has excellent built in disturbance rejection capabilities due to its low system gain.

The classic ADRC design eases the burden on the control system designer by requiring less modeling information than the alternative ADRC design. While the classic ADRC only requires one sensor to measure the position output information, the multi-loop design needs two sensors to measure both charge and position outputs. However, the benefit of demanding less modeling information for the classic ADRC requires that a

high DC gain be used which results in increased noise sensitivity when compared with the other two designs (alternative ADRC and multi-loop control design).

The alternative ADRC design requires the partial modeling information and uses this information to reduce the need for high controller gains. This makes the alternative ADRC controller slightly less susceptible to sensor noise compared to the classic ADRC design while still maintaining the ease of implementation of a single loop design.

The multi-loop controller does not require any additional modeling information compared to the classic ADRC design, but it does need an additional sensor to provide a charge feedback loop. The combination of an ADRC in the charge loop and a PI controller in the position loop allows the use of a low gain/bandwidth control scheme that offers good performance with reduced sensitivity to sensor noise.

CHAPTER V

SIMULATION RESULTS

In this chapter, the classic ADRC, alternate ADRC, and the multi-loop control system designs are applied to the normalized nonlinear electrostatic actuator model. The tracking performance of these controllers is compared utilizing the ISE (Integrals of the Squared Errors).

5.1 Classic ADRC Simulation Results

The normalized nonlinear model of the electrostatic actuator given below will be used for the simulations that follow.

$$\begin{aligned} \ddot{x} + 2\zeta\dot{x} + x &= \frac{1}{3}q^2 \\ \dot{q} + \frac{1}{r}(1-x)q &= \frac{2}{3r}v_s \end{aligned} \tag{5.1}$$

It is important to note that since (5.1) is a normalized model the units of time are scaled along with the displacement, charge and control signal. The equations that govern the normalization are given in (2.35) and (2.36). The sensor noise source used in these simulations is given in Figure 60.

The first simulation compares the tracking performances of the three classic LADRC designs with different sets of tuning parameters introduced in Section 4.1. In this simulation, the electrostatic actuator is commanded to track several desired travel ranges which are set to 10%, 30%, 50%, 70% and 90% of the full gap. The simulation results for the three LADRC designs are shown in Figure 61. In Figure 61, all of the three designs have shown acceptable tracking performances. Figure 62 investigates the displacement responses of the three LADRC designs at 10% of the full gap in greater detail.

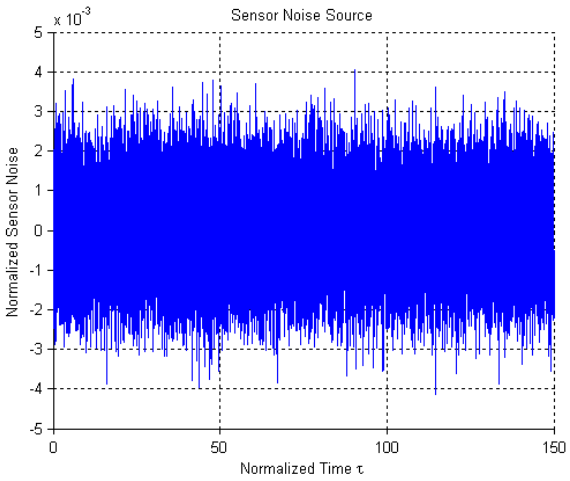

Figure 60: Sensor Noise

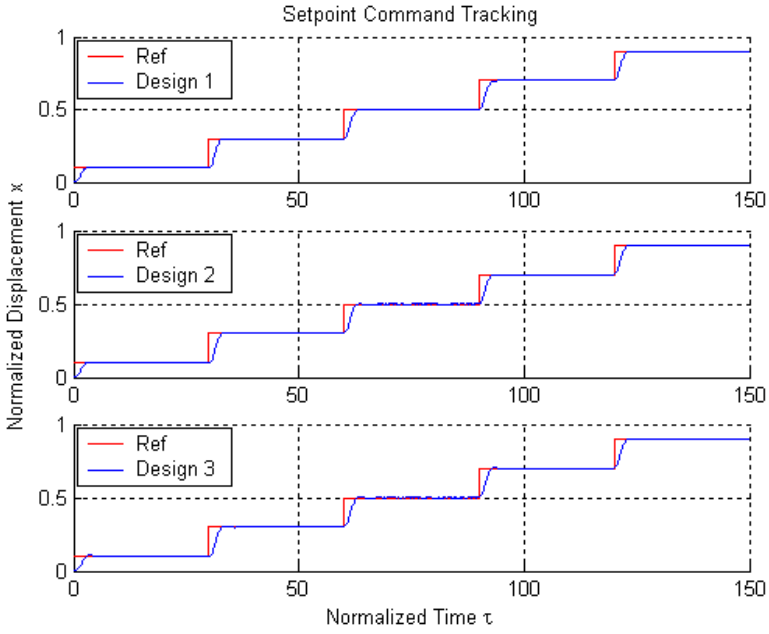

Figure 61: Displacement Outputs of Three Classic ADRC Designs

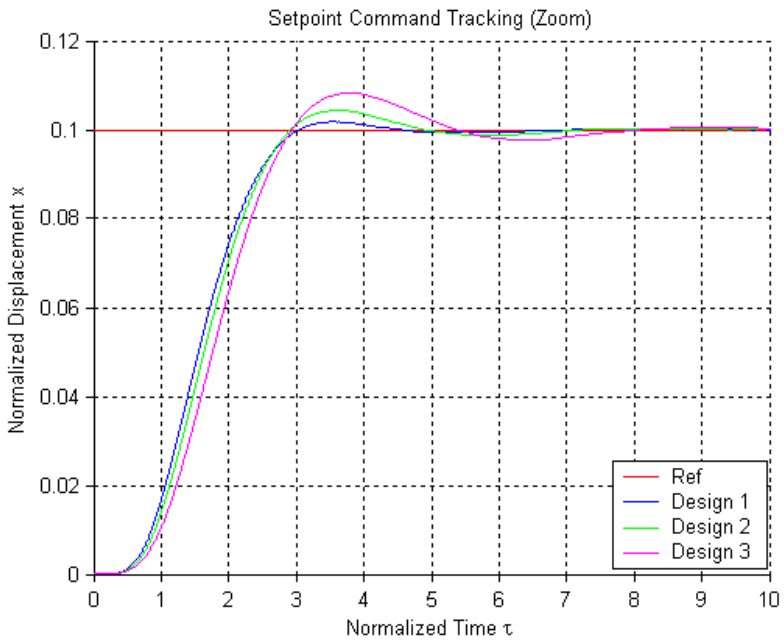

Figure 62: Displacement Responses of Three LADRC Designs at 10% of the Full Gap

From Figure 62, we can see that the first design, which has the highest observer bandwidth, performs the best with almost no overshoot. Designs 2 and design 3 perform well with a noticeable amount of overshoot, where design 2 has an overshoot of 4.8% and design 3 has an overshoot of 8.3%. For an electrostatic actuator, reasonable overshoot at small displacements is acceptable. However, the overshoot at large displacements is much more troubling since it may cause the two plates of the electrostatic actuator to crash into each other. The integrals of the squared errors (ISE) for the three LADRC designs as the desired travel range is set to 10% of the full gap are given in Table XIV.

TABLE XIV: ISES FOR THREE LADRC DESIGNS AT 10% OF FULL GAP

ISE		
Design 1	*Design 2*	*Design 3*
0.0127	0.0133	0.0144

From Table XIV, design 1 has the best tracking performance. The responses of the actuator to a desired traveling range of 90% of the full gap for the three designs (classic LADRC with three different sets of tuning parameters) are shown in Figure 63.

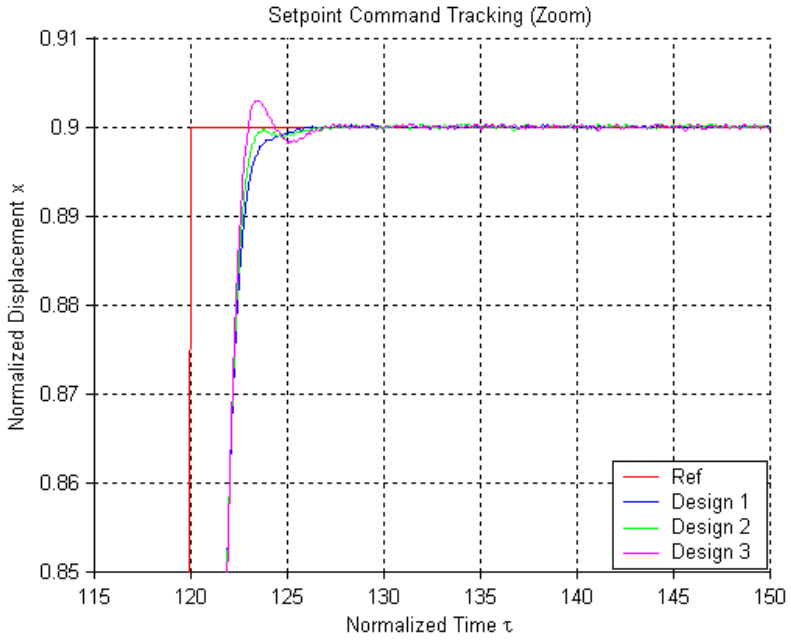

Figure 63: Displacement Responses of Three LADRC Designs at 90% of the Full Gap

In Figure 63, design 3 exhibits the largest overshoot percentage (2.2%). So it shows the worst tracking performance among the three designs. This is because design 3 has the smallest observer bandwidth. The effects of sensor noise on the outputs of these

three designs are too small to tell in the figure. The ISE for the three LADRC designs when the desired traveling range is chosen as 90% of the full gap are shown in Table XV.

TABLE XV: ISES FOR THREE LADRC DESIGNS AT 90% FULL GAP

ISE		
Design 1	*Design 2*	*Design 3*
0.8914	0.9074	0.9347

From Table XV, we can see that design 1 has the least tracking error among the three designs. Figure 64 shows the sensitivities of the control signals of the three classic ADRC designs (shown in Figure 60) to the sensor noise along with the equivalent control signals without sensor noise.

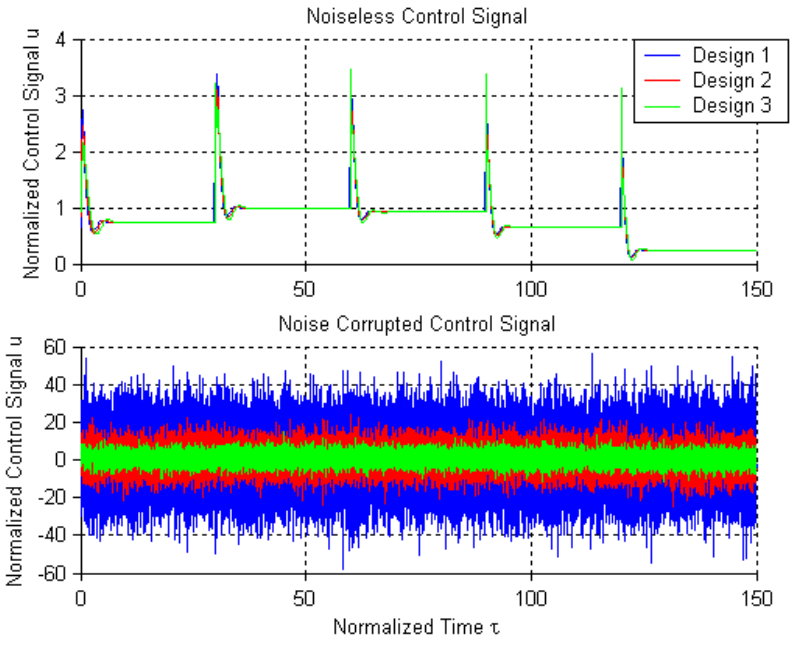

Figure 64: Controller Noise Sensitivities for Three Classic ADRC Designs

From Figure 64, we can see that these three designs are highly susceptible to sensor noise. Design 1 is completely unacceptable due to a very noisy control signal. Design 2 performs better but is still problematic. Compared to the first two designs, design 3 is the least susceptible to the sensor noise, and can be considered for application in the real world. A close look at the control signal with sensor noise (noisy signal) of design 3, along with its noiseless equivalent signal (clean signal) is shown in Figure 65.

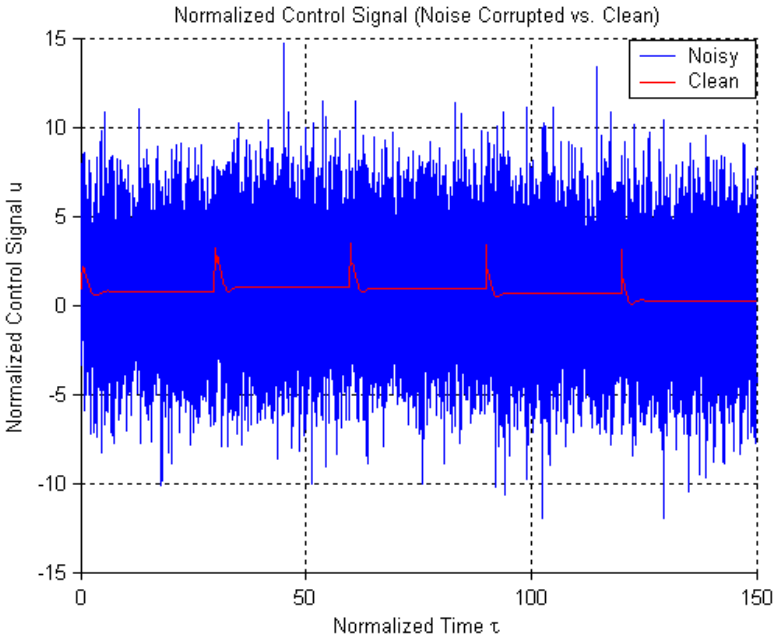

Figure 65: Clean and Noisy Control Signals of Design 3

From Figure 65 we can see that the control signal is highly affected by the noise source. The majority of the noise shown in Figure 65 is outside the bandwidth of the plant. In practice, the actuator itself is a very good low pass filter. In Chapter 2, Figure 16 shows how the actuator can be separated into an electrical sub-plant and a mechanical sub-plant. It also shows that the charge output of the electrical sub-plant can be viewed as a control signal for the mechanical sub-plant. The sensor noise at the input to the

electrical portion of the plant is only a concern if it approaches the saturation level of the drive electronics. However, excessive noise at the mechanical portion of the plant can lead to excessive wear on the electrostatic actuator. The electrical charge acting as the control signal to the mechanical portion of the plant is shown in Figure 66. We can see for Figure 66 that the electrical sub-plant filtered out the majority of the high frequency noise. This control signal shows the steps in charge needed to track the displacement commands at 10%, 30%, 50%, 70%, and 90% of full gap respectively.

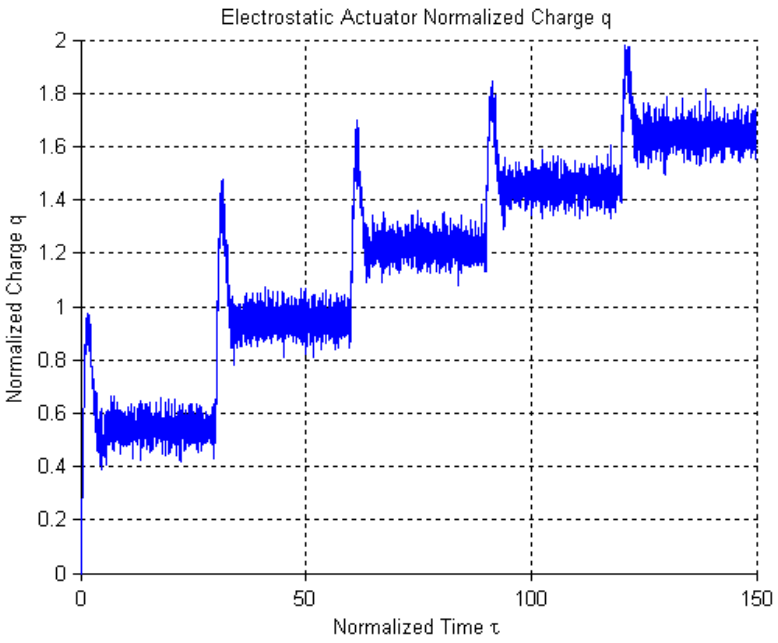

Figure 66: Actuator Charge Control Signal

In the following simulation results, the responses of the three classic ADRC designs to a reference input of 97% of the full gap will be investigated. We add a step input disturbance with a magnitude of 0.5 to the input of the actuator at $t = 15$ seconds. The displacement output in the presence of the input disturbance is shown in Figure 67.

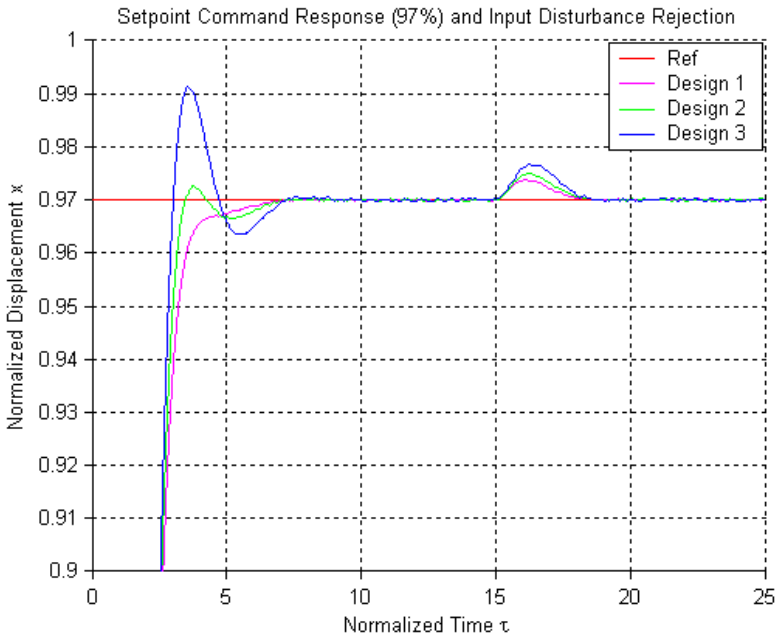

Figure 67: Displacement Outputs of the Actuator for Three Classic ADRC Designs in the Presence of Step Input Disturbance

From Figure 67 we can see all of three designs can accommodate a travel range of 97% of the full gap with small overshoots at the disturbance. Therefore it can be said that the classic ADRC design can achieve a maximum gap traversal of approximately 97% of the full gap in the presence of input disturbances.

Given the previous simulation results, design 3 is the only viable option for the classic ADRC strategy due to its excellent noise attenuation effects.

5.2 Alternative ADRC Simulation Results

In this section the alternate ADRC represented by (4.47) and (4.48) are applied to the nonlinear actuator model given by (5.1). The set-points were chosen as 10%, 30%, 50%, 70% and 90% of the full gap. The displacement outputs for both the classic ADRC design (design 3) and the alternate ADRC design are shown in Figure 68.

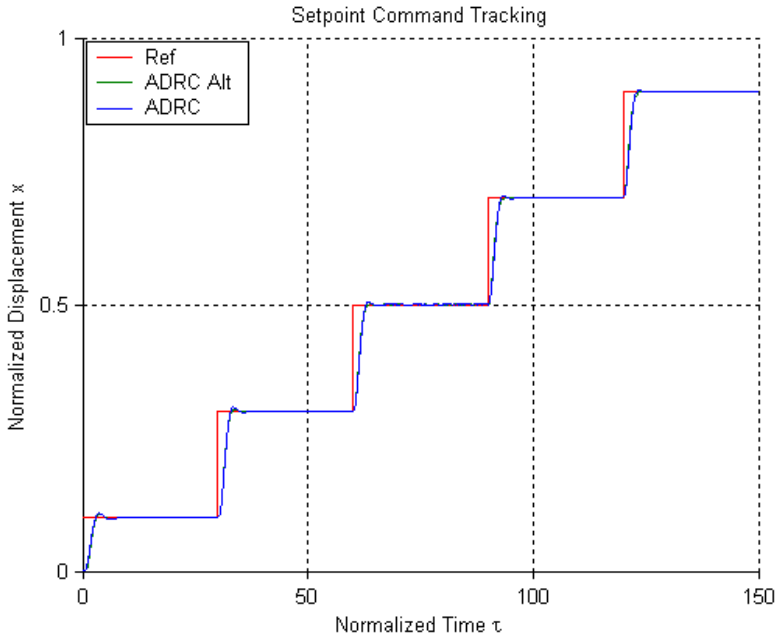

Figure 68: Set-points Tracking for Classic ADRC and Alternative ADRC Designs

It is seen from Figure 68 that the alternative ADRC design matches well with the classic ADRC design. Both designs utilize an observer bandwidth of $\omega_o = 20$ *rad/s*, a plant gain estimate $\hat{b} = 0.65$, and a desired closed loop plant of $8/(s+2)^3$, which results in controller gains of

$$K_1 = 8$$
$$K_2 = 8.335 \tag{5.2}$$
$$K_3 = 1.4063$$

The nominal plant for the alternative ADRC design was chosen as

$$P_n(s) = \frac{\hat{b}}{s(s+a_1)(s+a_2)} = \frac{0.65}{s(s+1.0276)(s+3.5661)}. \tag{5.3}$$

The nominal plant for the classic ADRC design is a third order integrator.

The step responses for these two designs at small displacements are demonstrated in Figure 69, where the step responses are at 10% of the full gap.

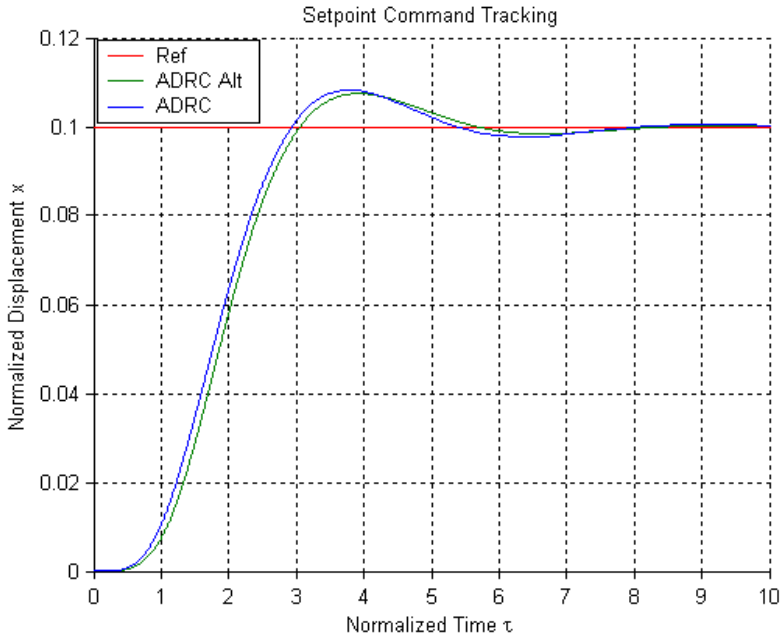

Figure 69: Displacement Outputs for Both Classic and Alternative ADRC Designs at 10% of Full Gap

From Figure 69 we can see that the classic ADRC design exhibits 8.3% overshoot, while the alternate ADRC design has 7.5% overshoot. As stated before, the

overshoot at small displacements is deemed acceptable. However, it would be much more serious at large displacements where the plates of the actuator could come into contact with each other.

In the next simulation, a step response at large displacement will be discussed. The set-point is chosen as 90% of the full gap. The displacement outputs (or step responses) of the classic ADRC (design 3) and alternative ADRC are displayed in Figure 70. From the figure, we can see that the classic ADRC design has a larger overshoot percentage (2.23%) than the alternate ADRC (almost zero).

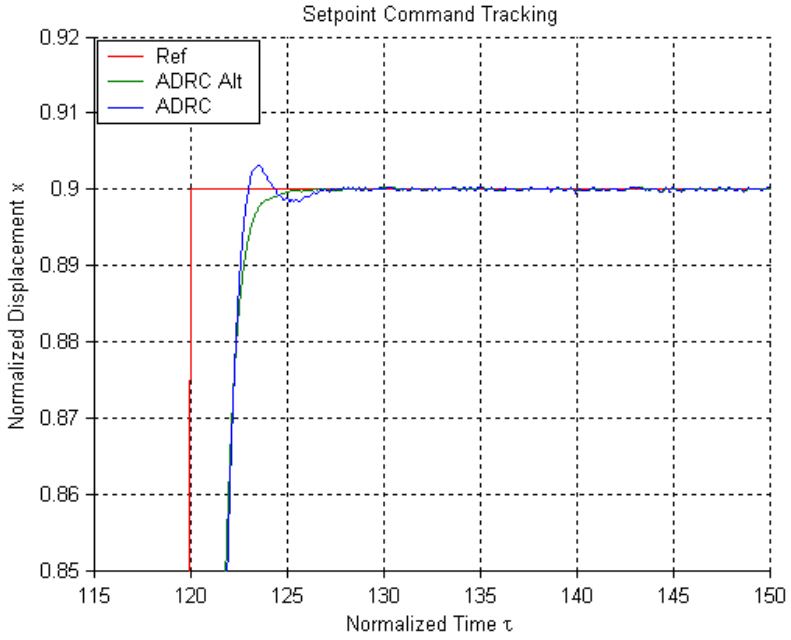

Figure 70: Step Responses for the Alternate and Classic ADRCs at 90% of Full Gap

The ISEs of the classic ADRC and the alternative ADRC designs at 90% of full gap are shown in Table XVI. From the table, we can see that the tracking performance of the classic ADRC design is better at small displacement but worse at the larger

displacement compared to the alternative ADRC. This is attributable to the higher observer bandwidth of the classic ADRC than the alternative one.

TABLE XVI: ISE OF CLASSIC ADRC AND ALTERNATE ADRC DESIGNS

ISE		
Displacement	*ADRC*	*ADRC Alt*
0.10 of full gap	0.0144	0.0154
0.90 of full gap	0.9347	0.9113

The responses of the alternative ADRC and the classic ADRC to a reference of 99% of the full gap in the presence of a step disturbance with a magnitude of 0.5 at t = 15 time units are shown in Figure 71.

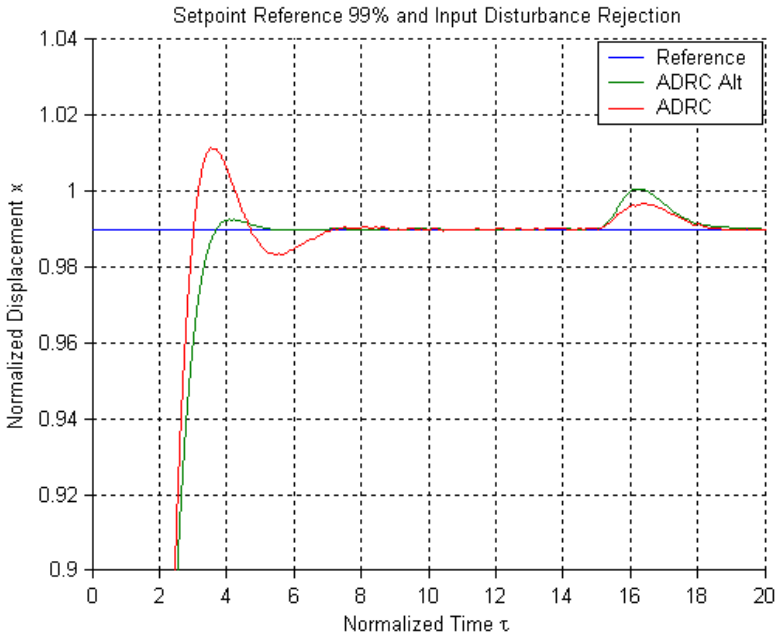

Figure 71: Displacement Outputs for Alternate and Classic ADRCs at 99% of Full Gap with Input Disturbance

From Figure 71, we can see that the alternative ADRC design shows much smaller overshoot percentage (0.25% at maximum) than the classic ADRC (2.25% at maximum). The large overshoot percentage of 2.25% for the classic ADRC controller could cause the upper and lower plates of the electrostatic actuator to crash into each other and therefore result in failure of operation in this design scenario. However, the disturbance rejection ability of the classic ADRC is a bit better than the alternative ADRC. Nevertheless the alternative ADRC design attenuates the disturbance just enough not to hit 100% gap traversal.

One significant advantage of the alternative ADRC design over the classic ADRC design is the attenuation of sensor noise. Figure 72 shows the control signals of both controller designs in the presence of sensor noise.

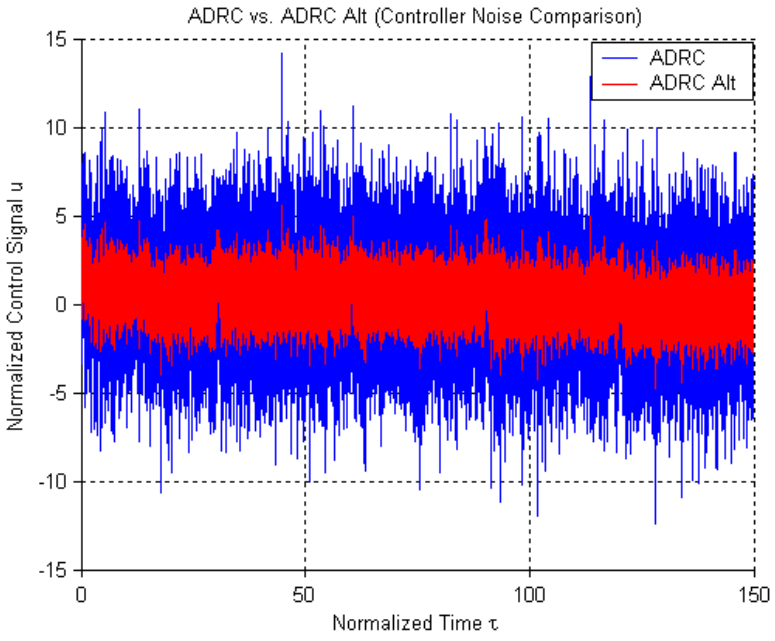

Figure 72: Control Signals of Classic and Alternate ADRCs in the Presence of Noise

From Figure 72, we can see that although the control signals for both cases are noisy, the alternative design is clearly less troublesome than the classic design. However the actuator plant in the classic design is a very good low pass filter so that the sensor noise at the electrical portion is not as much of a concern while reducing the sensor noise that reaches the mechanical portion is more important. The effective bandwidth of the controller must also be taken into consideration. The controller itself may be unable to pass the high frequency sensor noise. This is an implementation issue that was not covered in this thesis but is relevant to any sensor noise discussion.

The electrical charges acting as the control signals to the mechanical portion of the actuator plant for both alternative and classic ADRC designs are shown in Figure 73. The set-points were chosen as 10%, 30%, 50%, 70% and 90% of the full gap.

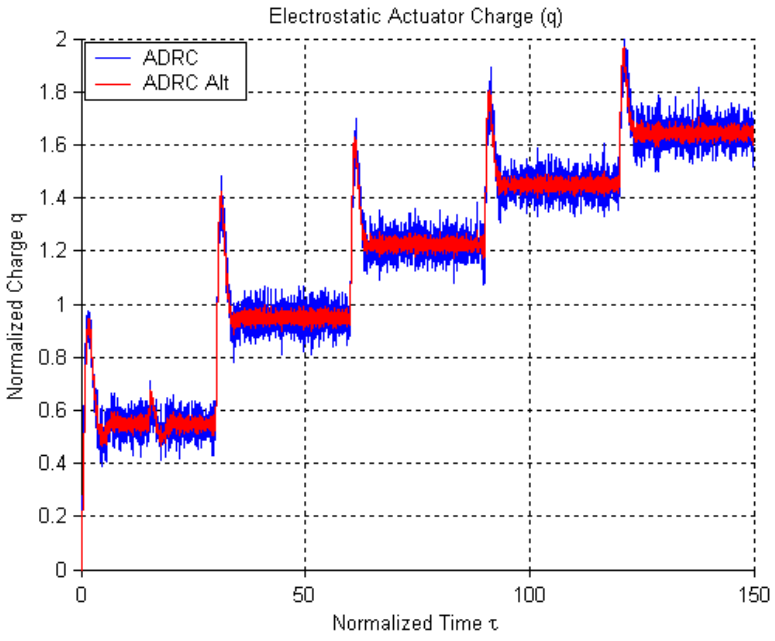

Figure 73: Charge Control Signals of Alternate and Classic ADRCs in the Presence of Sensor Noise

Figure 73 clearly shows how the control signals react to the commanded responses. After the filtering effect of the electrical portion of the actuator it is seen that the charge control input to the mechanical portion is acceptable in the alternate ADRC design while the classic ADRC design is still fairly noisy. It is important to note that this noise does not have a dramatic effect on the displacement output (*x)* for the classic ADRC.

5.3 Multi-loop Controller Simulation Results

The topology for the multi-loop controller design, which was previously shown in Figure 51, is repeated in Figure 74.

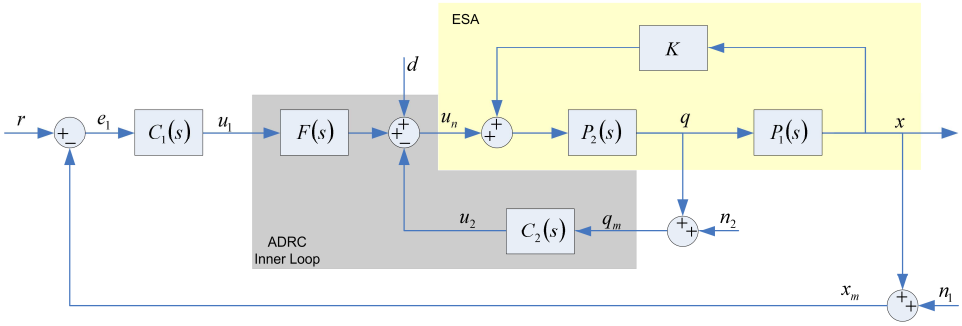

Figure 74: Configuration of Multi-loop Controller Design

The signals of interest in Figure 74 are the displacement *x*, the charge *q*, the control input u_n from ADRC, and the control signal u_1 from the PI controller. The PI controller is represented by the transfer function $C_1(s)$. The ADRC controller consists of the pre-filter $F(s)$ and the feedback controller $C_2(s)$.

In order to assess the performance of the multi-loop control structure, a series of step inputs of 10%, 30%, 50%, 70%, and 90% of the full gap were commanded. The displacement and the control signals of the PI controller and the composite control signal u_n are shown in Figure 75 without sensor noise. In the figure, the command response appears a little sluggish at 10% of the gap. The same simulation with sensor noise is shown in Figure 76. From Figure 76, we can see that the effect of sensor noise on the measured displacement output is almost unnoticeable. The composite control signal and the PI controller with the noise filter have acceptable levels of noise amplification.

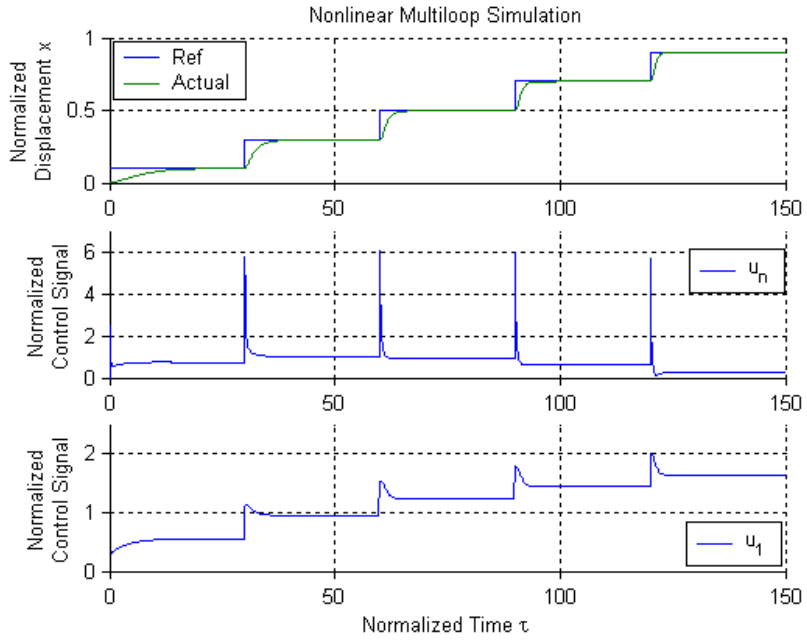

Figure 75: Control Signals and Displacement Output for Multi-loop Design without Sensor Noise

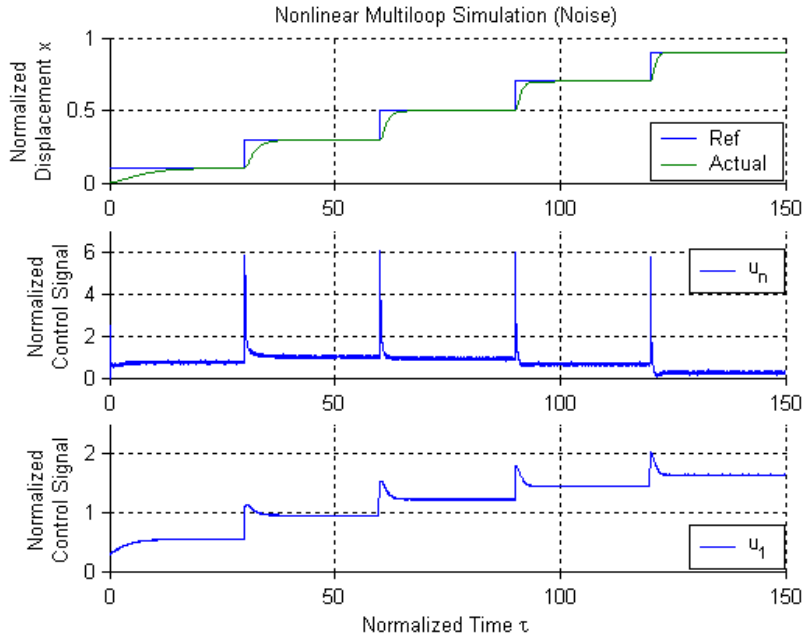

Figure 76: Control Signals and Displacement Output for Multi-loop Design in the Presence of Sensor Noise

A close-up view of the composite control signal u_n, for the two different implementations of the PI controller (ideal PI and the combination of PI with a 1st order low pass filter) is shown in Figure 77. Figure 77 clearly shows the benefits of the extra pole in the low pass filtered PI controller. The addition of the noise filter reduces the peaks of the control signal by more than one normalized voltage unit (*v*). There is also some noticeable attenuation at the steady state value of the control signal u_n.

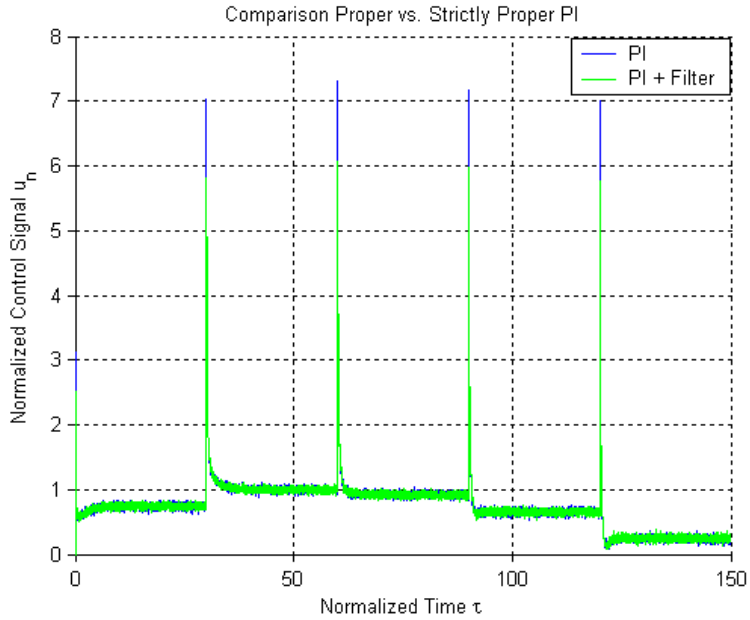

Figure 77: Control Signal u_n for Ideal PI and Noise Filtered PI Controllers

The response of this multi-loop control system to a command of 99% of the full gap is shown in Figure 78.

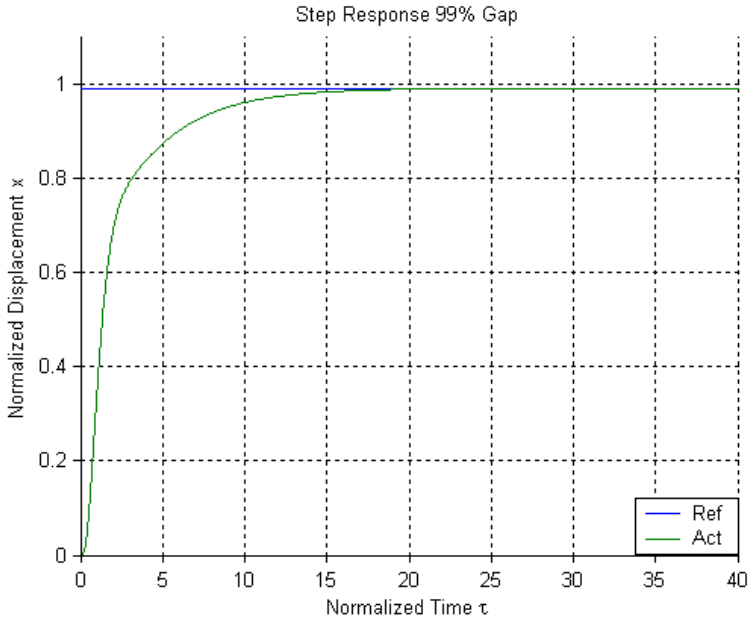

Figure 78: Displacement Output of the Actuator with 99% Gap Traversal

From Figure 78, we can see that it takes approximately 18 time units for the displacement output to reach the desired set-point, which is 99% of full gap. Figure 78 shows an achieved displacement of 99% of the gap with zero overshoot. This suggests that full gap traversal is attainable for the multi-loop control strategy. However, the low loop gain at small displacements slows this response down compared to the previous ADRC (classic ADRC and alternate ADRC) controllers.

The ISEs of the multi-loop controlled actuator for the 3 displacements, which are 10%, 90% and 99% of the full gap are shown in Table XVII. A comparison of the ISEs between the multi-loop controller and the other two designs (classic ADRC and alternate ADRC) is made in Section 5.4.

TABLE XVII: ISE ERROR

Displacement	*ISE*
0.10	0.0454
0.90	0.9755
0.99	1.1113

5.4 Controller Comparison

In this section, the three different designs of classic ADRC, alternate ADRC and multi-loop control will be compared from a performance perspective. The sensitivity of

each design to sensor noise will also be noted. In Table XVIII the ISEs for the three designs at various displacements are given.

TABLE XVIII: CONTROLLER COMPARISON ISE

ISE			
Displacement	*ADRC*	*ADRC Alt*	*Multi-loop*
0.10	0.0144	0.0154	0.0454
0.33	0.1389	0.1406	0.2489
0.50	0.3016	0.3004	0.4359
0.70	0.5757	0.5663	0.6917
0.90	0.9347	0.9113	0.9755
0.99	1.1238	1.0919	1.1113

In Table XVIII the underlined data indicate that the displacement exceeded the maximum travel range of the actuator, which is normalized to one. This would result in the two plates crashing into each other, which is undesirable.

Figure 79 illustrates the data values given in Table XVIII in a bar graph for qualitative analysis.

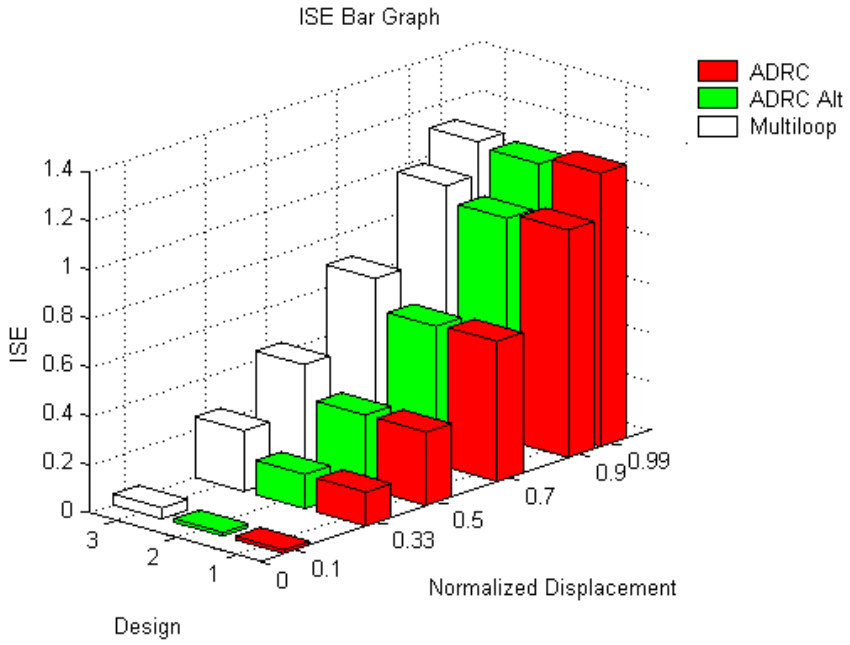

Figure 79: Bar Graph of the ISE for the Three Designs

Figure 79 allows for a quick assessment of the tracking performance of the three designs. It is clear that at low to medium displacements (*0.1* to *0.7* of the full gap) the ADRC and alternate ADRC greatly outperform the multi-loop controller. This advantage begins to wane at the higher displacements. The tracking performances of the classic and alternate ADRC designs begin to deviate from each other at the larger displacements (over 0.7 of full gap).

Figure 80 and Figure 81 show the step responses of the three control designs to the references of 10% and 99% of the full gap respectively.

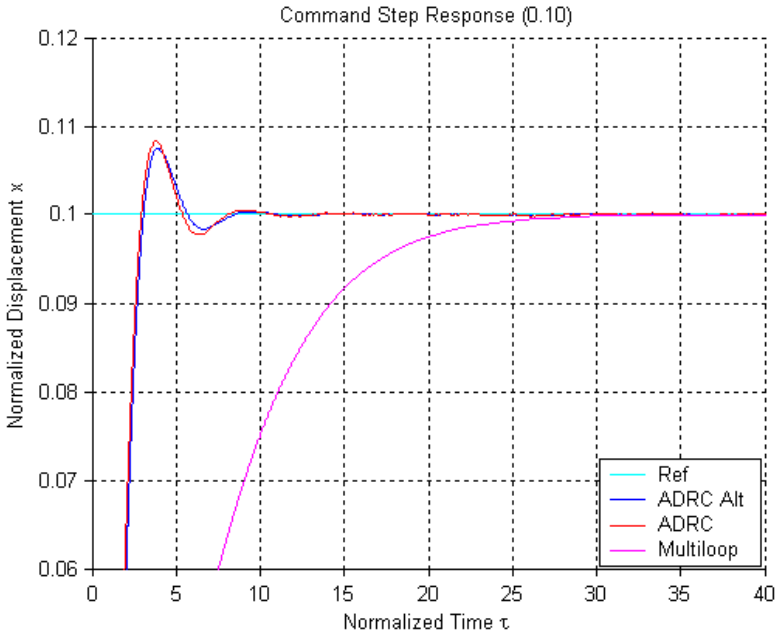

Figure 80: Step Responses of three Controller Designs at 10% of Full Gap

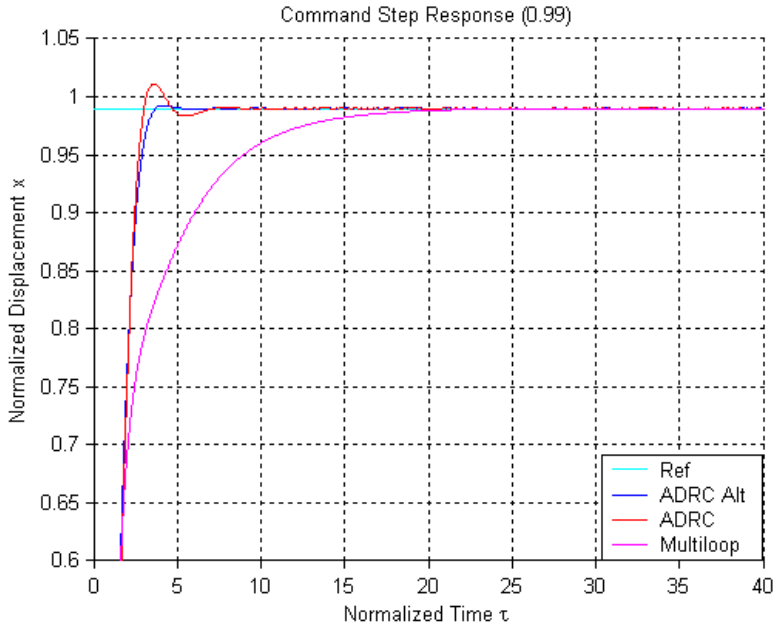

Figure 81: Step Responses of three Controller Designs at 99% of Full Gap

From Figure 80, we can see that the rise time of the classic and alternate ADRC is much smaller than the one of the multi-loop controller at small displacement. However, the step response of the multi-loop control has zero overshoot while the responses of the other two designs exhibit overshoot. Figure 81 demonstrates that only the alternate ADRC design and the multi-loop design can attain 99% gap traversal. Again, the multi-loop design has a very smooth step response compared to the other two designs.

Figure 82 shows the substantial difference of the control signals for the three designs in the presence of sensor noise.

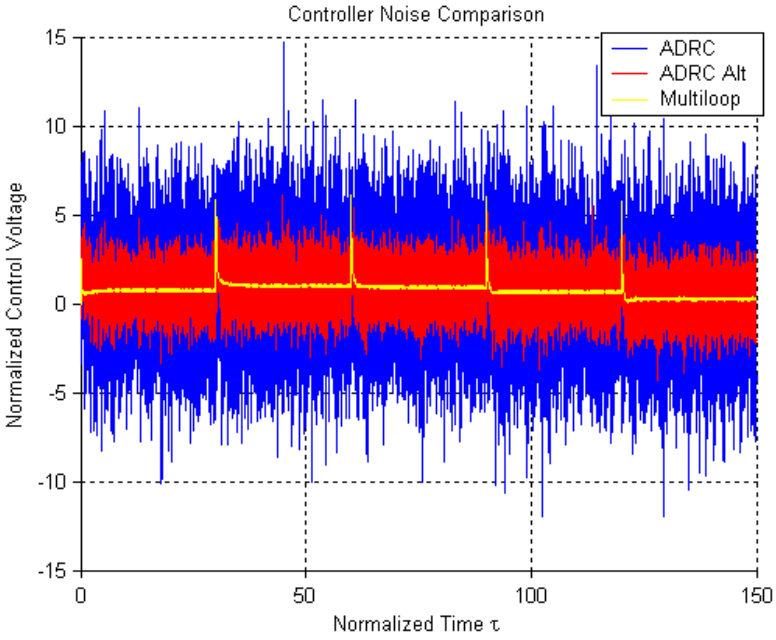

Figure 82: Controller Signals of the Three Designs with Sensor Noise

It is clear from Figure 82 that the multi-loop controller is the best in minimizing the effects of sensor noise among the three controller designs. However, compared to the two single-loop designs (classic and alternate ADRCs), the multi-loop design has to use an additional sensor in the inner loop. The alternate ADRC design has the second best

level of noise amplification. From the tracking performance data provided by Table XVII and the noise minimizing performance demonstrated in Figure 82, it appears that the best design for the electrostatic actuator is the alternate ADRC design, which has excellent tracking performance and noise minimization capability. In addition, the single-loop structure of the alternate ADRC design also makes it an economical choice in the real world. Nevertheless, the multi-loop design shows great promise for the future practical applications of it to the electrostatic actuator in the presence of substantial noise.

CHAPTER VI

CONCLUSIONS

The research aims to provide a feedback controller that could greatly increase the operating range of an electrostatic actuator and to stabilize the actuator over the entire operating range. This controller would have to overcome the pull-in phenomenon inherent in the actuator as the control voltage increases to a specific value. It also has to cope with plant gain variations along with a system pole that moved from the left half complex plane through to the right half complex plane. In addition to the unstable pole, and the bandwidth restrictions this imposed, the controller has to deal with a plant with very little low frequency gain, making the controller design highly susceptible to sensor noise. Finally, the controller needs to be simple enough to implement on a MEMS device where silicon area is at a premium.

The contribution of this thesis is that it develops three forms of linear Active Disturbance Rejection Controllers that provide either full gap traversal for the actuator in the multi-loop design or nearly full gap traversal in the single loop designs in the presences of sensor noise and disturbances. The three forms of controllers have

successfully addressed all the control problems state above. In addition to the effectiveness of these controllers they are simple enough for practical implementation.

The first ADRC design demonstrated that the travel range of the electrostatic actuator could be extended to 97% of the actuators range. It is limited only by some slight overshoot. This design is the most sensitive to sensor noise among the three design strategies.

The second ADRC design showed that the inclusion of additional modeling information could be beneficial in extending the travel range of the actuator up to 99% of the gap. This design was also less susceptible to noise than the first ADRC design. It is simple enough to implement in current MEMS control technology.

The third design is a multi-loop controller based on the ADRC strategy. This controller shows great promise in controlling the electrostatic actuator to 100% travel range, while keeping the effects of sensor noise to a minimum. This design should be considered as a design of the future since current technology makes it difficult to obtain two sensed outputs, but it does serve as a benchmark for what is possible with feedback control. As the complexity of MEMS devices increases the demand for high performance control will also rise, making this design highly practical in the near future.

In current literature, the nonlinear control designs have shown the ability to travel 100% of the gap for the electrostatic actuator. However they have much more complicated control structure than the controller proposed in this thesis. The effects of sensor noise are often neglected in the existing control designs reported in literature while this thesis research considers the noise and effectively rejects the effects of noise. The linear designs in literature have achieved displacements of up to 90% of the gap but they

often are not robust against parameter variations. The simulation results and performance analysis of the ADRC on an electrostatic actuator show strong robustness of the ADRC against structural uncertainties. In general, the proposed control strategies in this thesis offer impressive performance while filling the void between the simple controllers utilized in the past and the nonlinear approaches presented in academia.

6.1 Future Research

There are a few improvements to this research that should be conducted in the future. The first improvement would be to develop a higher frequency model of the electrostatic actuator. The model currently being used is adequate for control design but is merely a first step in the modeling process. The new model should include a more accurate description of the squeeze-film damping phenomena close to full gap traversal. Since feedback control was utilized in this thesis, it would be desirable to introduce a model of a realistic position sensor. With the amplification of noise sources being such an issue in the electrostatic actuator design it would also be prudent to conduct a more thorough analysis of noise sources in the micro-scale environment, to include a bound on their magnitude. Once this model has been completed, the next step would be to look at 2-DOF models that allow one to study the tip-in phenomenon, which occurs when the moveable electrode rotates, and creates different displacements at the two ends of its plates. The tip-in phenomenon could affect system stability. Finally, it would be

beneficial to create an accurate simulation model utilizing MEMS^{PRO} CAD software to fully test the performance of the control schemes presented in this thesis.

REFERENCES

1. Y. Nemirovsky, “A methodology and model for the pull-in parameters of electrostatic actuators,” *Journal of Microelectromechanical Systems*, Vol. 10, No. 4, pp. 601-615, Dec. 2001.

2. J. Seeger, “Charge control of parallel-plate, electrostatic actuators and the tip-in instability,” *Journal of Microelectromechanical Systems*, Vol. 12, No. 5, pp. 656-671, Oct. 2003.

3. A. Papavasiliou and S. Olivier, “Nanolaminate foils used to make deformable mirrors,” *International Society for Optical Engineering*, SPIE Newsroom, available on http://photonicsclusters.org.

4. G. Zhu, J. Levine, and L. Praly, “On the differential flatness and control of electrostatically actuated MEMS,” in *Proc. of 2005 American Control Conference*, Portland, Oregon, pp. 2493-2498, June 2005.

5. L. Hornbeck, “Digital Light Processing: A New MEMS-Based Display Technology,” Texas Instruments, available on www.focus.ti.com.

6. S.D. Senturia, *Microsystem Design*, Kluwer Academic Publishers, Norwell, MA, 2001.

7. J. Bryzek, A. Flannery, and D. Skurnik, “Integrating microelectromechanical systems with integrated circuits,” *IEEE Instrumentation & Measurement Magazine*, pp. 51-59, June 2004.

8. J. Bryzek and E. Abbot, “Control issues for MEMS,” in *Proc of the 42nd IEEE Conference on Decision and Control*, Maui, Hawaii, pp. 3039-3047, Dec. 2003.

9. B. Borovic, F. Lewis, et al., “Control issues for microelectromechanical systems,” *IEEE Control Systems Magazine*, Vol. 26, No. 2, pp. 18-21, April 2006.

10. E. S. Hung and S. D. Senturia, “Extending the travel range of analog-tuned electrostatic actuators,” *Journal of Microelectromechanical Systems*, Vol. 8, No. 4, pp. 497-505, Dec. 1999.

11. B. Borovic, “Open-loop versus closed-loop control of MEMS devices: choices and issues,” *Journal of Micromechanics and Micro-engineering*, Vol. 15, No.10, pp. 1917-1924, July 2005.

12. J. Seeger and S. Crary, “Stabilization of electrostatically actuated mechanical devices,” *IEEE International Conference on Solid-State Sensors and Actuators*, pp. 1133-1136, June 1997.

13. E. Chan and R. Dutton, “Electrostatic micromechanical actuator with extended range of travel,” *Journal of Microelectromechanical Systems*, Vol. 9, No. 3, pp. 321-328, Sep. 2000.

14. M. Lu and G. Fedder, "Closed-loop control of a parallel-plate microactuator beyond the pull-in limit," *Solid-State Sensor, Actuator and Microsystems Workshop*, pp. 255-258, Jun. 2002.

15. M. Lu, M. Hirano, G. Fedder, "Position control of parallel-plate microactuators for probe-based data storage," *Journal of Microelectromechanical Systems*, Vol. 13, No. 5, pp. 759-769, Oct. 2004.

16. I. Horowitz, *Quantitative Feedback Design Theory*, QFT Publications, Boulder Colorado, 1992.

17. G. Zhu, J. Levine, and L. Praly, "Improving the performance of an electrostatically actuated MEMS by nonlinear control: some advances and comparisons," in *Proc. of the 44th IEEE Conference on Decision and Control*, pp. 7534-7539, Dec. 2005.

18. G. Zhu, J. Penet, and L. Saydy, "Robust control of an electrostatically actuated MEMS in the presence of parasitics and parametric uncertainty," in *Proc. of the 2006 American Control Conference*, pp. 1233-1238, Jun. 2006.

19. H. A. C. Tilmans, "Equivalent circuit representation of electromechanical transducers I: Lumped-parameter systems," *Journal of Micromechanics and Microengineering*, Vol. 6, pp. 157-176, 1996.

20. H. H. Woodson and J. R. Melcher, *Electromechanical Dynamics, Part I: Discrete Systems*, chapter 3, John Wiley & Sons, New York, 1968.

21. S. Skogestad and I. Postlethwaite, *Multivariable Feedback Control: Analysis and Design 2nd Ed*., Wiley-Interscience Publishing, November 18, 2005.

22. Z. Gao, "Scaling and bandwidth-parameterization based controller tuning", in *Proc. of the 2003 American Control Conference*, Vol. 6, pp. 4989-4996, June 2003.

23. R. Miklosovic, A. Radke, Z. Gao, "Discrete implementation and generalization of the extended state observer," in *Proc. of the American Control Conference*, Minneapolis Minnesota, pp. 2209-2214, Jun. 2006.

24. G. Tian and Z. Gao, "Frequency response analysis of active disturbance rejection based control system," in *IEEE Multi Conference on Systems and Control, pp*. 1595-1599, Oct. 2007.

25. Z. Gao, "From linear to nonlinear control means: a practical progression," *ISA Transactions*, Vol. 41, No. 2, pp. 177-189, April 2002.

26. R. Miklosovic and Z. Gao, "A robust two-degree-of-freedom control design technique and its practical application," *Industry Applications Conference*, Vol. 3, pp. 1495-1502, Oct. 2004.

27. Z. Gao, "Active disturbance rejection control: a paradigm shift in feedback control system design," in *Proc. of the American Control Conference*, Minneapolis Minnesota, pp. 2399-2405, Jun. 2006.

28. B. Alexander, R. Rarick, L. Dong, "Application of active disturbance rejection control to self-sensing magenetic bearings," in *Proc. of the American Control Conference*, New York City New York, pp. 2910-2914, Jul. 2007.

29. Y. Hou, Z. Gao, F. Jiang, B. Boulter, "Active disturbance rejection control for web tension regulation," in *Proc. of IEEE Conference on Decision and Control*, Orlando, FL, pp. 4974-4979, Dec. 2001.

30. B. Sun and Z. Gao, "A DSP-based active disturbance rejection control design for a 1-kW H-bridge DC-DC power converter," *IEEE Transactions on Industrial Electronics*, Vol. 52, No. 5, pp. 1271-1277, Oct. 2005.

31. L. Dong, Q. Zheng, Z. Gao, "A novel oscillation controller for vibrational MEMS gyroscopes," in *Proc. of the American Control Conference* , New York City New York, pp. 3204-3209, Jul. 2007.

32. Q. Zheng, L. Dong, Z. Gao, "A novel control system design for vibrational MEMS gyroscopes," *Sensors and Transducers Journa*l, Vol. 78, pp. 1073-1082, Apr. 2007.

33. G. Ellis, *Control System Design Guide 3rd Ed*., Elsevier Academic Press, 2004.

34. E. Schrijver, J. Dijk, "Disturbance observers for rigid mechanical systems: equivalence, stability, and design," *Journal of Dynamic Systems, Measurement, and Control*, 2002 ASME, Vol. 124, pp. 539-548, Dec. 2002.

APPENDICES

Appendix A

This appendix provides a step by step normalization of the nonlinear differential equations that model the electrostatic actuator.

Equation Normalization

The displacement of the upper plate relative to the fixed lower plate (*X*) is normalized by the gap with zero applied voltage (maximum gap) g_0. The units of time (*t*) are scaled by the natural frequency of the actuator system ω_0. The charge accumulation on the plates (*Q*), the voltage across the actuator plates (V_{act}), and the applied source voltage (V_S) are normalized by their pull-in values as shown in (A.1).

$$x = \frac{X}{g_0} \quad \tau = \omega_0 t \quad q = \frac{Q}{q_{pi}} \quad v_{act} = \frac{V_{act}}{v_{pi}} \quad v_s = \frac{V_s}{v_{pi}} \tag{A.1}$$

The pull-in voltage v_{pi}, the amount of charge accumulated on the actuators plates at pull-in q_{pi} and the capacitance at full gap C_0 (zero applied voltage) are given in (A.2).

$$q_{pi} = \frac{3}{2} C_0 v_{pi} \quad v_{pi} = \sqrt{\frac{8kg_0^2}{27C_0}} \quad C_0 = \frac{\varepsilon A}{g_0} \tag{A.2}$$

The nonlinear differential equations that model the electrostatic actuator are given in (A.3).

$$\begin{aligned} m\ddot{X} + b\dot{X} + kX - \frac{1}{2\varepsilon A}Q^2 &= 0 \\ R\dot{Q} + \frac{1}{\varepsilon A}(g_0 - X)Q &= V_S \end{aligned} \tag{A.3}$$

The first equation in (A.3) describing the motion of the upper plate of the electrostatic actuator will be the first equation to be normalized. The normalization will start with the scaling of the time base *t*, utilizing the relation given in (A.1), and is shown in (A.4).

$$m\frac{d^2X}{d\left(\frac{\tau}{\omega_0}\right)^2} + b\frac{dX}{d\left(\frac{\tau}{\omega_0}\right)} + kX = \frac{Q^2}{2C_0 g_0} \tag{A.4}$$

Multiplying (A.4) by ω_0^2 / ω_0^2 simpflies (A.4) to

$$m\omega_0^2\frac{d^2X}{d\tau^2} + b\omega_0\frac{dX}{d\tau} + kX = \frac{Q^2}{2C_0 g_0}. \tag{A.5}$$

The displacement of the upper plate is normalized by replacing each occurrence of *X* with $g_0 x$, as shown in (A.6).

$$m\omega_0^2\frac{d^2(g_0 x)}{d\tau^2} + b\omega_0\frac{d(g_0 x)}{d\tau} + k(g_0 x) = \frac{Q^2}{2C_0 g_0} \tag{A.6}$$

Since g_0 is a constant (A.6) can be rewritten as

$$m\omega_0^2 g_0\frac{d^2x}{d\tau^2} + b\omega_0 g_0\frac{dx}{d\tau} + kg_0 x = \frac{Q^2}{2C_0 g_0}. \tag{A.7}$$

Dividing (A.7) by $m\omega_0^2 g_0$ results in

$$\frac{d^2x}{d\tau^2}+\frac{b}{m\omega_0}\frac{dx}{d\tau}+\frac{k}{m\omega_0^2}x=\frac{1}{m\omega_0^2}\frac{Q^2}{2C_0g_0^2}. \tag{A.8}$$

Next, the charge is normalized by replacing Q with qq_{pi}.

$$\frac{d^2x}{d\tau^2}+\frac{b}{m\omega_0}\frac{dx}{d\tau}+\frac{k}{m\omega_0^2}x=\frac{1}{m\omega_0^2}\frac{\left(qq_{pi}\right)^2}{2C_0g_0^2} \tag{A.9}$$

Substituting the relation for q_{pi} given in (A.2) into (A.9) gives

$$\frac{d^2x}{d\tau^2}+\frac{b}{m\omega_0}\frac{dx}{d\tau}+\frac{k}{m\omega_0^2}x=\frac{1}{m\omega_0^2}\frac{q^2\left(\frac{3}{2}C_0v_{pi}\right)^2}{2C_0g_0^2}. \tag{A.10}$$

Equation (A.10) can be simplified further; the result is shown in (A.11).

$$\frac{d^2x}{d\tau^2}+\frac{b}{m\omega_0}\frac{dx}{d\tau}+\frac{k}{m\omega_0^2}x=\frac{1}{m\omega_0^2}\frac{9C_0v_{pi}^2}{8g_0^2}q^2. \tag{A.11}$$

The pull-in voltage v_{pi} defined in (A.2) is substituted into (A.11) as shown in (A.12).

$$\frac{d^2x}{d\tau^2}+\frac{b}{m\omega_0}\frac{dx}{d\tau}+\frac{k}{m\omega_0^2}x=\frac{1}{m\omega_0^2}\frac{9C_0\left(\sqrt{\frac{8kg_0^2}{27C_0}}\right)^2}{8g_0^2}q^2 \tag{A.12}$$

Equation (A.12) can be simplified into the equation given by (A.13).

$$\frac{d^2x}{d\tau^2}+\frac{b}{m\omega_0}\frac{dx}{d\tau}+\frac{k}{m\omega_0^2}x=\frac{k}{3m\omega_0^2}q^2 \tag{A.13}$$

The natural frequency of the system is defined in (A.14).

$$\omega_0 = \sqrt{\frac{k}{m}} \tag{A.14}$$

Equation (A.14) can be used to simplify (A.13). The resulting equation is given in (A.15).

$$\frac{d^2x}{d\tau^2} + \frac{b}{m\omega_0}\frac{dx}{d\tau} + x = \frac{q^2}{3} \tag{A.15}$$

Finally, the damping ratio zeta (ς) is defined in (A.16).

$$\varsigma = \frac{b}{2m\omega_0}. \tag{A.16}$$

Substituting (A.16) into (A.15) gives the normalized equation for the motion of the upper plate of the electrostatic actuator.

$$\frac{d^2x}{d\tau^2} + 2\varsigma\frac{dx}{d\tau} + x = \frac{q^2}{3} \tag{A.17}$$

The normalization of the differential equation that relates the source voltage to the charge accumulated on the plates, given in (A.3) is repeated in (A.18).

$$R\dot{Q} + \frac{1}{\varepsilon A}(g_0 - X)Q = V_s \tag{A.18}$$

Equation (A.18) is rewritten in (A.19) to show the explicit dependence on time.

$$R\frac{dQ}{dt} + \frac{1}{\varepsilon A}(g_0 - X)Q = V_s \tag{A.19}$$

The time base *t* is scaled by the natural frequency ω_0, as in (A.20).

$$R\frac{dQ}{d\left(\frac{\tau}{\omega_0}\right)}+\frac{1}{\varepsilon A}(g_0-X)Q=V_s \tag{A.20}$$

Equation (A.20) can be simplified to

$$R\omega_0\frac{dQ}{d\tau}+\frac{1}{\varepsilon A}(g_0-X)Q=V_s. \tag{A.21}$$

Next, the charge Q is normalized by replacing each occurrence of Q with qq_{pi}.

$$R\omega_0\frac{d(qq_{pi})}{d\tau}+\frac{1}{\varepsilon A}(g_0-X)(qq_{pi})=V_s \tag{A.22}$$

The pull-in value of the charge q_{pi} is a constant, thus it can be moved outside of the derivative.

$$R\omega_0 q_{pi}\frac{dq}{d\tau}+\frac{1}{\varepsilon A}(g_0-X)(qq_{pi})=V_s \tag{A.23}$$

Dividing (A.23) by q_{pi} results in

$$R\omega_0\frac{dq}{d\tau}+\frac{1}{\varepsilon A}(g_0-X)q=\frac{V_s}{q_{pi}}. \tag{A.24}$$

The displacement X is normalized by replacing each occurrence of X with $g_0 x$.

$$R\omega_0\frac{dq}{d\tau}+\frac{1}{\varepsilon A}(g_0-g_0x)q=\frac{V_s}{q_{pi}} \tag{A.25}$$

Equation (A.25) can be rewritten as

$$R\omega_0\frac{dq}{d\tau}+\frac{1}{C_0}(1-x)q=\frac{V_s}{q_{pi}}. \tag{A.26}$$

Equation (A.26) can be reduced further by dividing it by $R\omega_0$.

$$\frac{dq}{d\tau}+\frac{1}{\omega_0 RC_0}(1-x)q=\frac{V_s}{\omega_0 Rq_{pi}} \tag{A.27}$$

The voltage source is normalized by substituting $v_{pi}v_s$ for V_s.

$$\frac{dq}{d\tau}+\frac{1}{\omega_0 RC_0}(1-x)q=\frac{v_{pi}v_s}{\omega_0 Rq_{pi}} \tag{A.28}$$

The pull-in charge is defined in (A.29).

$$q_{pi}=\frac{3}{2}C_0 v_{pi} \tag{A.29}$$

Substituting (A.29) into (A.28) results in

$$\frac{dq}{d\tau}+\frac{1}{\omega_0 RC_0}(1-x)q=\frac{v_{pi}v_s}{\omega_0 R\left(\frac{3}{2}C_0 v_{pi}\right)}. \tag{A.30}$$

Canceling out the pull-in voltage terms reduces (A.30) to (A.31).

$$\frac{dq}{d\tau}+\frac{1}{\omega_0 RC_0}(1-x)q=\frac{2v_s}{3\omega_0 RC_0} \tag{A.31}$$

The normalized resistance is defined in (A.32).

$$r=\omega_0 RC_0 \tag{A.32}$$

Substituting (A.32) into (A.31) gives the normalized equation for the charge

$$\frac{dq}{d\tau}+\frac{1}{r}(1-x)q=\frac{2}{3r}v_s. \tag{A.33}$$

Appendix B

Frequency Domain Representation of a 2nd Order ESO

The state space model of a Luenberger observer contains a model of the plant under study along with a feedback correction term, as shown by (B.1).

$$\begin{aligned} \dot{z} &= Az + Bu + L\left(y - \hat{y}\right) \\ \hat{y} &= Cz \end{aligned} \quad . \tag{B.1}$$

The observer of (B.1) can be rewritten as (B.2).

$$\dot{z} = \left(A - LC\right)z + Bu + Ly \tag{B.2}$$

The observer design calls for a 2nd order ESO with real repeated observer poles located at ω_o. The observer of (B.2) is changed to reflect this information in (B.3).

$$\begin{bmatrix} \dot{z}_1 \\ \dot{z}_2 \end{bmatrix} = \begin{bmatrix} -2\omega_o & 1 \\ -\omega_o^2 & 0 \end{bmatrix} \begin{bmatrix} z_1 \\ z_2 \end{bmatrix} + \begin{bmatrix} 1 & 2\omega_o \\ 0 & \omega_o^2 \end{bmatrix} \begin{bmatrix} u \\ y \end{bmatrix} \tag{B.3}$$

The Laplace transform of (B.3) is taken next, the result is shown in (B.4).

$$\begin{aligned} sZ_1(s) &= -2\omega_o Z_1(s) + Z_2(s) + U(s) + 2\omega_o Y(s) \\ sZ_2(s) &= -\omega_o^2 Z_1(s) + \omega_o^2 Y(s) \end{aligned} \quad . \tag{B.4}$$

Solving for the state estimate $Z_1(s)$ will be performed next. The equation for the estimated state $Z_1(s)$ is given in (B.5).

$$sZ_1(s) = -2\omega_o Z_1(s) + Z_2(s) + U(s) + 2\omega_o Y(s) \tag{B.5}$$

Equation (B.5) can be simplified by bringing all the $Z_1(s)$ terms to the left side of the equal sign.

$$(s + 2\omega_o)Z_1(s) = Z_2(s) + U(s) + 2\omega_o Y(s) \tag{B.6}$$

The equation for the extended state $Z_2(s)$ is easily solved and is substituted into (B.6).

$$s(s + 2\omega_o)Z_1(s) = \left(-\omega_o^2 Z_1(s) + \omega_o^2 Y(s)\right) + sU(s) + 2\omega_o sY(s) \tag{B.7}$$

Equation (B.7) is simplified by bringing all the $Z_1(s)$ terms to the left side of the equal sign.

$$\left(s(s + 2\omega_o) + \omega_o^2\right)Z_1(s) = \omega_o^2 Y(s) + sU(s) + 2\omega_o sY(s) \tag{B.8}$$

Next, (B.8) is reduced further by collecting like terms and factoring the left side.

$$(s + \omega_o)^2 Z_1(s) = \left(2\omega_o s + \omega_o^2\right)Y(s) + sU(s). \tag{B.9}$$

Finally, the transfer function for the estimated position is given in (B.10).

$$Z_1(s) = \frac{2\omega_o s + \omega_o^2}{(s + \omega_o)^2} Y(s) + \frac{s}{(s + \omega_o)^2} U(s) \tag{B10}$$

When the nominal model of the plant is perfect the control signal $U(s)$ can be obtained by filtering the measured output $Y(s)$ by the inverse of the nominal model, as shown in (B.11).

$$U(s) = P_n^{-1}(s)Y(s) \tag{B.11}$$

The inverse of the nominal plant $P_n(s)$ is

$$P_n^{-1}(s) = s\,. \tag{B.12}$$

Equation (B.10) can be rewritten as

$$Z_1(s) = \frac{2\omega_o s + \omega_o^2}{(s+\omega_o)^2} Y(s) + \frac{s^2}{(s+\omega_o)^2} Y(s). \tag{B.13}$$

Equation (B.13) reduces to

$$Z_1(s) = \frac{s^2 + 2\omega_o s + \omega_o^2}{(s+\omega_o)^2} Y(s) = Y(s). \tag{B.14}$$

The Laplace transform of the extended state is repeated in (B.15).

$$sZ_2(s) = -\omega_o^2 Z_1(s) + \omega_o^2 Y(s) \tag{B.15}$$

The transfer function for the estimated output $Z_1(s)$ is then substituted into (B.15) resulting in

$$sZ_2(s) = -\omega_o^2 \left[\frac{2\omega_o s + \omega_o^2}{(s+\omega_o)^2} Y(s) + \frac{s}{(s+\omega_o)^2} U(s) \right] + \omega_o^2 Y(s). \tag{B.16}$$

Simplifying (B.16) results in the transfer function for the extended state that is given in (B.23).

$$Z_2(s) = \frac{\omega_o^2 s}{(s+\omega_o)^2} Y(s) - \frac{\omega_o^2}{(s+\omega_o)^2} U(s) \tag{B.17}$$

The frequency domain representation of a 2nd order ESO is given in (B.24) and (B.25).

$$Z_1(s) = \frac{2\omega_o s + \omega_o^2}{(s+\omega_o)^2} Y(s) + \frac{s}{(s+\omega_o)^2} U(s) \tag{B.18}$$

$$Z_2(s) = \frac{\omega_o^2 s}{(s+\omega_o)^2} Y(s) - \frac{\omega_o^2}{(s+\omega_o)^2} U(s) \tag{B.19}$$

The frequency domain representation of a state observer can also be written as

$$\hat{Y}(s) = \frac{P_n(s)}{1+P_n(s)C(s)} U(s) + \frac{P_n(s)C(s)}{1+P_n(s)C(s)} Y(s). \tag{B.20}$$

The transfer function $P_n(s)$ is the nominal model of the plant and the transfer function $C(s)$ is a controller (internal to the observer) that attempts to drive the error between the actual and estimated output to zero.

The estimated output $Z_1(s)$ can be represented as in (B.20), the transfer function relating the output estimate to the control signal is

$$\frac{P_n}{1+P_n C} = \frac{s}{(s+\omega_o)^2}. \tag{B.21}$$

The transfer function relating the estimated output to the actual measured output of the plant would be

$$\frac{P_n C}{1+P_n C} = \frac{2\omega_o s + \omega_o^2}{(s+\omega_o)^2}. \tag{B.22}$$

Solving (B.21) and (B.22) for the error controller *C* results in

$$C = \left(\frac{P_n C}{1+P_n C}\right)\left(\frac{1+P_n C}{P_n}\right) = \left(\frac{2\omega_o s + \omega_o^2}{(s+\omega_o)^2}\right)\left(\frac{(s+\omega_o)^2}{s}\right) = \frac{\omega_o^2}{s} + 2\omega_o. \tag{B.23}$$

The result of (B.23) is clearly a PI controller. This implies that the observer will have zero steady state error to constant disturbances.